

UNIVERSITY OF OKLAHOMA

GRADUATE COLLEGE

A BIOINORGANIC APPROACH TO THE STUDY OF THE INTERACTIONS OF  
NITROGEN OXIDES WITH MANGANESE PORPHYRINS AND MANGANESE-  
AND COBALT-RECONSTITUTED MYOGLOBIN

A DISSERTATION

SUBMITTED TO THE GRADUATE FACULTY

in partial fulfillment of the requirements for the

Degree of

DOCTOR OF PHILOSOPHY

By

ZAKI NABEIH AHMED ZAHRAN

Norman, Oklahoma

2007

UMI Number: 3284234



---

UMI Microform 3284234

Copyright 2008 by ProQuest Information and Learning Company.  
All rights reserved. This microform edition is protected against  
unauthorized copying under Title 17, United States Code.

---

ProQuest Information and Learning Company  
300 North Zeeb Road  
P.O. Box 1346  
Ann Arbor, MI 48106-1346

A BIOINORGANIC APPROACH TO THE STUDY OF THE INTERACTIONS OF  
NITROGEN OXIDES WITH MANGANESE PORPHYRINS AND MANGANESE-  
AND COBALT-RECONSTITUTED MYOGLOBIN

A DISSERTATION APPROVED FOR THE  
DEPARTMENT OF CHEMISTRY AND BIOCHEMISTRY

BY

---

George B. Richter-Addo

---

Robert P. Houser

---

Patrick J. McCann

---

Richard W. Taylor

---

Ann H. West



## Acknowledgements

All my thanks and praise are to Allah (God) who created us and created this beautiful and well-organized universe. It is he who gives us this free beautiful sun to warm up with, the free air to breath. It is he who controls the functions of all enzymes in our bodies; with our limitation we spend years and years trying to figure out just a small part of their functions.

I am deeply thankful to my mentor Dr. George B. Richter-Addo for his guidance, support, and encouragement throughout my Ph.D studies at OU. He is helpful all the times. He was very close to me during my work advising me.

I would like to thank Drs. Ann West, Richard Taylor, Robert Houser, and Patrick McCann for serving as my Advisory Committee members. Your friendly help and guidance has been invaluable. I would like to extend special thanks to Drs. Masood Khan and Douglas Powell for their help with small molecule X-ray crystallographic studies. I am thankful to Dr. Susan Alguindigie for her help with NMR studies. I am also indebted to Dr. Michael Shaw (Southern Illinois University, Edwardsville) for his insightful help with my spectro-electrochemical studies and his friendship.

I would like also to thank Drs. Lilian Chooback, Jonghyuk Lee, and Daniel Copeland in Dr. Richter-Addo's research group. I would also like to thank my other coworkers in Dr. Richter-Addo's research group: Dr. Shawn Charter, Myron Jones, Nan Xu, Carolina Salazar, Yi (Eva) Jun, and Adam Warhausen. I have sincerely enjoyed being around these people and consider all of them friends.

I am grateful to my wife Eman, without her help I could not finish this work. She is always patient and helpful.

I am also grateful to the Muslim Community in Norman who provided a good atmosphere for me during my work.

I am very thankful to the Egyptian Government and all the people in the Cultural and Educational Bureau in Washington D.C for my scholarship and help during my time in the United States. Additionally, I am thankful to the National Institutes of Health (NIH) and National Science Foundation (NSF) for the funding that went towards the completion of this dissertation.

Finally, I would like to dedicate this dissertation to my Mother, Father, my kids (Umna and Ameir), my Mother-in-law, my Father-in-law, my Sister, my Sisters-in-law, my Brothers, and my Brother-in-Law.

## Table of Contents

	Page	
List of Tables	viii	
List of Figures	ix	
List of Schemes	xi	
List of abbreviations	xi	
Abstract	xii	
Chapter 1	Introduction	1
	1.1 Nitric Oxide in Biology	2
	1.2 Nitrite ion in Biology	4
	1.3 Manganese porphyrins and manganese proteins	6
	1.4 References	8
Chapter 2	Synthesis, Molecular Structure, and Redox Behavior of an oxo-bridged dimer of a Ruthenium-bpb Nitrosyl	
	2.1 Introduction	13
	2.2 Experimental Section	14
	2.3 Results and Discussion	19
	2.4 Conclusion	25
	2.5 References	26
Chapter 3	Synthesis, Molecular Structures, and Fiber-optic Infrared Spectroelectrochemical Studies of Six-Coordinate Manganese Nitrosyl Porphyrins	
	3.1 Introduction	28
	3.2 Experimental Section	31

	3.3 Results and Discussion	44
	3.4 Conclusion	73
	3.5 References	74
Chapter 4	Ligand Conformations in Derivatives of Manganese- and Cobalt-Substituted Horse Heart Myoglobin As Determined by X-ray Crystallography	
	4.1 Introduction	77
	4.2 Materials and Methods	79
	4.3 Crystallization and Complex Formation	80
	4.4 X-ray Diffraction Data Collection and Processing	83
	4.5 Structure Solution and Refinement	83
	4.6 Protein Data Bank accession numbers	87
	4.7 Results	87
	4.8 Discussion	101
	4.9 Conclusion	119
	4.9 References	120
Appendix	Table 2.4. Bond Lengths [ $\text{\AA}$ ] for $[\text{Ru}(\text{bpb})(\text{NO})_2(\mu\text{-O})]$ .	125
	Table 2.5. Bond Angles ( $^\circ$ ) for $[\text{Ru}(\text{bpb})(\text{NO})_2(\mu\text{-O})]$ .	125
	Table 3.6. Bond Lengths [ $\text{\AA}$ ] for $(\text{TTP})\text{Mn}(\text{NO})(\text{MeOH})$ .	126
	Table 3.7. Bond Angles [ $^\circ$ ] for $(\text{TTP})\text{Mn}(\text{NO})(\text{MeOH})$ .	128
	Table 3.8. Bond Lengths [ $\text{\AA}$ ] for $(\text{TTP})\text{Mn}(\text{NO})(1\text{-MeIm})$ .	131
	Table 3.9. Bond Angles [ $^\circ$ ] for $(\text{TTP})\text{Mn}(\text{NO})(1\text{-MeIm})$ .	134
	Table 3.10. Bond Lengths [ $\text{\AA}$ ] for $(\text{TPP})\text{Mn}(\text{NO})(1\text{-MeIm})$ .	139
	Table 3.11. Bond Angles [ $^\circ$ ] for $(\text{TPP})\text{Mn}(\text{NO})(1\text{-MeIm})$ .	141

Table 3.12. Bond Lengths [ $\text{\AA}$ ] for  
(T(*p*-OCH<sub>3</sub>)PP)Mn(NO)(1-MeIm). 145

Table 3.13. Bond Angles [ $^{\circ}$ ] for  
(T(*p*-OCH<sub>3</sub>)PP)Mn(NO)(1-MeIm). 146

### List of Tables

	Page
Table 2.1. Crystal Data and Structure Refinement of [(bpb)Ru(NO)] <sub>2</sub> O · CH <sub>2</sub> Cl <sub>2</sub>	18
Table 2.2. Selected Vibrational Frequencies (cm <sup>-1</sup> ) and Geometric Parameters ( $\text{\AA}$ , $^{\circ}$ ) for oxo-bridged Ruthenium Compounds. <sup>a</sup>	21
Table 2.3. Selected Bond Lengths and Angles for [Ru(bpb)(NO)] <sub>2</sub> ( $\mu$ -O)	22
Table 3.1. Crystal Data and Structure Refinement of (TTP)Mn(NO)(CH <sub>3</sub> OH) ( <b>1</b> ), (TTP)Mn(NO)(1-MeIm).0.28CH <sub>2</sub> Cl <sub>2</sub> ( <b>2</b> ), (TPP)Mn(NO)(1-MeIm).2.5toluene ( <b>3</b> ), and (T( <i>p</i> -OCH <sub>3</sub> )PP)Mn(NO)(1-MeIm).CH <sub>2</sub> Cl <sub>2</sub> ( <b>4</b> ).	43
Table 3.2. Selected Bond Lengths in ( $\text{\AA}$ ) and Angles in ( $^{\circ}$ ) of (TTP)Mn(NO)(CH <sub>3</sub> OH) ( <b>1</b> ), (TTP)Mn(NO)(1-MeIm) ( <b>2</b> ), (TPP)Mn(NO)(1-MeIm) ( <b>3</b> ), and (T( <i>p</i> -OCH <sub>3</sub> )PP)Mn(NO)(1-MeIm) ( <b>4</b> ).	49
Table 3.3. Infrared (cm <sup>-1</sup> ) and Electrochemical Data for the (por)Mn(NO)(1-MeIm) Compounds in CH <sub>2</sub> Cl <sub>2</sub> at 23 $^{\circ}$ C.	61
Table 3.4. Electrochemical Data for the (por)Mn(NO)(1-MeIm) Compounds in CH <sub>2</sub> Cl <sub>2</sub> at -78 $^{\circ}$ C.	61
Table 3.5. Infrared (cm <sup>-1</sup> ) and Electrochemical Data for the (por)Mn(NO)(1-MeIm) Compounds in THF at 23 $^{\circ}$ C.	62
Table 4.1. Statistics of X-Ray Data Collection and Refinement.	89
Table 4.2. Selected Geometrical Data for the Mn- and Co-substituted Myoglobin Complexes.	90

## List of Figures

		Page
Figure 2.1.	Molecular structure of $[\text{Ru}(\text{bpb})(\text{NO})]_2(\mu\text{-O})$ .	20
Figure 2.2.	Cyclic voltammogram of 0.1 mM $\text{Ru}(\text{bpb})(\text{NO})\text{Cl}$ in DMF containing 0.1 M $\text{NBu}_4\text{PF}_6$ .	23
Figure 2.3.	Cyclic voltammogram of 0.1 mM $[\text{Ru}(\text{bpb})\text{NO}]_2\text{O}$ in DMF containing 0.1 M $\text{NBu}_4\text{PF}_6$ .	24
Figure 3.1.	Structural representation of the new $(\text{por})\text{Mn}(\text{NO})(\text{L})$ complexes.	31
Figure 3.2.	Schematic diagram of the TDLAS instrument.	34
Figure 3.3.	(a) Molecular structure of $(\text{TTP})\text{Mn}(\text{NO})(\text{CH}_3\text{OH})$ . (b) View of the orientation of the methanol ligand relative to the porphyrin skeleton.	50
Figure 3.4.	(a) Molecular structure of $(\text{TTP})\text{Mn}(\text{NO})(1\text{-MeIm})$ . (b) View of the orientation of the 1-MeIm ligand relative to the porphyrin skeleton.	51
Figure 3.5.	(a) Molecular structure of $(\text{TPP})\text{Mn}(\text{NO})(1\text{-MeIm})$ . Hydrogen atoms have been omitted for clarity. (b) View of the orientation of the 1-MeIm ligand relative to the porphyrin skeleton. The porphyrin <i>p</i> -phenyl substituents have been omitted for clarity.	52
Figure 3.6.	(a) Molecular structure of $(\text{T}(p\text{-OCH}_3)\text{PP})\text{Mn}(\text{NO})(1\text{-MeIm})$ . (b) View of the orientation of the 1-MeIm ligand relative to the porphyrin skeleton.	53
Figure 3.7.	Cyclic voltammogram of $(\text{T}(p\text{-OCH}_3)\text{PP})\text{Mn}(\text{NO})(1\text{-MeIm})$ in $\text{CH}_2\text{Cl}_2$ at 23 °C.	55
Figure 3.8.	Difference IR spectra of $(\text{T}(p\text{-OCH}_3)\text{PP})\text{Mn}(\text{NO})(1\text{-MeIm})$ and its products in $\text{CH}_2\text{Cl}_2$ : (a) showing the consumption of starting $(\text{T}(p\text{-OCH}_3)\text{PP})\text{Mn}(\text{NO})(1\text{-MeIm})$ after the first oxidation without the formation of a new nitrosyl-containing species at 23 °C, (b) showing the consumption of starting $(\text{T}(p\text{-OCH}_3)\text{PP})\text{Mn}(\text{NO})(1\text{-MeIm})$ after the first oxidation with the concomitant formation of a new nitrosyl-containing species at -78 °C, and (c) showing the consumption of starting $(\text{T}(p\text{-OCH}_3)\text{PP})\text{Mn}(\text{NO})(1\text{-MeIm})$ and the formation of a new nitrosyl-containing species when the electrode potential	57

is held at half of the peak reduction potential at 23 °C.

Figure 3.9.	Infrared (a) and UV-visible (b) spectra recorded during the bulk electrolysis (first oxidation) of (T( <i>p</i> -OCH <sub>3</sub> )PP)Mn(NO)(1-MeIm) in CH <sub>2</sub> Cl <sub>2</sub> .	58
Figure 3.10.	Cyclic voltammogram of (T( <i>p</i> -OCH <sub>3</sub> )PP)Mn(NO)(1-MeIm) in CH <sub>2</sub> Cl <sub>2</sub> at -78 °C.	59
Figure 3.11.	Cyclic voltammogram of (T( <i>p</i> -OCH <sub>3</sub> )PP)Mn(NO)(1-MeIm) in THF at 23 °C.	60
Figure 3.12.	NO release from (TTP)Mn(NO)(1-MeIm) (1.7 mM in CH <sub>2</sub> Cl <sub>2</sub> ) after addition of AgBF <sub>4</sub> (10 mM).	64
Figure 4.1.	Final models and final $F_o-F_c$ difference electron density maps showing side views of hh MnMb derivatives.	91
Figure 4.2.	Final model of the Mn-heme environment in Mn <sup>III</sup> Mb(H <sub>2</sub> O), and the $2F_o-F_c$ electron density map, contoured at $1\sigma$ , associated with the two conformations of the distal His64 residue.	92
Figure 4.3.	Final models and final $F_o-F_c$ difference electron density maps showing side views of hh MnMb and CoMb derivatives.	97
Figure 4.4.	A superposition of the heme environments in the crystal structures of hh Co <sup>III</sup> Mb(H <sub>2</sub> O).	99
Figure 4.5.	A superposition of the heme environments in the crystal structures of hh Mn <sup>III</sup> Mb(H <sub>2</sub> O). (a) natural hh Fe <sup>III</sup> Mb(H <sub>2</sub> O) and (b) recombinant hh Fe <sup>III</sup> Mb(H <sub>2</sub> O).	103
Figure 4.6.	A superposition of the heme environments in the crystal structures of hh Mn <sup>III</sup> Mb(H <sub>2</sub> O) and hh Mn <sup>II</sup> Mb.	109
Figure 4.7.	A superposition of the heme environments in the crystal structures of hh Mn <sup>II</sup> Mb and hh Fe <sup>II</sup> Mb.	110

## List of Schemes

Page

Scheme 3.1

73

### List of Abbreviations

<i>bpb</i>	1,2-Bis(pyridine-2-carboximido)benzene dianion
<i>cGMP</i>	Cyclic Guanosine Monophosphate
<i>GTP</i>	Guanosine Triphosphate
<i>Hb</i>	Hemoglobin
<i>Hbk</i>	hemoglobin Kansas
<i>Hh</i>	horse heart
<i>Mb</i>	Myoglobin
<i>Me<sub>2</sub>bpb</i>	1,2-bis(pyridine-2-carboxamido)-4,5-dimethylbenzene dianion
<i>1-Melm</i>	1-Methylimidazole
<i>4-Mepip</i>	4-Methylpiperidine
<i>NBu<sub>4</sub>PF<sub>6</sub></i>	tetra- <i>n</i> -butylammonium hexafluorophosphate
<i>nNOS</i>	Neuronal Nitric Oxide Synthase
<i>NO</i>	Nitric Oxide
<i>OEP</i>	dianion of 2,3,7,8,12,13,17,18-octaethylporphyrin
<i>PGHS</i>	prostaglandin H <sub>2</sub> synthase
<i>Salen</i>	<i>N,N'</i> -ethylenebis(salicylideneiminato) dianion
<i>SCE</i>	saturated calomel electrode
<i>SDS-PAGE</i>	sodium dodecylsulfate polyacrilamide gel electrophoresis
<i>sGC</i>	Soluble Guanylyl Cyclase
<i>Sw</i>	sperm whale
<i>TCPP</i>	Tetracarboxyphenylporphyrin dianion
<i>TDLAS</i>	Tunable diode laser absorption spectroscopy
<i>T(p-OCH<sub>3</sub>)PP</i>	5,10,15,20-tetra- <i>p</i> -methoxyphenylporphyrinato dianion
<i>TPP</i>	5,10,15,20-tetraphenylphyrinato dianion
<i>TTP</i>	5,10,15,20-tetra- <i>p</i> -tolylporphyrinato dianion

## ABSTRACT

This dissertation deals with the interaction of the biologically important nitrogen oxides (nitric oxide and nitrite) with manganese and ruthenium centers in small inorganic porphyrin and nonporphyrin complexes as well as with manganese and cobalt centers in manganese and cobalt substituted myoglobin.

Chapter 1 introduces the fundamental background of the biological importance of nitric oxide, nitrite, manganese porphyrins and manganese-reconstituted myoglobin.

Chapter 2 describes the preparation of the oxo-bridged dimer  $[\text{Ru}(\text{bpb})(\text{NO})_2(\mu\text{-O})]$  in 60% isolated yield from the reaction of the known  $\text{Ru}(\text{bpb})(\text{NO})\text{Cl}$  with silver nitrite. The compound exhibits a  $\nu_{\text{NO}}$  of  $1758\text{ cm}^{-1}$  (KBr pellet). The crystal structure reveals a linear ON-Ru-O-Ru-NO fragment with the oxo atom serving as an inversion center in the molecule. The redox behavior in DMF is characterized by a reversible reduction followed by a second but irreversible reduction in this solvent.

Chapter 3 describes the syntheses of a new set of six-coordinate manganese nitrosyl porphyrins of the general form  $(\text{por})\text{Mn}(\text{NO})(\text{L})$  ( $\text{por} = \text{TTP}, \text{TPP}, \text{T}(p\text{-OCH}_3)\text{PP}$ ;  $\text{L} = \text{piperidine}, \text{methanol}, 1\text{-methylimidazole}$ ) in moderate to high yields. The  $(\text{por})\text{Mn}(\text{NO})(\text{pip})$  complexes were prepared from the reductive nitrosylation of the  $(\text{por})\text{MnCl}$  compounds with NO in the presence of piperidine. The IR spectra of the  $(\text{por})\text{Mn}(\text{NO})(\text{pip})$  compounds as KBr pellets show new strong bands at  $1746\text{ cm}^{-1}$  (for TTP) and  $1748\text{ cm}^{-1}$  (for  $\text{T}(p\text{-OCH}_3)\text{PP}$ ) due to the NO ligands. Attempted crystallization of one of these compounds ( $\text{por} = \text{TTP}$ ) from

dichloromethane/methanol resulted in the generation of the methanol complex (TTP)Mn(NO)(CH<sub>3</sub>OH). Reaction of the (por)Mn(NO)(pip) compounds with excess 1-methylimidazole gave the (por)Mn(NO)(1-MeIm) derivatives in good yields. The IR spectra of these compounds show  $\nu_{\text{NO}}$  bands that are  $\sim 12 \text{ cm}^{-1}$  lower than those of the (por)Mn(NO)(pip) precursors, indicative of greater Mn $\rightarrow$ NO  $\pi$ -backdonation in the 1-MeIm derivatives. X-ray crystal structures of four of these compounds, namely (TTP)Mn(NO)(CH<sub>3</sub>OH), (TTP)Mn(NO)(1-MeIm), (TPP)Mn(NO)(1-MeIm), and (T(*p*-OCH<sub>3</sub>)PP)Mn(NO)(1-MeIm) were obtained, and reveal that the NO ligands in these complexes are linear.

Also we report the room and the low temperature ( $-78 \text{ }^{\circ}\text{C}$ ) cyclic voltammetric behavior of three six coordinate (por)Mn(NO)(1-MeIm) (por = tetraphenylporphyrin dianion (TPP), tetratolylporphyrin dianion (TTP) or tetra-*p*-methoxyphenylporphyrin dianion (T(*p*-OCH<sub>3</sub>)PP)) complexes at a Pt disc electrode in two nonaqueous solvents (CH<sub>2</sub>Cl<sub>2</sub> and THF). In CH<sub>2</sub>Cl<sub>2</sub> at room temperature, the compounds undergo four oxidations and two reductions within the solvent limit; in THF, the compounds undergo one oxidation and three reductions. In both solvents, the first oxidation represents a chemically irreversible one-electron process involving the rapid loss of nitric oxide. The oxidation occurs at the MnNO site as judged from bulk electrolysis, UV-vis spectroscopy at room temperature, and IR-spectroelectrochemistry at room temperature and at  $-78 \text{ }^{\circ}\text{C}$ . The second oxidation, accessible in CH<sub>2</sub>Cl<sub>2</sub>, is also chemically irreversible and occurs at the porphyrin ring; the third and the fourth oxidations are, on the other hand, chemically reversible but also occur at the porphyrin ring. The first reduction is chemically irreversible in

CH<sub>2</sub>Cl<sub>2</sub>, occurs at the porphyrin ring, and is followed by loss of NO. In THF, the first reduction is chemically reversible and is followed by reversible loss of NO.

Chapter 4 describes the 1.6–2.0 Å resolution crystal structures of the as-isolated Mn-substituted horse heart myoglobin (hh Mn<sup>III</sup>Mb), the reduced form hh Mn<sup>II</sup>Mb, and complexes of hh MnMb with methanol, azide, nitric oxide, and nitrite. The Mn<sup>III</sup>Mb compound contains distal pocket water in two positions, one coordinated and the other not coordinated. The reduced form, Mn<sup>II</sup>Mb, lacks a distal pocket water molecule, in contrast to that observed previously for the iron-containing *deoxy*Mb. Interestingly, the structure of the NO adduct suggests a loosely bound NO in the distal pocket; the Mn–N–O moiety is surprisingly bent, and represents the first such distinctly bent metal–NO unit for a natural or synthetic manganese porphyrin complex. Both crystal structures of hh Mn<sup>III</sup>Mb(ONO) and hh Co<sup>III</sup>Mb(ONO) determined in this work also reveal this unusual nitrito coordination mode. In addition, this surprising result for the cobalt case, when compared with nitrite ligand orientations in related model compounds, demonstrates the importance of the Mb distal pocket in orienting the nitrite towards this O-binding mode.

In summary, this dissertation shows that nitric oxide binds to the manganese center in a linear axial fashion in manganese porphyrin model compounds and in a bent tilted fashion in manganese-substituted myoglobin. Nitrite displays the *O*-binding coordination mode to both manganese model compounds and manganese-substituted myoglobin. Although nitrite exhibits the *N*-binding coordination mode in all known cobalt model compounds, it shows *O*-binding mode to cobalt-substituted myoglobin. The *O*-binding mode that nitrite exhibits to manganese- and cobalt-

substituted myoglobin as well as that reported for ferric-myoglobin further demonstrates the crucial role of the distal amino acids in the heme pocket in changing the coordination preferences of ligands to metal center in myoglobin.

## Chapter 1. Introduction

It is now widely recognized that nitric oxide (NO)<sup>1-8</sup> and nitrite (NO<sub>2</sub><sup>-</sup>)<sup>9-13</sup> have a direct relationship to many physiological and pathological processes such as vasodilation, neurotransmission, immune system defense, thrombosis, and ischemia reperfusion. Indeed, the function of NO and NO<sub>2</sub><sup>-</sup> ion in these physiological and pathological processes is tied in with their interactions with heme-containing biomolecules. The active site of these heme-containing biomolecules is either a heme-imidazole active site such as that in hemeoglobin, myoglobin, and soluble guanylyl cyclase or a heme-thiolate active site such as that in cytochrome P450 and nitric oxide synthases.

Studies on the interactions of NO and NO<sub>2</sub><sup>-</sup> ion with metalloporphyrin-imidazole and metalloporphyrin-thiolate model compounds have contributed substantially in understanding the biological chemistry of NO/NO<sub>2</sub><sup>-</sup>-heme protein interactions as well as in understanding their many roles in many disease processes affecting humans. Since iron is the biologically relevant metal, iron porphyrin model compounds have received the greatest attention. However, these studies have been hampered with many difficulties such as the common instability of iron porphyrin nitrosyl complexes, the difficulties in obtaining them in a pure state, and the common mixed spin states of iron nitrosyl moieties in these compounds.

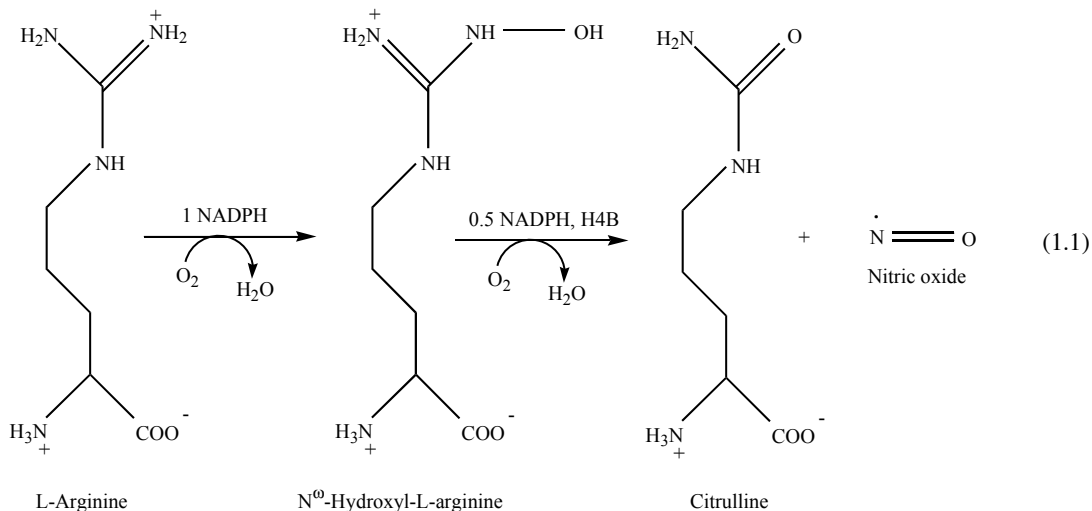
Manganese is only one electron less than iron, and manganese (II) porphyrin complexes are isoelectronic with their iron (III) porphyrin analogues. Also, manganese has been used to replace iron in many heme-containing biomolecules.

However, only few manganese porphyrin nitrosyl and manganese porphyrin nitrite compounds have been reported in the literature. In this dissertation, we focus on the interaction of nitric oxide (NO) and nitrite ion ( $\text{NO}_2^-$ ) with manganese porphyrin model compounds and with manganese and cobalt substituted myoglobin model compounds. In this chapter, we give a brief background about the biology of NO,  $\text{NO}_2^-$  ion, manganese porphyrin and manganese substituted heme proteins.

## 1.1 Nitric Oxide in Biology

The discovery of nitric oxide as a biological molecule was in the late 1980s when the research groups of Ignarro and Moncada revealed that the endothelium-derived relaxing factor (EDRF) proposed by Furchgott is NO.<sup>2,14-16</sup> Like norepinephrine and epinephrine, nitric oxide (NO) is an important intercellular messenger in all vertebrates. It regulates blood flow rate, platelet aggregation, and neuronal activity. NO is produced in most mammalian cell types provided they are appropriately stimulated.<sup>7</sup> It was shown by the Food and Drug Administration that inhaling a low dose of NO gas can be a powerful treatment of persistent pulmonary hypertension in the newborn.<sup>5,17</sup> Two biologically pathways are known for NO biosynthesis; conventional and non-conventional pathways.

In the conventional pathway, nitric oxide is synthesized, in two enzymatic steps, from L-arginine by three heme-containing isozymes of nitric oxide synthases (NOSs) (eq. 1.1). NADPH, tetrahydrobiopterin (H4B), and oxygen are used as cofactors.

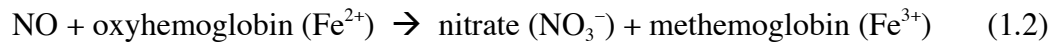


In neuronal cells, nitric oxide is produced by the neuronal nitric oxide synthase (nNOS or NOSI) isozyme. This isozyme was the first NOS that was cloned and purified.<sup>1,18</sup> It has been proposed that NO, in the brain, provides an important signal-averaging mechanism to control synaptic plasticity.<sup>19</sup> Indeed, the nNOS is particularly well suited to produce NO in a manner that facilitates synaptic plasticity.<sup>6</sup>

Nitric oxide production in macrophages was established by Stuehr and Nathan.<sup>3</sup> It is produced by the calcium independent inducible nitric oxide synthase (iNOS or NOSII) isozyme and serves as a defending agent against pathogens after conversion to peroxynitrite ( $\text{ONOO}^-$ ) from the reaction with the superoxide ion in a diffusion-limited non-enzymatic reaction.<sup>20</sup>

In endothelium cells, nitric oxide is produced by the endothelial nitric oxide synthase (eNOS or NOSIII) isozyme.<sup>21,22</sup> It can then rapidly diffuse, through tissues, either into the smooth muscles or into red blood cells.<sup>23,24</sup> In vascular smooth muscles NO activates another heme-containing enzyme, soluble guanylate cyclase (sGC), to produce cyclic guanosine monophosphate (cGMP) from guanosine triphosphate

(GTP). Only 5-10 nM concentration of NO is required to activate the sGC enzyme. Increased levels of cGMP within vascular smooth muscles had been known to allow blood vessels to relax and thus increase blood flow.<sup>14</sup> Indeed, cGMP activates cGMP-dependent kinases in the target tissue that modulates intracellular calcium levels to modulate many diverse activities in the target tissues. In red blood cells most of NO is scavenged rapidly ( $k = 3.4 \times 10^7 \text{ M}^{-1} \text{ s}^{-1}$ )<sup>25</sup> by another heme-containing protein (oxyhemoglobin) and converted to the inert metabolite nitrate ion ( $\text{NO}_3^-$ ) (eq. 1.2).



The oxyhemeoglobin limits the half-life time of NO in vivo to less than a second, and prevents the accumulated NO concentration from directly reacting with oxygen to form significant amounts of nitrogen dioxide (very reactive nitrogen species). A fraction of NO produced by eNOS in the vasculature (approximately 20%) escapes inactivation by hemoglobin and is oxidized to nitrite ion ( $\text{NO}_2^-$ ), another biologically important nitrogen oxide species, in the plasma by a reaction with oxygen.<sup>28</sup> The NO oxidation reaction to nitrite has recently been proposed to be catalyzed by the ceruloplasmin, a multicopper plasma protein.<sup>26</sup>

## 1.2 Nitrite ion in Biology

Nitrite ( $\text{NO}_2^-$ ) is an important inorganic ion for all living organisms. Its typical concentration levels are 0.1-1.0  $\mu\text{M}$  in plasma, 0.5-2.0  $\mu\text{M}$  in tissues and up to 20  $\mu\text{M}$  in vascular tissues.<sup>27-32</sup> Most of the nitrite in mammalian cells comes from exogenous

sources such as food. A small portion comes from the reaction of NO with molecular oxygen as mentioned above.<sup>28</sup> Nitrite can readily modify various biomolecules by, for example, protein and lipid nitration,<sup>33,34</sup> and S-, N-,<sup>31</sup> and Fe- nitrosation.<sup>35,36</sup>

In the meat industry, nitrite ion is used in color fixing and as a protecting agent against botulism. However, it has been reported that nitrite in the digestive system is a source of nitrosoamines that are commonly believed to promote cancer in humans.<sup>37,38</sup> Also, high concentrations of nitrite in the blood stream have been known as a causative agent for methemoglobinemia (loosing the oxygen carrying capability of hemoglobin due to its oxidation to *met*-hemoglobin).<sup>39</sup>

Recently, evidence has accumulated that nitrite ion has beneficial effects under conditions of low oxygen in physiological processes such as ischemia reperfusion and hypoxic vasodilation and these effects are attributed to the reduction of nitrite back to NO.<sup>10,27,40</sup> Non-enzymatic and enzymatic mechanisms have been proposed to explain this reduction. The non-enzymatic reduction is very slow<sup>41</sup> except under high acidic conditions that might only be found in stomach,<sup>42,43</sup> urine,<sup>44</sup> or ischemic tissue.<sup>45,46</sup> In the enzymatic reduction, certain mammalian enzymes catalyze the reduction of nitrite to NO. Examples are glutathione-S-transferase,<sup>47</sup> xanthine oxidoreductase,<sup>48-50</sup> deoxyhemoglobin, deoxymyoglobin,<sup>27,51-55</sup> cytochrome P450,<sup>56</sup> and nitric oxide synthases.<sup>57,58</sup>

Modeling the interaction of nitrite with heme-containing biomolecules will contribute in our understanding of the nitrite reduction mechanism. In Chapter 4 of this dissertation, structural details of the interaction of nitrite with manganese- and cobalt-reconstituted myoglobin are discussed.

### 1.3 Manganese porphyrins and manganese proteins

Manganese is a required trace element for all known living organisms. It is essential for many biological processes such as bone and tissue formation, reproductive processes, and carbohydrate and lipid metabolism.<sup>59</sup> It is a cofactor for a number of metalloenzymes such as arginase, catalase, ribonucleotide reductase, enolase, superoxide dismutase and the oxygen-evolving complex of photosystem II.<sup>60-</sup>  
<sup>63</sup> Humans have a mean manganese concentration of  $9.03 \pm 2.25$  mg/L in whole blood with a mean concentration of  $1.82 \pm 0.64$  mg/L in the serum.<sup>64</sup>

Fifty years ago, Borg and Cotzias discovered that injection of radiolabeled  $^{54}\text{MnCl}_2$  into patients *in vivo* resulted in the incorporation of  $\text{Mn}^{2+}$  into red cell fractions, and that the incorporated  $\text{Mn}^{2+}$  was non-exchangeable and non-dialyzable.<sup>65-</sup>  
<sup>67</sup> Based on their data, they suggested that the  $\text{Mn}^{2+}$  was most likely incorporated into heme, thus providing some circumstantial evidence for the production of a natural manganese heme in humans.<sup>68</sup> Mahoney and Sargent confirmed this finding, and showed that between 0.5-9.0% of administered radiolabeled  $^{54}\text{Mn}$  was incorporated into red blood cells, and that 60-70% of the radioactivity was recovered in the resulting crystalline hemin preparation.<sup>69</sup> Hancock and Fritze later showed that, indeed, injection of  $^{54}\text{MnCl}_2$  into rats resulted in the formation of a  $^{54}\text{Mn}$ -containing species that had identical gel chromatographic elution behavior as hemoglobin, bis-pyridine hemochrome and hematin;<sup>70</sup> this provided further evidence for the *in vivo* formation of a manganese porphyrin, confirming the earlier results of Borg and Cotzias. These authors noted, however, that added  $\text{Mn}^{2+}$  was not able to displace iron from heme by a simple metal displacement reaction, suggesting the incorporation of

Mn<sup>2+</sup> at the heme biosynthesis stage. In a separate study, Wibowo *et al.* determined that increased levels of protoporphyrin in erythrocytes (induced by exposure to Pb) resulted in incorporation of *in vivo* manganese by the porphyrin.<sup>71</sup> In metal ion accumulation studies using Norway lobsters, it was determined that exposure of the lobsters to Mn<sup>2+</sup> resulted in accumulation of the metal ion in nerve tissue, and in the hemolymph where it was bound mainly to the respiratory protein hemocyanin (the authors noted that Mn<sup>2+</sup> was not able to displace copper in the protein).<sup>72</sup>

Manganese-substituted derivatives of a number of heme proteins have been prepared and studied. In many cases, these Mn-substituted derivatives were investigated in order to provide insight on the role of heme iron in the reactions of the native proteins.<sup>73</sup> Manganese-substituted derivatives of heme proteins that have been reported to date include those of hemoglobin (Hb),<sup>74,75</sup> myoglobin (Mb),<sup>76-78</sup> cytochrome P450,<sup>79</sup> soluble guanylyl cyclase,<sup>80</sup> cytochrome *c*,<sup>81</sup> nitric oxide synthase,<sup>82</sup> horse radish peroxidase,<sup>75,77,83</sup> cytochrome *b*<sub>5</sub>,<sup>84</sup> cytochrome *c* peroxidase (CcP),<sup>77,85,86</sup> and prostaglandin H<sub>2</sub> synthase-1.<sup>87</sup>

Unlike the native iron analogues, Mn<sup>II</sup>-substituted hemoglobin (Mn<sup>II</sup>Hb) and – myoglobin (Mn<sup>II</sup>Mb) *do not* bind dioxygen or carbon monoxide,<sup>77</sup> although the Mn<sup>III</sup>-derivatives bind azide.<sup>77,88-90</sup> Mitra and coworkers have shown that Mn<sup>III</sup>Mb binds cyanide and thiocyanate at a location > 6Å from the metal center.<sup>91</sup>

Clearly, Mn porphyrins are becoming increasingly recognized for their potential biological applications. The fact that Mn<sup>II</sup> is incorporated into heme at the biosynthesis level (mentioned above) raises an intriguing possibility that Mn-hemes might be of some physiological importance, although their function (if any) remains

unknown. Despite numerous reports on the spectroscopy of Mn-substituted heme proteins, there are only a few reports of crystal structures of these complexes. Moffat and coworkers reported the structure of MnHb using X-ray difference Fourier techniques<sup>92,93</sup> and demonstrated the similarity of the structure of this complex to that of the native iron compound. Arnone later reported the 3.0 Å resolution structure of the heterometallic complex Hb( $\alpha$ -Fe<sup>II</sup>CO)( $\beta$ -Mn<sup>II</sup>).<sup>94</sup> Very recently, Loll and coworkers reported the 2.0 Å resolution crystal structure of Mn-PGHS.<sup>87</sup>

This dissertation is organized as follows. Chapter 2 describes the synthesis, characterization, molecular structure, and electrochemical properties of an oxo-bridged dimer of a ruthenium nitrosyl compound containing the bpb ligand system. Chapter 3 describes the synthesis, characterization, molecular structures, and fiber-optic IR-spectroelectrochemical properties of a series of six-coordinate manganese porphyrin nitrosyl complexes containing three different axial ligands, piperidine, methanol, and 1-methylimidazole and three different porphyrin ligands, TPP, TTP, and T(*p*-OCH<sub>3</sub>)PP. Chapter 4 describes the ligand conformations in derivatives of manganese- and cobalt-substituted horse heart myoglobin as determined by X-ray crystallography.

#### 1.4 References

- (1) Brecht, D. S.; Snyder, S. H. *Proc Natl Acad Sci USA* **1989**, *86*, 9030–9033.
- (2) Ignarro, L. J. *Semin Hematol* **1989**, *26*, 63–76.
- (3) Stuehr, D. J.; Nathan, C. F. *J Exp Med* **1989**, *169*, 1543–1555.
- (4) Marietta, M. A.; Yoon, P. S.; Iyengar, R.; Leaf, C. D.; Wishnok, J. S. *Biochemistry* **1988**, *27*, 8706–8711.
- (5) Frostell, D.; Fratacci, M. D.; Wain, J. C.; Jones, R.; Zapol, W. M. *Circulation* **1991**, *83*, 2038–2047.

- (6) Southam, E.; East, S. J.; Garthwaite, J. *J Neurochem* **1991**, *56*, 2072–2081.
- (7) Nathan, C. *FASEB J.* **1992**, *6*, 3051-3064.
- (8) Phelan, M. W.; Faller, D. V. *J. Cell. Physiol.* **1996**, *167*, 469-476.
- (9) Dejam, A.; Hunter, C. J.; Pelletier, M. M.; Hsu, L. L.; Machado, R. F.; Shiva, S.; Power, G. G.; Kelm, M.; Gladwin, M. T.; Schechter, A. N. *BLOOD* **2005**, *106*, 734-739.
- (10) Webb, A.; Bond, R.; McLean, P.; Uppal, R.; Benjamin, N.; Ahluwalia, A. *PNAS* **2004**, *101*, 13683–13688.
- (11) Hunter, C. J.; Dejam, A.; Blood, A. B.; Shields, H.; Kim-Shapiro, D.; Machado, R. F.; Tarekegn, S.; Mulla, N.; Hopper, A. O.; Schechter, A. N.; Power, G. G.; Gladwin, M. T. *Nature medicine* **2004**, *10*, 1122-1127.
- (12) Gladwin, M. T. *The Journal of Clinical Investigation* **2004**, *113*, 19-21.
- (13) Dejam, A.; Hunter, C. J.; Schechter, A. N.; Gladwin, M. T. *Blood Cells, Molecules, and Diseases* **2004**, *32*, 423-429.
- (14) Ignarro, L. J.; Adams, J. B.; Horwitz, P. M.; Wood, K. S. *J Biol Chem* **1986**, *261*, 4997–5002.
- (15) Ignarro, L. J.; Harbison, R. G.; Wood, K. S.; Kadowitz, P. J. *J Pharmacol Exp Ther* **1986**, *237*, 893–900.
- (16) Moncada, S.; Herman, A. G.; Vanhoutte, P. M. *Trends Pharmacol Sci* **1987**, *8*, 365–368.
- (17) Ballard, R. A.; Truog, W. E.; Cnaan, A.; Martin, R. J.; Ballard, P. L.; Merrill, J. D.; Walsh, M. C.; Durand, D. J.; Mayock, D. E.; Eichenwald, E. C., .; Null, D. R.; Hudak, M. L.; Puri, A. R.; Golombek, S. G.; Courtney, S. E.; Stewart, D. L.; Welty, S. E.; Phibbs, R. H.; Hibbs, A. M.; Luan, X.; Wadlinger, S. R.; Asselin, J. M.; Coburn, C. E. *N Engl J Med* **2006**, *355*, 343–353.
- (18) Brecht, D. S.; Synder, H. S. *Proc Natl Acad Sci USA* **1990**, *87*, 682–685.
- (19) Gally, J. A.; Montague, P. R.; Reeke, G. N.; Jr Edelman, G. M. *Proc Natl Acad Sci USA* **1990**, *87*, 3547–3551.
- (20) Huie, R. E.; Padmaja, S. *Free Rad Res Commun* **1993**, *18*, 195–199.
- (21) Furchgott, R. F.; Zawadzki, J. V. *Nature* **1980**, *288*, 373-376.
- (22) Palmer, R. M.; Ferrige, A. G.; Moncada, S. *Nature* **1987**, *327*, 524-526.
- (23) Joshi, M. S.; Ferguson, T. B.; Jr. Han, T. H.; Hyduke, D. R.; Liao, J. C.; Rassaf, T.; Bryan, N.; Feelisch, M.; Lancaster, J. R. J. *Proc Natl Acad Sci USA* **2002**, *99*, 10341–10346.
- (24) Butler, A. R.; Megson, I. L.; Wright, P. G. *Biochim Biophys Acta* **1998**, *1425*, 168–176.
- (25) Kim-Shapiro, D. B.; Schechter, A. N.; Gladwin, M. T. *Arterioscler. Thromb. Vasc. Biol.* **2006**, *26*, 697-705.
- (26) Shiva, S.; Wang, X.; Ringwood, L. A.; Xu, X.; Yuditskaya, S.;

- Annavaajhala, V.; Miyajima, H.; Hogg, N.; Harris, Z. L.; Gladwin, M. T. *Nature Chemical Biology* **2006**, *2*, 486-493.
- (27) Duranski, M. R.; Greer, J. J. M.; Dejam, A.; Jaganmohan, S.; Hogg, N.; Langston, W.; Patel, R. P.; Yet, S.-F.; Wang, X.; Kevil, C. G.; Gladwin, M. T.; Lefer, D. J. *The Journal of Clinical Investigation* **2005**, *115*, 1232-1240.
- (28) Kelm, M. *Biochim. Biophys. Acta* **1999**, *1411*, 273-289.
- (29) Gladwin, M. T.; Shelhammer, J. H.; Schechter, A. N.; Pease-Fye, M. E.; Wadawiw, M. A.; Panza, J. A.; Ognibene, F. P.; Cannon III, R. O. *Proc. Natl. Acad. Sci. USA* **2000**, *97*, 11482-11487.
- (30) Lauer, T.; Preik, M.; Rassaf, T.; Strauer, B.; Deussen, A.; Feelisch, M.; Kelm, M. *Proc. Natl. Acad. Sci. USA* **2001**, *98*, 12814-12819.
- (31) Bryan, N. S.; Rassaf, T.; Maloney, R. E.; Rodriguez, C. M.; Saijo, F.; Rodriguez, J. R.; Feelisch, M. *Proc. Natl. Acad. Sci. USA* **2004**, *101*, 4308-4313.
- (32) Rodriguez, J.; Maloney, R.; Rassaf, T.; Bryan, N.; Feelisch, J. *Proc. Natl. Acad. Sci. USA* **2003**, *100*, 336-341.
- (33) O'Donnell, V. B. e. a. *Chem. Res. Toxicol.* **1999**, *12*, 83-92.
- (34) Hazen, S. L. e. a. *Circ. Res.* **1999**, *85*, 950-958.
- (35) Huang, K. T.; Keszler, A.; Patel, N.; Patel, R. P.; Gladwin, M. T.; Kim-Shapiro, D. B.; Hogg, N. *J. Biol. Chem.* **2005**, *280*, 31126-21131.
- (36) Huang, Z.; Shiva, S.; Kim-Shapiro, D. B.; Patel, R. P.; Ringwood, L. A.; Irby, C. E.; Huang, K. T.; Ho, C.; Hogg, N.; Schechter, A. N.; Gladwin, M. T. *The Journal of Clinical Investigation* **2005**, *115*, 2099-2107.
- (37) Fox, J. B. *Crit. Rev. CRC, Anal. Chem.* **1983**, *15*, 283-.
- (38) Dumham, A. J.; Barkley, R. M.; Sievers, R. E. *Anal. Chem.* **1995**, *67*, 67.
- (39) Jaffe, R. E. *Clin. Haematol.* **1981**, *10*, 99.
- (40) Tiravanti, E.; Samouilov, A.; Zweier, J. J. *J. Biol. Chem.* **2004**, *279*, 11065-11073.
- (41) Samouilov, A.; Kuppusamy, P.; Zweier, J. *Arch. Biochem. Biophys.* **1998**, *357*, 1-7.
- (42) McKnight, G.; Smith, L.; Drummond, R.; Duncan, C.; Golden, M.; Benjamin, N. *Gut* **1997**, *40*, 211-214.
- (43) Tsuchiya, K.; Kanematsu, Y.; Yoshizumi, M.; Ohnishi, H.; Kirima, K.; Izawa, Y.; Shikishima, M.; Ishida, T.; Kondo, S.; Kagami, S.; Takiguchi, Y.; Tamaki, T. *Am. J. Physiol. Heart Circ. Physiol.* **2005**, *288*, H2163-H2170.
- (44) Lundberg, J.; Carlsson, S.; Engstrand, L.; Morcos, E.; Wiklund, N.; Weitzberg, E. *Urology* **1997**, *50*, 189-191.
- (45) Zweier, J.; Wang, P.; Samouilov, A.; Kuppusami, P. *Nat. Med.* **1995**, *1*, 804-809.
- (46) Dennis, S. C.; Gevers, W.; Opie, L. *J. Mol. Cell Cardiol.* **1991**, *23*, 1077-1086.
- (47) Hill, K.; Hunt, R.; Jones, R.; Hoover, R. L.; Burk, R. F. *Biochem.*

- Pharmacol* **1992**, *43*, 561–566.
- (48) Millar, T. M.; Stevens, C.; Benjamin, M.; Eisenthal, R.; Harrison, R.; Blake, D. R. *FEBS Lett.* **1998**, *427*, 225–228.
- (49) Godber, B. L. J.; Doel, J. J.; Sapkota, G. P.; Blake, D. R.; Stevens, C. R.; Eisenthal, R.; Harrison, R. *J. Biol. Chem.* **2000**, *275*, 7757–7763.
- (50) Li, H.; Samouilov, A.; Liu, X.; Zweier, J. *Biochemistry* **2003**, *42*, 1150–1159.
- (51) Cosby, K.; Partovi, K. S.; Crawford, J. H.; Patel, R. P.; Reiter, C. D.; Martyr, S.; Yang, B. K.; Waclawiw, M. A.; Zalos, G.; Xu, X.; Huang, K. T.; Shields, M.; Kim-Shapiro, D. B.; Schechter, A. N.; Cannon III, R. O.; Gladwin, M. T. *Nature Medicine* **2003**, *9*, 1498–1505.
- (52) Gladwin, M. T.; Schechter, A. N.; Kim-Shapiro, D. B.; Patel, R. P.; Hogg, N.; Shiva, S.; Cannon 3rd, R. O.; Kelm, M.; Wink, D. A.; Espey, M. G.; Oldfield, E. H.; Pluta, R. M.; Freeman, B. A.; Lancaster Jr., J. R.; Feelisch, M.; Lundberg, J. O. *Nat. Chem. Biol.* **2005**, *1*, 308.
- (53) Gladwin, M.; Shelhamer, J.; Schechter, A.; Pease-Fye, M.; Waclawiw, M.; Panza, J.; Ognibene, F.; Cannon, R. I. *Proc. Natl. Acad. Sci. USA* **2000**, *97*, 11482–11487.
- (54) Doyle, M. P.; Pickering, R. A.; DeWeert, T. M.; Hoekstra, J. W.; Pater, D. *J. Biol. Chem.* **1981**, *256*, 12393–12398.
- (55) Luchsinger, B. P.; Rich, E. N.; Yan, Y.; Williams, E. M.; Stamler, J. S.; Singel, D. J. *J. Inorg. Biochem.* **2005**, *99*, 912–921.
- (56) Delaforge, M.; Servent, D.; Wirsta, P.; Ducrocq, C.; Mansuy, D.; Lenfant, M. *Chem. Biol. Interact.* **1993**, *86*, 103–117.
- (57) Vanin, A. F.; Bevers, L. M.; Slama-Schwok, A.; van Faassen, E. E. *Cell. Mol. Life Sci.* **2007**, *64*, 96–103.
- (58) Gautier, C.; van Faassen, E.; Mikula, I.; Martasek, P.; Slama-Schwok, A. *Biochemical and Biophysical Research Communications* **2006**, *341*, 816–821.
- (59) Leach, R. M.; Lilburn, M. S. *World Rev. Nutr. Diet.* **1978**, *32*, 123.
- (60) Dismukes, G. C. *Chem. Rev.* **1996**, *96*, 2909–2926.
- (61) Holm, R. H.; Kennepoh, P.; Solomon, E. I. *Chem. Rev.* **1996**, *96*, 2239–2314.
- (62) Wu, A. J.; Penner-Hahn, J. E.; Pecoraro, V. L. *Chem. Rev.* **2004**, *104*, 903–938.
- (63) Yachandra, V. K.; Sauer, K.; Klein, M. P. *Chem. Rev.* **1996**, *96*, 2927–2950.
- (64) Pleban, P. A.; Pearson, K. H. *Clin. Chem.* **1979**, *25*, 1915–1918.
- (65) Borg, D. C.; Cotzias, G. C. *Nature* **1958**, *182*, 1677–1678.
- (66) Borg, D. C.; Cotzias, G. C. *Med. Res. Center, Brookhaven Natl. Lab., Upton, L. I. N. Y.*, 1850.
- (67) Borg, D. C.; Cotzias, G. C. *J. Clin. Invest.* **1958**, *37*, 1269–1278.
- (68) Borg, D. C.; Cotzias, G. C. *Fed. Proc.* **1959**, *18*, 470.
- (69) Mahoney, J. P.; Sargent, K. *J. Clin. Invest.* **1967**, *46*, 1090.
- (70) Hancock, R. G. V.; Fritze, K. *Bioinorg. Chem.* **1973**, *3*, 77–87.

- (71) Wibowo, A. A. E.; Salle, H. J. A.; del Castiho, P.; Zielhuis, R. L. *Int. Arch. Occup. Environ. Health* **1979**, *43*, 177-182.
- (72) Baden, S. P.; Neil, D. M. *Comp. Biochem. Physiol. A: Mol. Integr. Physiol.* **1998**, *119A*, 351-359.
- (73) Boucher, L. J. *Coord. Chem. Rev.* **1972**, *7*, 289-329.
- (74) Fabry, T. L.; Simo, C.; Javaherian, K. *Biochim. Biophys. Acta* **1968**, *160*, 118-122.
- (75) Yonetani, T.; Drott, H. R.; Leigh, J. S., Jr.; Reed, G. H.; Waterman, M. R.; Asakura, T. *J. Biol. Chem.* **1970**, *245*, 2998-3003.
- (76) Atassi, M. Z. *Biochem. J.* **1967**, *103*, 29-35.
- (77) Yonetani, T.; Asakura, T. *J. Biol. Chem.* **1969**, *244*, 4580-4588.
- (78) Breslow, E. *J. Biol. Chem.* **1964**, *239*, 486-496.
- (79) Gelb, M. H.; Toscano, W. A., Jr.; Sligar, S. G. *Proc. Natl. Acad. Sci. U.S.A* **1982**, *79*, 5758-5762.
- (80) Dierks, E. A.; Hu, S.; Vogel, K. M.; Yu, A. E.; Spiro, T. G.; Burstyn, J. N. *J. Am. Chem. Soc.* **1997**, *119*, 7316-7323.
- (81) Dickinson, L. C.; Chien, J. C. W. *J. Biol. Chem.* **1977**, *252*, 6156-6162.
- (82) Hemmens, B.; Gorren, A. C. F.; Schmidt, K.; Werner, E. R.; Mayer, B. *Biochem. J.* **1998**, *332*, 337-342.
- (83) Theorell, H. *Nature (London)* **1945**, *156*, 474.
- (84) Ozols, J.; Strittmatter, P. *J. Biol. Chem.* **1964**, *239*, 1018-???
- (85) Yonetani, T. *J. Biol. Chem.* **1967**, *242*, 5008-5013.
- (86) Yonetani, T.; Asakura, T. *J. Biol. Chem.* **1968**, *243*, 3996-3998.
- (87) Gupta, K.; Selinsky, B. S.; Loll, P. J. *Acta Cryst.* **2006**, *D62*, 151-156.
- (88) Keilin, D. *Proc. Roy. Soc. B* **1936**, *121*, 165-173.
- (89) Hoffman, B. M.; Gibson, Q. H.; Bull, C.; Crepeau, R. H.; Edelstein, S. J.; Fisher, R. G.; McDonald, M. J. *Ann. N. Y. Acad. Sci.* **1975**, *244*, 174-186.
- (90) Hoffman, B. M.; Gibson, Q. H. *Biochemistry* **1976**, *15*, 3405-3410.
- (91) Mondal, M. S.; Mazumdar, S.; Mitra, S. *Inorg. Chem.* **1993**, *32*, 5362-5367.
- (92) Moffat, K.; Loe, R. S.; Hoffman, B. M. *J. Mol. Biol.* **1976**, *104*, 669-685.
- (93) Moffat, K.; Loe, R. S.; Hoffman, B. M. *J. Am. Chem. Soc.* **1974**, *96*, 5259-5261.
- (94) Arnone, A.; Rogers, P.; Blough, N. V.; McGourty, J. L.; Hoffman, B. M. *J. Mol. Biol.* **1986**, *188*, 693-706.

## Chapter 2. Synthesis, Molecular Structure, and Redox Behavior of an oxo-bridged dimer of a Ruthenium-bpb Nitrosyl\*

### 2.1 Introduction

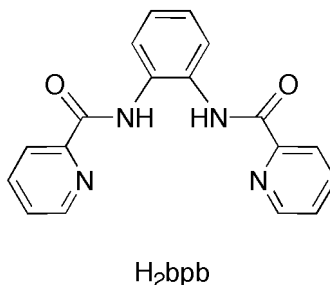
Nitrosyl complexes of the group 8 metals have been studied for many decades.<sup>1,2</sup> This is due in large part to the fact that the interaction of nitric oxide (NO) with iron is biologically relevant both for heme and non-heme proteins.<sup>3</sup> The use of synthetic models in the study of the heme-NO interactions has provided a wealth of information concerning the electronic structure and the predicted geometries of the FeNO moiety in these systems. However, a common byproduct of iron porphyrin chemistry in aerobic environments is the  $\mu$ -oxo dimer [(porphyrinato)Fe]<sub>2</sub>( $\mu$ -O). Several of these iron porphyrin oxo-bridged dimers have been characterized by X-ray crystallography.<sup>4,7</sup>

In 1998, our group described an unexpected product formed during work with organoosmium nitrosyl porphyrins.<sup>4</sup> This product, namely [(OEP)Os(NO)]<sub>2</sub>( $\mu$ -O) (OEP = octaethylporphyrinato dianion) was characterized by spectroscopy and by X-ray crystallography, and displayed a linear oxo-bridged ON-Os-O-Os-NO linkage. This product was found to be rather unreactive towards acid, and this lack of reactivity of the oxo-bridge was attributed to the removal of electron-density in this bridge by the two *trans* NO ligands. We have not, to date, been successful at obtaining the corresponding ruthenium analogue [(porphyrinato)Ru(NO)]<sub>2</sub>( $\mu$ -O).

---

\* Taken in part from "Synthesis, molecular structure, and redox behavior of an oxo-bridged dimer of a ruthenium-bpb nitrosyl" Zahran, Z. N.; Powell, D. R.; Richter-Addo, G. B. *Inorg. Chim. Acta* **2006**, 359, 3084–3088, with permission from Elsevier.

1,2-Bis(pyridine-2-carboximido)benzene ( $H_2bpb$ ) and its various derivatives have been extensively employed as tetradentate diamide ligands for various transition metal ions. Mascharak and coworkers have utilized the  $H_2bpb$  ligand for the design and construction of metal nitrosyl complexes that behave as NO-donors under



mild photochemical conditions.<sup>8</sup> Importantly, they have investigated possible similarities between the  $H_2bpb$  ligand and porphyrin ligands.<sup>9</sup> Ford,<sup>10,11</sup> and Mascharak,<sup>8,12-15</sup> have published extensively on the photochemical release of NO from group 8 metal-NO compounds with related polydentate ligands.

Based on the work of Mascharak, we explored the possibility of designing ( $bpb$ )Ru(NO)-containing compounds that will complement our work on ruthenium nitrosyl porphyrins. In this chapter, we describe (i) the preparation and spectroscopic properties of an oxo-bridged dimer of a ruthenium nitrosyl compound containing the  $bpb$  ligand system, (ii) its crystal structure, and (iii) its electrochemical properties.

## 2.2 Experimental Section

**2.2.1 General.** All reactions were performed under an atmosphere of prepurified nitrogen using standard Schlenk glassware and/or in an Innovative

Technology Labmaster 100 Dry Box. Solutions for spectral studies were also prepared under a nitrogen atmosphere. Solvents were distilled from appropriate drying agents under nitrogen just prior to use.

**2.2.2 Chemicals.** 1,2-Bis(pyridine-2-carboxamido)benzene ( $H_2bpb$ )<sup>16</sup> and  $Ru(bpb)(NO)Cl$ <sup>8</sup> were prepared by the literature methods. Silver nitrite, tetra-*n*-butylammonium hexafluorophosphate ( $NBu_4PF_6$ ), and anhydrous DMF were purchased from Aldrich Chemical Company and used as received. Chloroform-*d* (99.8%) was obtained from Cambridge Isotope Laboratories. Diethyl ether,  $CH_2Cl_2$  and THF were distilled from calcium hydride under a nitrogen atmosphere just prior to use. Nitrogen of ultra high purity was purchased from Trigas (Houston, TX).

**2.2.3 Instrumentation.** Infrared spectra were recorded on a Bio-Rad FT-155 FTIR spectrometer. Proton NMR spectra were obtained on Varian Mercury VX 300 MHz spectrometer and the signals referenced to the residual signal of the solvent employed ( $CHCl_3$  at  $\delta$  7.24 ppm). ESI mass spectra were obtained on a Micromass Q-TOF mass spectrometer. UV-vis spectra were recorded on a Hewlett-Packard model 8453 diode array instrument. Electrochemical measurements were performed with a BAS CV-50W instrument. A three-electrode cell was used (Pt working and auxiliary electrodes, Ag/AgCl reference electrode). The solutions used were 1.0 mM in analyte in 10 ml of 0.1 M  $NBu_4PF_6$ . Nitrogen gas was bubbled through the solution for about 8 min before each set of measurements and was passed continuously over the surface of the solution during the measurements.

**2.2.4 Synthesis of  $[(bpb)Ru(NO)]_2(\mu-O)$ .** A solution of  $AgNO_2$  (0.06 g, 0.4 mmol) in DMF (10 mL) was added slowly, via cannula, to a solution of

Ru(bpb)(NO)Cl (0.20 g, 0.4 mmol) in DMF (5 mL). The mixture was stirred under nitrogen gas overnight at room temperature. Dichloromethane (30 ml) was added, whereby a white precipitate formed. The solution was filtered, and filtrate was heated at  $\sim 100$  °C under vacuum to remove the solvent. The IR spectrum of the residue showed two bands in the  $\nu_{\text{NO}}$  region at  $1758\text{ cm}^{-1}$  (major) and  $1840\text{ cm}^{-1}$  (minor). The residue was washed several times with  $\text{CH}_2\text{Cl}_2$  to remove an as-yet uncharacterized byproduct. The remaining orange residue, after the wash with  $\text{CH}_2\text{Cl}_2$ , was dried under vacuum for several hours to give the orange-red compound  $[(\text{bpb})\text{Ru}(\text{NO})]_2(\mu\text{-O})$  (0.11 g, 60% yield based on Ru). IR (KBr,  $\text{cm}^{-1}$ ):  $\nu_{\text{NO}} = 1758$  vs,  $\nu_{\text{Ru-O-Ru}} = 816$ s; also 3057vw, 2984 vw, 1631vs, 1595vs, 1563s, 1470s, 1447w, 1372s, 1359w, 11268vw, 1112vw, 1092vw, 1028w, 970w, 745w, 725w, 693vw, 682w, 653vw, 571w, 512w, 452vw.  $^1\text{H NMR}$  ( $\text{CDCl}_3$ ;  $\delta$ , ppm): 8.28 (m, 4H), 8.07 (m, 2H), 8.05 (m, 2H), 7.93–7.84 (overlapping m, 8H), 7.30 (m, 4H), 6.93 (m, 4H); also, 5.29 (s, trace  $\text{CH}_2\text{Cl}_2$ ) and 1.57 (s, trace  $\text{H}_2\text{O}$ ). ESI mass spectrum:  $m/z$  913.0  $[(\text{Ru}(\text{bpb})\text{NO})_2\text{O} + \text{H}]^+$  (100%).

The complex is soluble only in DMF and insoluble or only sparingly soluble in most organic solvents.

**2.2.5 X-ray crystallography.** Suitable crystals for X-ray crystallography were grown by vapor diffusion of  $\text{CH}_2\text{Cl}_2$  (25 ml) into a DMF solution of the compound at room temperature under inert atmosphere. A red prism-shaped crystal of dimensions 0.16 x 0.10 x 0.10 mm was selected for structural analysis. Intensity data for this compound were collected at 90(2) K using an instrument with a Bruker APEX CCD

area detector<sup>17,18</sup> using graphite-monochromated Mo K $\alpha$  radiation ( $\lambda = 0.71073 \text{ \AA}$ ). Cell parameters were determined from a non-linear least squares fit of 5577 peaks in the range  $2.27 < \theta < 28.18^\circ$ . A total of 15194 data were measured in the range  $2.09 < \theta < 26.00^\circ$  using  $\omega$  oscillation frames. The data were corrected for absorption by the semi-empirical method<sup>19</sup> giving minimum and maximum transmission factors of 0.840 and 0.897. The data were merged to form a set of 3859 independent data with  $R(\text{int}) = 0.0234$  and a coverage of 100.0 %. The monoclinic space group  $P2_1/n$  was determined by systematic absences and statistical tests, and verified by subsequent refinement. The structure was solved by direct methods and refined by full-matrix least-squares methods on  $F^2$ .<sup>20</sup> Hydrogen atom positions were initially determined by geometry and refined by a riding model. Non-hydrogen atoms were refined with anisotropic displacement parameters. Hydrogen atom displacement parameters were set to 1.2 times the displacement parameters of the bonded atoms. A total of 305 parameters were refined against 7 restraints and 3859 data to give  $wR(F^2) = 0.0541$  and  $S = 1.001$  for weights of  $w = 1/[\sigma^2(F^2) + (0.0280 P)^2 + 1.5000 P]$ , where  $P = [F_o^2 + 2F_c^2] / 3$ . The final  $R(F)$  was 0.0211 for the 3587 observed,  $[F > 4\sigma(F)]$ , data. The largest shift/s.u. was 0.002 in the final refinement cycle. The final difference map had maxima and minima of 0.341 and  $-0.344 \text{ e/\AA}^3$ , respectively. Details of the crystal data and structure refinement are given in Table 2.1. Thermal ellipsoids are drawn at 50% level.

**Table 2.1.** Crystal Data and Structure Refinement of [(bpb)Ru(NO)]<sub>2</sub>O·CH<sub>2</sub>Cl<sub>2</sub>

Formula	(C <sub>36</sub> H <sub>24</sub> N <sub>10</sub> O <sub>7</sub> Ru <sub>2</sub> )·(CH <sub>2</sub> Cl <sub>2</sub> ) <sub>2</sub> C <sub>38</sub> H <sub>28</sub> Cl <sub>4</sub> N <sub>10</sub> O <sub>7</sub> Ru <sub>2</sub>
Fw	1080.64
<i>T</i> (K)	90(2)
Crystal system	Monoclinic
Space group	<i>P</i> 2 <sub>1</sub> / <i>n</i>
<i>a</i> (Å), α (°)	10.1710(14), 90
<i>b</i> (Å), β (°)	12.7547(18), 97.919(5)
<i>c</i> (Å), γ (°)	15.256(2), 90
<i>V</i> , <i>Z</i> , <i>Z</i>	1960.3(5) Å <sup>3</sup> , 2, 0.5
<i>D</i> (calcd), mg/m <sup>3</sup>	1.831
Abs coeff, mm <sup>-1</sup>	1.109 mm
F(000)	1076
Crystal size (mm)	0.16 x 0.10 x 0.10
θ range for data collection, deg	2.09 -26.00
Reflections collected	15194
Independent reflns	3859 [R(int) = 0.0234]
Max and min trans.	0.897 and 0.840
Data / restraints / parameters	3859 / 7 / 305
Goodness-of-fit on F <sup>2</sup>	1.001
Largest and mean shift / s.u.	0.002 and 0.000
R indices (all data)	R1 = 0.0211, wR2 = 0.0541
Largest diff. peak and hole, eÅ <sup>-3</sup>	0.341 and -0.344
Observed data [I > 2σ(I)]	3587

$$wR2 = \{ S [w(F_o^2 - F_c^2)^2] / S [w(F_o^2)^2] \}^{1/2}$$

$$R1 = S ||F_o| - |F_c|| / S |F_o|$$

## 2.3 Results and Discussion

**2.3.1 Synthesis and spectroscopy of  $[(bpb)Ru(NO)]_2(\mu-O)$ .** Several years ago, Bohle and coworkers<sup>21</sup> reported the preparation of  $(TTP)Ru(NO)(ONO)$  in 60% yield from the metathesis reaction of the precursor  $(TTP)Ru(NO)Cl$  with silver nitrite. In our attempt to generate an analogous  $Ru(bpb)(NO)(ONO)$  complex, we reacted  $Ru(bpb)(NO)Cl$  with silver nitrite in DMF. The product obtained after workup, in 60% yield, was the oxo-bridged dimer  $[Ru(bpb)(NO)]_2(\mu-O)$ . The production of this oxo-bridged dimer from the use of a nitrite reagent is not unusual. For example, Ankers and Fanning<sup>22</sup> have reported that ferric salen complexes (salen =  $N,N'$ -ethylenebis(salicylideneiminato) dianion) react with nitrite reagents to generate the  $[Fe(salen)]_2(\mu-O)$  species, and that no evidence for the target nitrite adducts was obtained.

The IR spectrum of  $[Ru(bpb)(NO)]_2(\mu-O)$  as a KBr pellet shows a strong band at  $1758\text{ cm}^{-1}$  attributed to  $\nu_{NO}$ . This  $\nu_{NO}$  band is lower than that of the monometallic precursor  $Ru(bpb)(NO)Cl$  ( $\nu_{NO} = 1867\text{ cm}^{-1}$ ), and is reflective of the replacement of the chloride ligand by the oxo-bridge in the product. A similar lowering of  $\nu_{NO}$  is observed in the related  $Ru(salen)(NO)Cl$  ( $1844\text{ cm}^{-1}$ ) and  $[Ru(salen)(NO)]_2(\mu-O)$  ( $1762\text{ cm}^{-1}$ ) derivatives in  $CH_2Cl_2$ .<sup>10</sup> A strong band at  $816\text{ cm}^{-1}$  is also evident in the IR spectrum, and is assigned to the IR-active asymmetric Ru-O-Ru stretch. Related stretches have been reported for  $[Fe(salen)]_2(\mu-O).py$  ( $805\text{ cm}^{-1}$ ),<sup>23</sup>  $[Fe(sal-O-phen)]_2(\mu-O).py$  ( $820\text{ cm}^{-1}$ ),<sup>23</sup> and  $[Ru(salen)]_2(\mu-O)$  ( $805\text{ cm}^{-1}$ ).<sup>10</sup>

**2.3.2 X-ray crystallography of  $[(bpb)Ru(NO)]_2(\mu-O)$ .** There are only a handful of oxo-bridged compounds of ruthenium containing the  $(O_x)N-Ru-O-Ru-N(O_x)$  fragment that have been structurally characterized in the solid state by X-ray crystallography (Table 2.2). Slow diffusion of  $CH_2Cl_2$  vapor into a DMF solution of  $[Ru(bpb)(NO)]_2(\mu-O)$  at room temperature over several days produced single crystals suitable for X-ray diffraction. The molecular structure of this oxo-bridged dimer is shown in Figure 2.1, and selected structural data are presented in Table 2.3. Details of the bond lengths and angles are presented in Tables 2.4 and 2.5 in the appendix at the end of this dissertation.

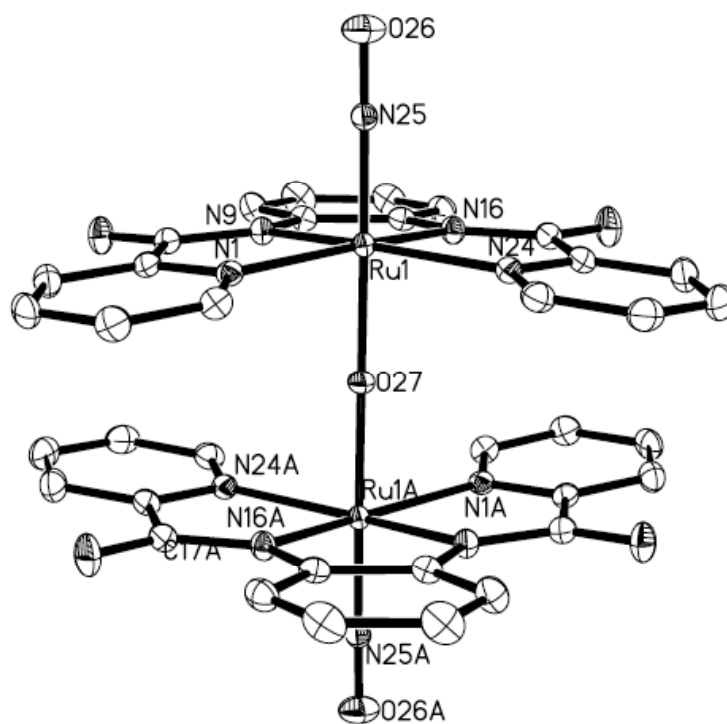


**Figure 2.1.** Molecular structure of  $[Ru(bpb)(NO)]_2(\mu-O)$ . Thermal ellipsoids are shown at 50%. Hydrogen atoms and the methylene chloride solvent molecules are omitted for clarity

**Table 2.2.** Selected Vibrational Frequencies (cm<sup>-1</sup>) and Geometric Parameters (Å, °) for oxo-bridged Ruthenium Compounds.<sup>a</sup>

Compound	$\nu_{\text{NO}}$	$\nu_{\text{RuORu}}$	Ru-O	Ru-N(O)	Ru-O-Ru	Ru-N-O	O-Ru-N(O)	Ref
[Ru(bpb)(NO)] <sub>2</sub> ( $\mu$ -O)	1758	816	1.8829(3)	1.7486(17)	180.0	175.85(15)	174.14(5)	Tw
[RuCl <sub>2</sub> (NO)(dmpH) <sub>2</sub> ] <sub>2</sub> ( $\mu$ -O)	1809.1	791.7	1.917(6)	1.734(9)	178.9(4)	178.5(10)	179.6(4)	[24]
			1.885(6)	1.721(10)		177.1(13)	179.0(4)	
[RuCl(dmpH)( $\mu$ <sub>2</sub> -dmp)(NO)] <sub>2</sub> ( $\mu$ -O)	1829.4, 1802.4	715.5	1.910(3)	1.747(4)	116.35(13)	177.7(5)	178.1(2)	[24]
			1.913(3)	1.752(4)	)	179.6(4)	178.2(2)	
[RuCl <sub>4</sub> (NO)][Ru(dmpH) <sub>4</sub> (NO)]( $\mu$ -O)	1818.2, 1790.2	792.2	1.940(2)	1.731(3)	176.6(2)	176.2(3)	177.67(14)	[24]
			1.873(2)	1.759(3)		177.0(3)	179.27(14)	
{[Ru(bpy) <sub>2</sub> (NO <sub>2</sub> )] <sub>2</sub> ( $\mu$ -O)} <sup>2+</sup>			1.876(6)		157.2(3)			[25]
			1.890(7)					

<sup>a</sup> Abbreviations: dmpH = 3,5-dimethylpyrazole; bpy = bipyridine, tw = this work.

**Table 2.3.** Selected Bond Lengths and Angles for [Ru(bpb)(NO)]<sub>2</sub>(μ-O)

<b>Bond Lengths (Å)</b>			
N(25)-O(26)	1.174(2)	Ru(1)-N(16)	1.9935(15)
Ru(1)-N(25)	1.7486(17)	Ru(1)-N(24)	2.1507(16)
Ru(1)-N(1)	2.1277(15)	Ru(1)-O(27)	1.8829(3)
Ru(1)-N(9)	1.9890(16)		
<b>Bond Angles (°)</b>			
O(26)-N(25)-Ru(1)	175.85(15)	N(16)-Ru(1)-O(27)	89.49(5)
N(25)-Ru(1)-O(27)	174.14(5)	N(24)-Ru(1)-O(27)	86.41(4)
N(25)-Ru(1)-N(1)	91.61(7)	N(1)-Ru(1)-N(9)	80.14(6)
N(25)-Ru(1)-N(9)	95.07(7)	N(1)-Ru(1)-N(16)	162.84(6)
N(25)-Ru(1)-N(16)	95.54(7)	N(1)-Ru(1)-N(24)	115.53(6)
N(25)-Ru(1)-N(24)	91.52(7)	N(9)-Ru(1)-N(24)	162.86(6)
N(1)-Ru(1)-O(27)	84.36(4)	N(9)-Ru(1)-N(16)	83.69(6)
N(9)-Ru(1)-O(27)	88.44(5)		

Each ruthenium center is octahedrally coordinated, and the oxo group is at an inversion center. The Ru-N-O moiety is near-linear with a bond angle of 175.85(15)°, and a Ru-N(O) bond length of 1.7486(17) Å. The Ru-N(pyridyl) bonds are longer than the Ru-N(amide) bonds (Figure 2.1 and Table 2.3) with an average Ru-N(bpb) value of 2.06 Å. The ON-Ru-O-Ru-NO linkage is linear and imposed by symmetry, with a Ru-O bond length of 1.8829(3) Å; this Ru-O bond length is similar to those determined for related Ru oxo-bridged dimers (Table 2.2).<sup>24,25</sup>

**2.3.3 Redox behavior of Ru(bpb)(NO)Cl and [Ru(bpb)(NO)]<sub>2</sub>(μ-O).** The redox behavior of the known compound Ru(bpb)(NO)Cl and the newly-synthesized oxo-bridged compound [Ru(bpb)(NO)]<sub>2</sub>(μ-O) in DMF have been investigated using cyclic voltammetry. These compounds are insoluble or only sparingly soluble in other organic solvents, hence we were limited with our choice of solvent for electrochemistry. The electrochemistry of Ru(bpb)(NO)Cl is characterized by two reversible one-electron reductions at  $E^{o'}_1 = -0.17$  V and  $E^{o'}_2 = -0.64$  V vs Ag/AgCl (Figure 2.2), and these are represented by equations (2.1) and (2.2), respectively.

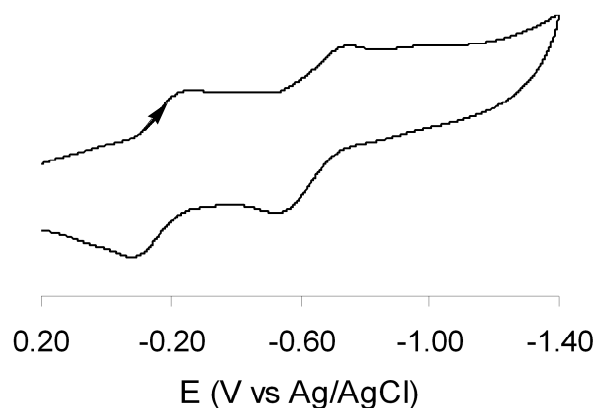
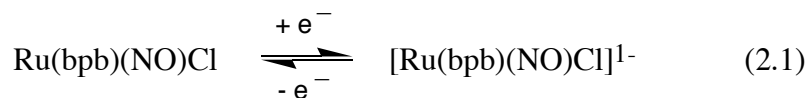


**Fig. 2.2.** Cyclic voltammogram of 0.1 mM Ru(bpb)(NO)Cl in DMF containing 0.1 M NBu<sub>4</sub>PF<sub>6</sub>. Scan rate = 0.2 V/s.





No oxidation behavior for Ru(bpb)(NO)Cl was apparent in this solvent.

The oxo-bridged compound [Ru(bpb)(NO)]<sub>2</sub>(μ-O) displays a quasi-reversible and diffusion-controlled reduction in DMF, and the cyclic voltammogram showing this reduction ( $E^{\circ'} = -0.99$  V vs Ag/AgCl) is shown in Figure 2.3.

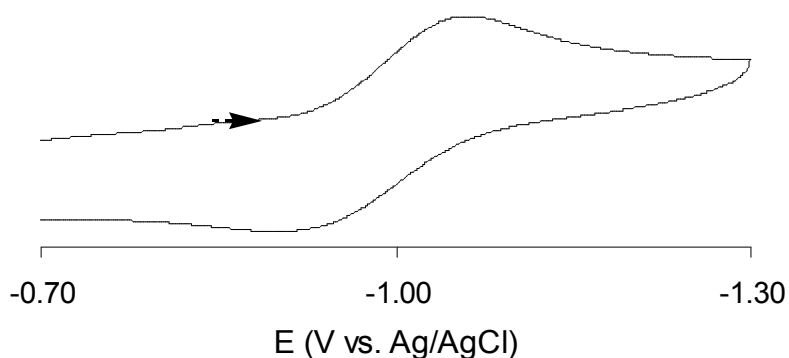
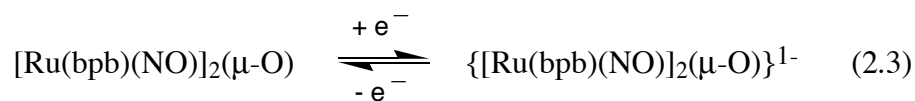
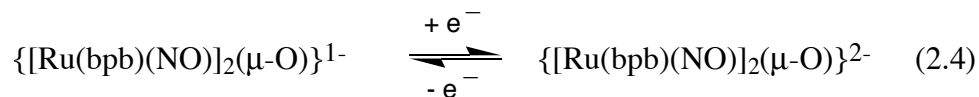


**Fig. 2.3.** Cyclic voltammogram of 0.1 mM [Ru(bpb)(NO)]<sub>2</sub>O in DMF containing 0.1 M NBu<sub>4</sub>PF<sub>6</sub>. Scan rate = 0.2 V/s.

The peak separation ( $\Delta E = E_{\text{pa}} - E_{\text{pc}}$ ) is 132 mV. We thus represent this first reduction by equation (2.3).



The compound also undergoes a second, but irreversible, reduction at  $E_p^2 = -1.63$  V (not shown). Analysis of the peak geometry indicates that the overall process consists of a reversible electron transfer followed by a fast chemical (decomposition) reaction, i.e., equations (2.4) and (2.5).



Interestingly, a similar pattern of reductions has been reported for the oxo-bridged ruthenium complexes  $\{\text{[RuX(bpy)}_2\}_2(\mu\text{-O})\}^{2+}$  ( $X = \text{Cl}$  or  $\text{NO}_2$ ) in acetonitrile vs. SCE ( $E^o = -0.32$  V and  $-0.15$  V, respectively;  $E_{p2} = -1.0$  V and  $-0.75$  V, respectively).<sup>26</sup> As seen in Figures 2.2 and 2.3, the large negative shifts of the reductions of  $\text{[Ru(bpb)(NO)]}_2(\mu\text{-O})$  ( $\nu_{\text{NO}} = 1758 \text{ cm}^{-1}$ ) compared with those of the precursor compound  $\text{Ru(bpb)(NO)Cl}$  ( $\nu_{\text{NO}} = 1867 \text{ cm}^{-1}$ ), by  $\sim 0.8\text{-}1.0$  V, are consistent with the greater electron density in the oxo-bridged compound.

## 2.4 Conclusion

In this chapter we reported the preparation of the oxo-bridged dimer  $\text{[Ru(bpb)(NO)]}_2(\mu\text{-O})$  in 60% isolated yield from the reaction of the known

Ru(bpb)(NO)Cl with silver nitrite. The compound exhibits a  $\nu_{\text{NO}}$  of 1758  $\text{cm}^{-1}$  (KBr pellet). The crystal structure reveals a linear ON-Ru-O-Ru-NO fragment with the oxo atom serving as an inversion center in the molecule. The redox behavior in DMF is characterized by a reversible reduction followed by a second but irreversible reduction in this solvent.

## 2.5 References

- (1) Richter-Addo, G. B.; Legzdins, P. *Metal Nitrosyls*; Oxford University Press: New York, 1992.
- (2) Richter-Addo, G. B.; Legzdins, P.; Burstyn, J. *Chem. Rev.* **2002**, *102*, 857-859, and references therein.
- (3) Cheng, L.; Richter-Addo, G. B. In *The Porphyrin Handbook*; Guilard, R., Smith, K., Kadish, K. M., Eds.; Academic Press: New York, 2000; Vol. 4 (Biochemistry and Binding: Activation of Small Molecules), p 219-291.
- (4) Cheng, L.; Chen, L.; Chung, H.-S.; Khan, M. A.; Richter-Addo, G. B.; Young, V. G., Jr. *Organometallics* **1998**, *17*, 3853-3864, Table 3, and references therein.
- (5) Li, M.; Shang, M.; Duval, H. F.; Scheidt, W. R. *Acta Crystallogr.* **2000**, *C56*, 1206-1207.
- (6) Scheidt, W. R. In *The Porphyrin Handbook*; Kadish, K. M., Smith, K. M., Guilard, R., Eds.; Academic Press: New York, 2000, p Chapter 16.
- (7) Cheng, L.; Lee, J.; Powell, D. R.; Richter-Addo, G. B. *Acta Crystallogr.* **2004**, *E60*, m1340-m1342.
- (8) Patra, A. K.; Rose, M. J.; Murphy, K. A.; Olmstead, M. M.; Mascharak, P. K. *Inorg. Chem.* **2004**, *43*, 4487-4495.
- (9) Patra, A. K.; Rose, M. J.; Olmstead, M. M.; Mascharak, P. K. *J. Am. Chem. Soc.* **2004**, *126*, 4780-4781.
- (10) Works, C. F.; Jocher, C. J.; Bart, G. D.; Bu, X.; Ford, P. C. *Inorg. Chem.* **2002**, *41*, 3728-3739.
- (11) Ford, P. C.; Bourassa, J.; Miranda, K.; Lee, B.; Lorkovic, I.; Boggs, S.; Kudo, S.; Laverman, L. *Coord. Chem. Rev.* **1998**, *171*, 185-202.
- (12) Afshar, R. K.; Patra, A. K.; Olmstead, M. M.; Mascharak, P. K. *Inorg. Chem.* **2004**, *43*, 5736-5743.
- (13) Patra, A. K.; Afshar, R.; Olmstead, M. M.; Mascharak, P. K. *Angew. Chem. Int. Ed.* **2002**, *41*, 2512-2515.
- (14) Patra, A. K.; Mascharak, P. K. *Inorg. Chem.* **2003**, *42*, 7363-7365.
- (15) Patra, A. K.; Rowland, J. M.; Marlin, D. S.; Bill, E.; Olmstead, M. M.; Mascharak, P. K. *Inorg. Chem.* **2003**, *42*, 6812-6823.

- (16) Barnes, D. J.; Chapman, R. L.; Vagg, R. S.; Watton, E. C. *J. Chem. Eng. Data* **1978**, *23*, 349-350.
- (17) Bruker AXS: Madison, WI, 1997-1998.
- (18) Bruker AXS: Madison, WI, 1998.
- (19) Sheldrick, G. M.; University of Göttingen, Germany: University of Göttingen, Germany, 2000.
- (20) Sheldrick, G. M. 2000. SADABS: Program for Empirical Absorption Correction of Area Detector Data.
- (21) Bohle, D. S.; Hung, C.-H.; Smith, B. D. *Inorg. Chem.* **1998**, *37*, 5798-5806.
- (22) Ankers, D. L.; Fanning, J. C. *Polyhedron* **2001**, *20*, 623-625.
- (23) Niswander, R. H.; Martell, A. E. *Inorg. Chem.* **1978**, *17*, 2341-2344.
- (24) Bohle, D. S.; Sagan, E. S. *Eur. J. Inorg. Chem.* **2000**, 1609-1616.
- (25) Phelps, D. W.; Kahn, E. M.; Hodgson, D. J. *Inorg. Chem.* **1975**, *14*, 2486-2490.
- (26) Weaver, T. R.; Meyer, T. J.; Adeyemi, S. A.; Brown, G. M.; Eckberg, R. P.; Hatfield, W. E.; Johnson, E. C.; Murray, R. W.; Untereker, D. *J. Am. Chem. Soc.* **1975**, *97*, 3039-3048.
- (27) Dutta, S. K.; Beckmann, U.; Bill, E.; Weyhermiiller, T.; Wieghardt, K. *Inorg. Chem.* **2000**, *39*, 3355-3364.
- (28) Leung, W.-H.; Ma, J.-X.; Yam, V. W.-W.; Che, C.-M.; Poon, C.-K. *J. Chem. Soc. Dalton Trans.* **1991**, 1071-1076.
- (29) Callahan, R. W.; Meyer, T. J. *Inorg. Chem.* **1977**, *16*, 574-81.
- (30) Callahan, R. W.; Brown, G. M.; Meyer, T. J. *J. Am. Chem. Soc.* **1975**, *97*, 894-895.

## Chapter 3. Synthesis, Molecular Structures, and Fiber-optic Infrared Spectroelectrochemical Studies of Six-Coordinate Manganese Nitrosyl Porphyrins\*

### 3.1 Introduction

As mentioned in Chapter 1, the biological role of nitric oxide (NO) is tied in with its interactions with iron center in heme-containing biomolecules.<sup>1</sup> For example, the receptor for NO in smooth muscles is the heme-containing enzyme soluble guanylyl cyclase (sGC), and this enzyme contains histidine as an axial ligand to iron. NO binds to the ferrous heme site in sGC to give a six-coordinate (por)Fe(NO)(His) complex that converts rapidly to a five-coordinate (por)Fe(NO) species.<sup>2-5</sup> The binding of NO to the heme iron in sGC has been correlated with activation of this enzyme, resulting in the formation of cyclic guanosine monophosphate (cGMP) from guanosine triphosphate (GTP). The accumulation of cGMP is associated with vasodilation. Other histidine-liganded hemes also form adducts with NO, and these include hemoglobin (Hb), myoglobin (Mb), cytochrome oxidase, nitrophorins, FixL, and nitrite reductase.<sup>1</sup> In many cases, the binding of NO has been shown to be biologically relevant.

---

\* Taken in part from;

i- "Synthesis, Characterization, and Molecular Structures of Six-Coordinate Manganese Nitrosyl Porphyrins" Zahran Z. N.; Lee J.; Alguindigue S. S.; Khan M. A.; Richter-Addo G. B. *Dalton Trans.* **2004**, 44–50, with permission from Elsevier.

ii- "Fiber-optic Infrared Spectroelectrochemical Studies of Six-coordinate Manganese Nitrosyl Porphyrins in Nonaqueous Media" Zahran Z. N.; Shaw M.; Khan M. A.; Richter-Addo G. B. *Inorg. Chem.* **2006**, *45*, 2661-2668, with permission from The American Chemical Society.

iii- "Specific detection of gaseous NO and <sup>15</sup>NO in headspace from liquid-phase reactions involving NO-generating organic, inorganic, and biochemical samples using a mid-infrared laser" Yi J.; Namjou K.; Zahran Z. N.; McCann P. J.; Richter-Addo G. B. *Nitric Oxide* **2006**, *15*, 154-162, with permission from Elsevier.

NO binds to both ferric and ferrous hemes, although NO binding to ferric hemes is weaker than that for ferrous hemes.<sup>6</sup> The biological relevance of NO binding to ferric heme is best exemplified by ferric nitrophorins from the kissing bug *Rhodnius prolixus*.<sup>7</sup> The nitrophorins are ferric heme proteins contained in the saliva of the insect, and the hemes bind NO. When the insect bites the host, NO is released from the ferric nitrosyl nitrophorins, resulting in local vasodilation which ensures that the insect obtains a sufficient blood meal.

Efforts to study well-characterized six-coordinate ferric nitrosyl porphyrins have been hampered by the fact that they are difficult to obtain pure, and only a few have been obtained in sufficient quantities for detailed spectroscopic and crystallographic studies.<sup>8</sup> Such ferric nitrosyl porphyrins belong to the {MNO}<sup>6</sup> class as defined by Enemark and Feltham.<sup>9-11</sup>

We are interested in the study of manganese nitrosyl porphyrins belonging to the {MnNO}<sup>6</sup> classification. These are isoelectronic with their ferric nitrosyl and d<sup>6</sup> ferrous carbonyl FeCO counterparts. NO binding to manganese-substituted heme provides a possible scenario in which the strong Mn-NO bond formed between NO and Mn<sup>II</sup> will effectively mimic the labile Fe-NO bond formed between NO and ferric Fe<sup>III</sup> ion (which is isoelectronic with Mn<sup>II</sup>). Manganese-substituted hemoproteins containing NO continue to provide very valuable information to complement that obtained from their isoelectronic and biologically relevant FeCO analogues. Examples of such Mn-substituted nitrosyl complexes include those of Hb, Mb, sGC, neuronal nitric oxide synthase (nNOS), cytochrome *c*, and peroxidases.<sup>4,12-15</sup> MnHbNO and MnMbNO have been prepared as spectroscopic models for their EPR-

silent Fe-CO analogues.<sup>16-18</sup> The MnHbNO derivative was shown to behave similarly to native HbCO in terms of ligand rebinding kinetics and cooperativity.<sup>19</sup> In the case of Mn-substituted sGC, binding of NO generated a six-coordinate (porphyrinato)Mn(NO)(His) species that did not activate the enzyme.<sup>4</sup> Other manganese hemes have been prepared for NO-sensing<sup>20-22</sup> and for peroxynitrite decomposition.<sup>23,24</sup>

Prior to our work in this area, there were only two X-ray crystal structures of manganese nitrosyl porphyrins, namely those of (TTP)Mn(NO) and (TPP)Mn(NO)(4-Mepip).<sup>25</sup> In order to better understand the nature of binding of NO to manganese porphyrins and to determine the nature of the *trans* effect of the bound NO ligand in these complexes, we prepared a new set of synthetic manganese nitrosyl porphyrin complexes containing methanol, and *N*-donor ligands. In this chapter, we report their syntheses and structural characterization by spectroscopy and high resolution X-ray crystallography.

We were also interested in examining the redox properties of the six-coordinate (por)Mn(NO)(1-MeIm) compounds containing the axial imidazole group. To the best of our knowledge, only one other electrochemical study of MnNO porphyrins was reported prior to our work, that of the five-coordinate (TPP)Mn(NO).<sup>26</sup> The electrochemistry of non-NO-containing manganese porphyrins is well developed.<sup>27-29</sup> In this chapter, we also report the redox behavior of three (por)Mn(NO)(1-MeIm) (por = TPP, TTP, T(*p*-OCH<sub>3</sub>)PP) compounds in CH<sub>2</sub>Cl<sub>2</sub> and THF as determined by cyclic voltammetry, infrared spectroelectrochemistry, and bulk electrolysis.

A structural representation of the new complexes is given in Figure 3.1.

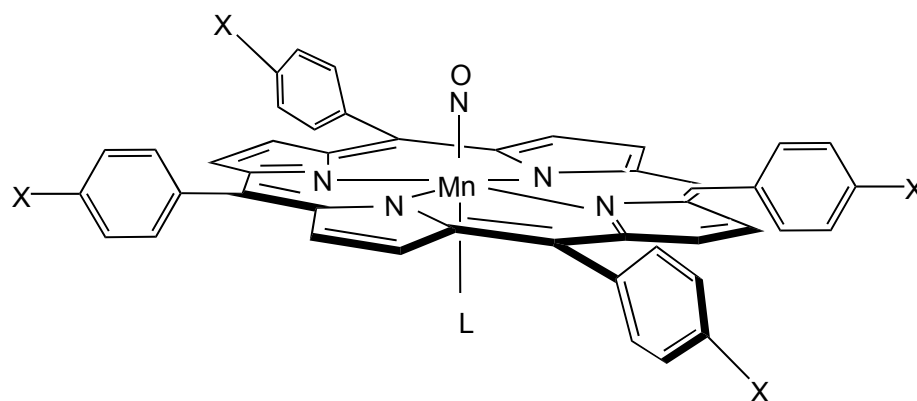


**Figure 3.1.** Structural representation of the new (por)Mn(NO)(L) complexes  
X = H, L = 1-Methylimidazole or piperidine  
X = CH<sub>3</sub>, L = 1-Methylimidazole, piperidine, or MeOH  
X = OCH<sub>3</sub>, L = 1-Methylimidazole or piperidine

### 3.2 Experimental Section

All reactions were performed under an atmosphere of prepurified nitrogen using standard Schlenk glassware and/or in an Innovative Technology Labmaster 100 Dry Box. Solutions for spectral studies were also prepared under a nitrogen atmosphere. The toluene, CH<sub>2</sub>Cl<sub>2</sub>, and THF solvents were distilled from calcium hydride under nitrogen gas just prior to use.

**3.2.1 Chemicals.** H<sub>2</sub>TPP (TPP = 5,10,15,20-tetraphenylporphyrinato dianion), H<sub>2</sub>TTP (TTP = 5,10,15,20-tetra-*p*-tolylporphyrinato dianion), H<sub>2</sub>(T(*p*-OCH<sub>3</sub>)PP (T(*p*-OCH<sub>3</sub>)PP = 5,10,15,20-tetra-*p*-methoxyphenylporphyrinato dianion), (TPP)MnCl, (TTP)MnCl, (T(*p*-OCH<sub>3</sub>)PP)MnCl, and (TPP)Mn(1-MeIm) were prepared by literature methods.<sup>30,31</sup> Pyrrole (98%), benzaldehyde (99%), *p*-tolylaldehyde (97%), *p*-anisaldehyde (98%), piperidine (99.5+%), 1-methylimidazole

(1-MeIm, 99+%), anhydrous CH<sub>3</sub>OH (99.8%) and tetra-*n*-butylammonium hexafluorophosphate (NBu<sub>4</sub>PF<sub>6</sub>) were purchased from Aldrich Chemical Company and used as received. Chloroform-*d* (99.8%) was obtained from Cambridge Isotope Laboratories. Nitric oxide (98%, Matheson Gas) for the synthesis work was passed through KOH pellets and two cold traps (dry ice/acetone, -78 °C) to remove higher nitrogen oxides. Nitrogen of ultrahigh-purity grade was purchased from Trigas (Houston, TX).

**3.2.2 Instrumentation.** Infrared spectra were recorded on a Bio-Rad FT-155 FTIR spectrometer. Proton NMR spectra were obtained on Varian VXR-S 500 MHz or Varian Mercury VX 300 MHz spectrometers for low temperature and room temperature measurements, respectively, and the signals referenced to the residual signal of the solvent employed (CHCl<sub>3</sub> at 7.24 ppm). All coupling constants are in Hz. ESI mass spectra were obtained on a Micromass Q-TOF mass spectrometer. Elemental analyses were performed by Atlantic Microlab, Norcross, Georgia.

Electrochemical measurements were performed with a BAS CV-50W instrument. IR spectra were recorded with a Bruker Vector 22 FTIR spectrometer equipped with a mid-IR fiber-optic dip probe system and a liquid-nitrogen cooled MCT detector (RemSpec corporation, Sturbridge, MA, USA). The stainless steel mirror of the fiber-optic dip probe system was replaced by a Pt disc (3 mm diameter) working electrode (Bioanalytical Systems). The spectrometer was set to 4 cm<sup>-1</sup> resolution. Typically 16 scans from 2200–1000 cm<sup>-1</sup> were recorded.

The IR spectroelectrochemical measurements were performed in a three-electrode cell as described previously (Pt working and auxiliary electrodes, Ag wire

quasi-reference electrode).<sup>32</sup> The room temperature was  $23 \pm 1$  °C. We jacketed the cell to allow for a dry ice-acetone bath ( $-78$ °C) for the low temperature measurements. Potentials are reported versus the ferrocene-ferrocenium couple ( $\sim +0.46$  V vs. SCE).<sup>33</sup> Corrections for iR drop between the working and reference electrodes were applied. The solutions used were 0.5–1.0 mM in analyte in 10 mL of 0.1 M  $\text{NBu}_4\text{PF}_6$ . Nitrogen gas was bubbled through the solution for about 8 min before each set of measurements and was passed continuously over the surface of the solution during the measurements. Each measurement was performed in triplicate or greater.

Nitric oxide detection was based on high-resolution tunable diode laser absorption spectroscopy (TDLAS). The experimental setup is shown in Fig. 3.2. The system consists of a cold head, optics and control electronics. The cold head, inside the cryostat housing, contains an infrared photovoltaic detector, a foil heater, a temperature sensor, and a mid- infrared tunable diode laser source emitting in the wavelength region around  $5.2 \mu\text{m}$ . The optics consist of a gas cell and a series of plane and focusing mirrors for steering and collimating the infrared beam. Associated electronics include a laser current controller, a laser temperature controller, a lock-in amplifier, two waveform generators, and a computer. The present system employs a closed-cycle refrigerator system that cools the diode laser and detector to cryogenic temperatures with no need for liquid nitrogen refills. An auto-tuning temperature controller (LakeShore, OH), working in conjunction with cryo-cooler (IGC Polycold, CA), is used to maintain laser temperatures at set points between 85 and 110 K. The spectrometer takes advantage of a second harmonic detection scheme, and a 100-m

long optical multi-pass Herriott cell (Aerodyne, MA).

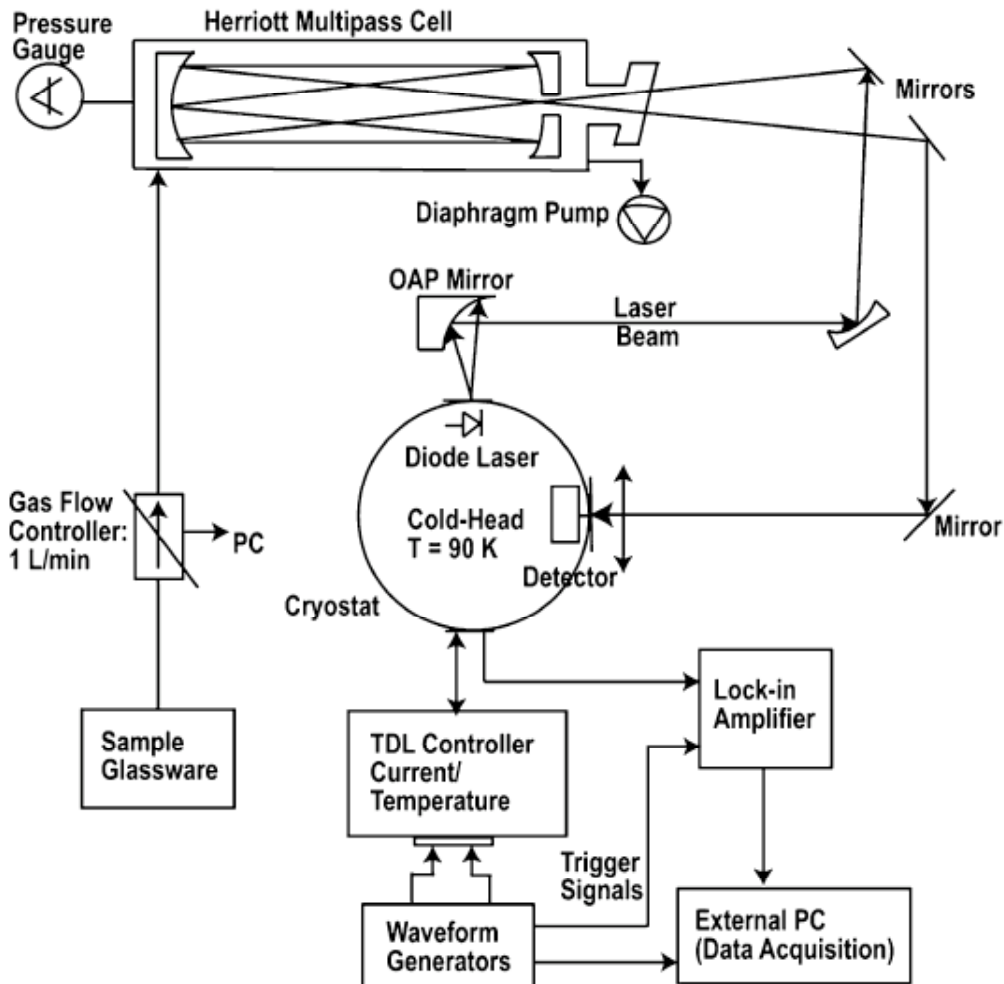


**Figure 3.2.** Schematic diagram of the TDLAS instrument. Major components include a cryostat, Herriott multipass cell, electronics, and an integrated gas sampling interface.

**3.2.3 Preparation of (*por*)Mn(NO)(*pip*) compounds (*por* = TPP, TTP, T(*p*-OCH<sub>3</sub>)PP).** A Schlenk flask was charged with (TTP)MnCl (0.035 g, 0.046 mmol), CH<sub>2</sub>Cl<sub>2</sub> (8 mL), and piperidine (0.7 mL). The mixture was stirred to generate a green solution, and NO gas was bubbled through the solution for 20 min. [Note: during

this time, an uncharacterized white gas was generated from solution] The color of the reaction mixture turned bright red. Nitrogen was bubbled through the solution for 5 min to remove any unreacted NO and other gaseous products. Anhydrous methanol (15 mL) was added to the solution, and the volume of the solution was reduced in vacuo until a solid precipitated. The supernatant solution was discarded, and the red-purple solid was dried in vacuo to give (TTP)Mn(NO)(pip).0.65CH<sub>2</sub>Cl<sub>2</sub> (0.026 g, 0.029 mmol, 63% isolated yield). Anal. Calcd for C<sub>53</sub>H<sub>47</sub>N<sub>6</sub>O<sub>1</sub>Mn<sub>1</sub>.0.65CH<sub>2</sub>Cl<sub>2</sub>: C, 72.07; H, 5.44; N, 9.40; Cl, 5.15. Found: C, 71.78; H, 5.66; N, 9.53; Cl, 4.99. IR (KBr, cm<sup>-1</sup>):  $\nu_{\text{NO}} = 1746$  s; also 3022 w, 2935 w, 2920 w, 2859 w, 1533 m, 1503 m, 1450 m, 1404 vw, 1346 m, 1305 w, 1268 vw, 1209 w, 1181 m, 1108 w, 1070 m, 1027 vw, 1015 w, 1001 s, 871 w, 847 vw, 796 s, 718 m, 631 w, 552 vw, 522 m. <sup>1</sup>H NMR (CDCl<sub>3</sub>;  $\delta$ , ppm, -50 °C): 8.74 (s, 8H, *pyrrole*-H of TTP), 8.03 (d,  $J = 7$ , 4H, *o*-H of TTP), 7.99 (d,  $J = 7$ , 4H, *o'*-H of TTP), 7.52 (app t (overlapping d's), 8H, *m/m'*-H of TTP), 5.29 (s, CH<sub>2</sub>Cl<sub>2</sub>), 2.67 (s, 12H, CH<sub>3</sub> of TTP), 0.15 (br d, 1H of pip), -0.40 (br d, 2H of pip), -0.78 (br d, 1H of pip), -1.34 (br d, 2H of pip), -3.42 (app q,  $J = 13$ , 2H of pip), -3.76 (br d, 2H of pip), -5.48 (app t,  $J = 13$ , 1H of pip). The peaks of piperidine ligand were not observed in the <sup>1</sup>H NMR spectrum of the complex at room temperature. ESI mass spectrum:  $m/z$  723 [(TTP)Mn]<sup>+</sup> (100%).

Attempts to obtain suitable crystals of this sample for a single-crystal X-ray structural determination have not been successful. Unexpectedly, however, crystals grown by slow solvent evaporation of a CH<sub>2</sub>Cl<sub>2</sub>/CH<sub>3</sub>OH (2:1) solution mixture of (TTP)Mn(NO)(pip) under inert atmosphere were identified as (TTP)Mn(NO)(CH<sub>3</sub>OH) by X-ray crystallography. The IR spectrum of

(TTP)Mn(NO)(CH<sub>3</sub>OH) (as a KBr pellet) showed a strong band at 1743 cm<sup>-1</sup> assigned to  $\nu_{\text{NO}}$ .

The (TPP)Mn(NO)(pip) and (T(*p*-OCH<sub>3</sub>)PP)Mn(NO)(pip) compounds were prepared similarly from the reaction of (TPP)MnCl and (T(*p*-OCH<sub>3</sub>)PP)MnCl, respectively, with NO gas in the presence of piperidine. The red (TPP)Mn(NO)(pip) product was obtained in 85 % isolated yield. IR (KBr, cm<sup>-1</sup>):  $\nu_{\text{NO}}$  = 1744 s; also 3447 w, 2938 w, 1598 m, 1534 vw, 1490 vw, 1441 m, 1347 m, 1303 vw, 1273 w, 1205 w, 1175 vw, 1071 m, 1003 vs, 870 vw, 797 m, 752 s, 702 s, 667 w. <sup>1</sup>H NMR (CDCl<sub>3</sub>;  $\delta$ , ppm): 8.71 (s, 8H, pyrrole-H of TPP), 8.16 (d, *J* = 7 Hz, 4H, *o*-H of TPP), 8.06 (d, *J* = 8 Hz, 4H, *o'*-H of TPP), 7.69–7.64 (overlapping m, *m*-H and *p*-H of TPP). The peaks of piperidine ligand were not observed in the <sup>1</sup>H NMR spectrum of the complex at room temperature. ESI mass spectrum: *m/z* 667.1 [(TPP)Mn]<sup>+</sup> (100%).

The red-purple (T(*p*-OCH<sub>3</sub>)PP)Mn(NO)(pip) product was obtained in 81% isolated yield. IR (KBr, cm<sup>-1</sup>):  $\nu_{\text{NO}}$  = 1748 s; also 3032 vw, 2997 vw, 2935 w, 2834 w, 1608 m, 1574 vw, 1533 m, 1512 s, 1502 s, 1464 m, 1439 m, 1410 vw, 1347 m, 1303 w, 1287 m, 1248 s, 1206 w, 1175 s, 1107 w, 1071 w, 1039 w, 1026 m, 1002 s, 872 vw, 848 w, 803 s, 719 m, 637 vw, 632 vw, 607 m, 575 vw, 555 w, 538 m. <sup>1</sup>H NMR (CDCl<sub>3</sub>;  $\delta$ , ppm, -50 °C): 8.73 (s, 8H, *pyrrole*-H of T(*p*-OCH<sub>3</sub>)PP), 8.04 (d, *J* = 8, 4H, *o*-H of T(*p*-OCH<sub>3</sub>)PP), 8.01 (d, *J* = 8, 4H, *o'*-H of T(*p*-OCH<sub>3</sub>)PP), 7.22 (br (overlapping with CHCl<sub>3</sub> peak), 8H, *m/m'*-H of T(*p*-OCH<sub>3</sub>)PP), 5.29 (s, CH<sub>2</sub>Cl<sub>2</sub>), 4.07 (s, 12H, OCH<sub>3</sub> of T(*p*-OCH<sub>3</sub>)PP), 0.12 (br d, 1H of pip), -0.43 (br d, 2H of pip), -0.80 (br d, 1H of pip), -1.36 (br d, 2H of pip), -3.46 (app q, *J* = 13, 2H of pip), -3.79 (br d, 2H of pip), -5.50 (app t, *J* = 13, 1H of pip). The peaks of piperidine ligand

were not observed in the  $^1\text{H}$  NMR spectrum of the complex at room temperature. ESI mass spectrum:  $m/z$  787 [(T(*p*-OCH<sub>3</sub>)PP)Mn]<sup>+</sup> (100%).

**3.2.4 Preparation of (*por*)Mn(NO)(1-MeIm) compounds (*por* = TPP, TTP, T(*p*-CH<sub>3</sub>)PP).** To a stirred CH<sub>2</sub>Cl<sub>2</sub> solution (8 mL) of (TTP)Mn(NO)(pip).0.65CH<sub>2</sub>Cl<sub>2</sub> (0.020 g, 0.022 mmol) was added 1-MeIm (0.01 mL). The mixture was stirred for 5 h. The solvent was removed in vacuo, and the residue was redissolved in a CH<sub>2</sub>Cl<sub>2</sub>/CH<sub>3</sub>OH (1:1, 10 mL) mixture. To this solution was added 1-MeIm (0.1 mL). Slow evaporation of this solution at room temperature under inert atmosphere gave spectroscopically pure (TTP)Mn(NO)(1-MeIm) (0.012 g, 0.014 mmol, 64% isolated yield) as purple crystals. IR (KBr, cm<sup>-1</sup>):  $\nu_{\text{NO}}$  = 1738 s, 1732 s; also 3128 vw, 3019 vw, 2952 vw, 2918 vw, 2866 vw, 1532 w, 1506 m, 1457 vw, 1347 m, 1304 vw, 1284 vw, 1233 w, 1209 w, 1181 m, 1108 m, 1081 w, 1071 m, 1001 s, 943 vw, 908 vw, 846 vw, 796 s, 731 w, 719 m, 670 vw, 660 vw, 628 vw, 615 vw, 523 m.  $^1\text{H}$  NMR (CDCl<sub>3</sub>;  $\delta$ , ppm): 8.69 (s, 8H, *pyrrole*-H of TTP), 8.07 (d,  $J = 7$ , 4H, *o*-H of TTP), 7.90 (d,  $J = 7$ , 4H, *o'*-H of TTP), 7.50 (d,  $J = 7$ , 4H, *m*-H of TTP), 7.44 (d,  $J = 7$ , 4H, *m'*-H of TTP), 2.67 (s, 12H, CH<sub>3</sub> of TTP). The peaks of the 1-MeIm ligand were not observed at room temperature.  $^1\text{H}$  NMR (CDCl<sub>3</sub>;  $\delta$ , ppm, -40 °C): 8.69 (s, 8H, *pyrrole*-H of TTP), 8.04 (d,  $J = 7$ , 4H, *o*-H of TTP), 7.91 (d,  $J = 7$ , 4H, *o'*-H of TTP), 7.50 (d,  $J = 7$ , 4H, *m*-H of TTP), 7.45 (d,  $J = 7$ , 4H, *m'*-H of TTP), 4.60 (s, 1H of 1-MeIm), 2.66 (s, 12H, CH<sub>3</sub> of TTP), 2.06 (s, 3H, CH<sub>3</sub> of 1-MeIm), 1.17 (s, 1H of 1-MeIm), 0.73 (s, 1H of 1-MeIm). ESI mass spectrum:  $m/z$  805 [(TTP)Mn(1-MeIm)]<sup>+</sup> (57%), 723 [(TTP)Mn]<sup>+</sup> (100%).

The red (TPP)Mn(NO)(1-MeIm) compound was prepared in 80% isolated yield by similar procedures. IR (KBr,  $\text{cm}^{-1}$ ):  $\nu_{\text{NO}} = 1737\text{s}$ ; also 3122vw, 3030vw, 2994vw, 2952vw, 2930vw, 2900vw, 2865vw, 1686vw, 1655vw, 1637vw, 1596w, 1533w, 1489vw, 1440w, 1420vw, 1365vw, 1348s, 1284vw, 1231w, 1204w, 1176w, 1070s, 1003s, 796s, 752s, 703s, 663w, 614vw, 526vw, 453vw.  $^1\text{H}$  NMR ( $\text{CDCl}_3$ ;  $\delta$ , ppm): 8.67 (s, 8H, pyrrole-H of TPP), 8.20 (d,  $J = 7$  Hz, 4H, *o*-H of TPP), 8.01 (d,  $J = 8$  Hz, 4H, *o'*-H of TPP), 7.68–7.64 (overlapping m, *m*-H and *p*-H of TPP). The peaks of the 1-MeIm ligand were not observed in the spectrum at room temperature. ESI mass spectrum:  $m/z$  667.2 [(TPP)Mn] $^+$  (68.8%), 749.2 [(TPP)Mn(1-MeIm)] $^+$  (100%). The (por)Mn(NO)(1-MeIm) complexes are stable in the solid state in air for at least 1 week (as judged by IR and  $^1\text{H}$  NMR spectroscopy). Suitable crystals for X-ray crystallography were grown by slow evaporation of a  $\text{CH}_2\text{Cl}_2$ /toluene (2:1) solution of the compound containing 1-MeIm at room temperature under inert atmosphere.

The purple (T(*p*-OCH<sub>3</sub>)PP)Mn(NO)(1-MeIm) compound was obtained in 77% isolated yield after recrystallization from  $\text{CH}_2\text{Cl}_2$ /CH<sub>3</sub>OH (2:1) in the presence of excess 1-MeIm at room temperature under inert atmosphere. IR (KBr,  $\text{cm}^{-1}$ ):  $\nu_{\text{NO}} = 1736$  s; also 3128 vw, 3033 vw, 2998 vw, 2958 vw, 2934 vw, 2906 vw, 2833 vw, 1606 m, 1533 w, 1501 s, 1466 w, 1460 w, 1439 w, 1346 m, 1303 vw, 1285 m, 1247 s, 1205 vw, 1177 s, 1108 w, 1089 vw, 1073 vw, 1037 vw, 1024 w, 1001 s, 849 vw, 808 m, 799 m, 735 w, 719 w, 670 vw, 662 vw, 607 w, 582 vw, 540 w.  $^1\text{H}$  NMR ( $\text{CDCl}_3$ ;  $\delta$ , ppm): 8.69 (s, 8H, pyrrole-H of T(*p*-OCH<sub>3</sub>)PP), 8.08 (dd,  $J = 8.4/2.1$ , 4H, *o*-H of T(*p*-OCH<sub>3</sub>)PP), 7.91 (dd,  $J = 8.4/2.1$ , 4H, *o'*-H of T(*p*-OCH<sub>3</sub>)PP), 7.22 (dd

(overlapping with  $\text{CHCl}_3$  peak), 4H, *m*-H of T(*p*-OCH<sub>3</sub>)PP), 7.17 (dd,  $J = 8.4/2.1$ , 4H, *m*'-H of T(*p*-OCH<sub>3</sub>)PP), 4.06 (s, 12H, OCH<sub>3</sub> of T(*p*-OCH<sub>3</sub>)PP). The peaks of the 1-MeIm ligand were not observed at room temperature. <sup>1</sup>H NMR (CDCl<sub>3</sub>;  $\delta$ , ppm, -40 °C): 8.70 (s, 8H, *pyrrole*-H of T(*p*-OCH<sub>3</sub>)PP), 8.07 (dd,  $J = 8/2$ , 4H, *o*-H of T(*p*-OCH<sub>3</sub>)PP), 7.93 (dd,  $J = 8/2$ , 4H, *o*'-H of T(*p*-OCH<sub>3</sub>)PP), 7.22 (dd (overlapping with  $\text{CHCl}_3$  peak), 4H, *m*-H of T(*p*-OCH<sub>3</sub>)PP), 7.18 (dd,  $J = 8/2$ , 4H, *m*'-H of T(*p*-OCH<sub>3</sub>)PP), 4.60 (s, 1H of 1-MeIm), 4.06 (s, 12H, OCH<sub>3</sub> of T(*p*-OCH<sub>3</sub>)PP), 2.07 (s, 3H, CH<sub>3</sub> of 1-MeIm), 1.15 (s, 1H of 1-MeIm), 0.72 (s, 1H of 1-MeIm). ESI mass spectrum:  $m/z$  787 [(T(*p*-OCH<sub>3</sub>)PP)Mn]<sup>+</sup> (100%).

**3.2.5 Structural determinations by X-ray crystallography.** X-ray data were collected on a Bruker Apex diffractometer using MoK $\alpha$  ( $\lambda = 0.71073 \text{ \AA}$ ) radiation. The structures were solved by the direct method using the SHELXTL system (Version 6.12; 1997) and refined by full-matrix least squares on  $F^2$  using all reflections. All the non-hydrogen atoms were refined anisotropically. All the hydrogen atoms were included with idealized parameters.

(i) **(TTP)Mn(NO)(CH<sub>3</sub>OH).** Crystals for X-ray crystallography were grown during an attempt at crystallizing (TTP)Mn(NO)(pip) using CH<sub>2</sub>Cl<sub>2</sub>/CH<sub>3</sub>OH. X-ray diffraction intensity data, which approximately covered the full sphere of the reciprocal space, were measured as a series of  $\omega$  oscillation frames each 0.3° for 21 sec/frame. The detector was operated in 512 x 512 mode and was positioned 6.00 cm from the crystal. Coverage of unique data was 99.0% complete to 54°(2 $\theta$ ). Cell parameters were determined from a non-linear least squares fit of 7582 reflections in the range of 2.8 <  $\theta$  < 25.9°. A total of 37158 reflections were measured. The data

were corrected for absorption by multi-scan method from equivalent reflections giving minimum and maximum transmissions of 0.9193 and 0.9403. The asymmetric unit contains one and half units of the  $C_{49}H_{40}N_5O_2Mn$  complex (with the Mn(2) atom situated very near the inversion center) and fractional amounts of dichloromethane (0.2) and methanol (1.15) solvent molecules. SHELXTL restraints of DFIX and ISOR were applied to the atoms belonging to the disordered axial group and the solvent molecules to achieve convergence during least squares refinement. The final  $R1 = 0.067$  is based on 12836 “observed reflections” [ $I > 2\sigma(I)$ ], and  $wR2 = 0.178$  is based on all reflections (13303 reflections).

(ii) *(TTP)Mn(NO)(1-MeIm).0.28CH<sub>2</sub>Cl<sub>2</sub>*. Suitable crystals for X-ray crystallography were grown by slow evaporation of CH<sub>2</sub>Cl<sub>2</sub>/CH<sub>3</sub>OH (1:1) solution of the compound containing 1-MeIm at room temperature under inert atmosphere. Coverage of unique data was 99.1% complete to 53°(2 $\theta$ ). Cell parameters were determined from a non-linear least squares fit of 8729 reflections in the range of  $3.6 < \theta < 26.2^\circ$ . A total of 13983 reflections were measured. The data were corrected for absorption by multi-scan method from equivalent reflections giving minimum and maximum transmissions of 0.8602 and 0.9036. The asymmetric unit contains one and half units of the  $C_{52}H_{42}N_7OMn$  complex (with the Mn(2) atom situated very near the inversion center) and fractional dichloromethane solvent molecules. The unit of the  $C_{52}H_{42}N_7OMn$  complex that lies at the inversion center is disordered at the axial sites. The N(10) atom from the NO group lies very close to the N(11) atom of the 1-methylimidazole ligand. As a result, the refinement of the positional and thermal parameters is compromised. The Mn-N-O angles and N-O bond distances in the two

molecules are significantly different. However, in view of the axial disorder in the disordered molecule, it is not possible to ascertain whether these differences in bond angles and bond lengths are real or an artifact of the poor refinement due to the disorder. SHELXTL restraints of DFIX, ISOR and EADP were applied to achieve convergence during least squares refinement (the disordered NO group in the molecule #2 was allowed to refine without any restraints). The final R1 = 0.078 is based on 13129 “observed reflections” [ $I > 2\sigma(I)$ ], and wR2 = 0.222 is based on all reflections (13983 reflections).

*(iii) (TPP)Mn(NO)(1-MeIm).2.5toluene.* Suitable crystals for X-ray crystallography were grown by slow evaporation of a CH<sub>2</sub>Cl<sub>2</sub>/toluene (2:1) solution of the compound containing 1-MeIm at room temperature under inert atmosphere. X-ray data were collected at 120(2) K. Intensity data, which approximately covered the full sphere of the reciprocal space, were measured as a series of  $\omega$  oscillation frames each 0.3° for 21 sec/frame. The detector was operated in 512 x 512 mode and was positioned 6.12 cm from the crystal. Coverage of unique data was 94.5 % complete to 53.0°(2 $\theta$ ). Cell parameters were determined from a non-linear least squares fit of 6715 reflections in the range of  $2.5 < \theta < 28.2^\circ$ . A total of 30030 reflections were measured. All the non-hydrogen atoms were refined anisotropically. All the hydrogen atoms were included with idealized parameters. The asymmetric unit contains one C<sub>48</sub>H<sub>34</sub>MnN<sub>7</sub>O molecule and 2.5 toluene solvent molecules which sit on the crystallographic two-fold axis. The final R1 = 0.0448 is based on 10214 “observed reflections” [ $I > 2\sigma(I)$ ].

(iv) *(T(p-OCH<sub>3</sub>)PP)Mn(NO)(1-MeIm).CH<sub>2</sub>Cl<sub>2</sub>*. Suitable crystals for X-ray crystallography were grown by slow evaporation of CH<sub>2</sub>Cl<sub>2</sub>/CH<sub>3</sub>OH (2:1) solution of the compound containing 1-MeIm at room temperature under inert atmosphere. Coverage of unique data was 98.4% complete to 50°(2 $\theta$ ). Cell parameters were determined from a non-linear least squares fit of 7823 reflections in the range of 3.2 <  $\theta$  < 24.4°. A total of 23420 reflections were measured. The data were corrected for absorption by multi-scan method from equivalent reflections giving minimum and maximum transmissions of 0.9223 and 0.9820. An initial data set was collected at 100(2) K and yielded poor refinement. Better data were obtained at 178(2) K, showing much sharper spots on the frames. There is a highly disordered CH<sub>2</sub>Cl<sub>2</sub> solvent molecule and some minor disorder involving the nitrosyl O(1) atom, the imidazole N(7) atom, and the C(27), C(34), C(41) and C(48) atoms of the porphyrin periphery. The non-solvent atoms were refined without resolving into their disordered components due to the very close proximity of these components. The overall geometry of the molecule of interest is sound. SHELXTL restraints of DFIX, ISOR and SADI were applied to the atoms belonging to the disordered solvent molecule to achieve convergence during least squares refinement. The final R1 = 0.075 is based on 4461 “observed reflections” [ $I > 2\sigma(I)$ ], and wR2 = 0.1896 is based on all reflections (8054 unique reflections). The data fit well for a triclinic cell ( $R_{\text{int}} = 0.07$ ); the Laue symmetry is 1-bar.

Displacement ellipsoids in Figures 3.3-3.6 are drawn at the 35% probability level. Details of the crystal data and refinement are given in Table 3.1. Some selected bond lengths and angles are given in Table 3.2. Details of bond lengths and angles for

**Table 3.1** Crystal Data and Structure Refinement of (TTP)Mn(NO)(CH<sub>3</sub>OH) (**1**), (TTP)Mn(NO)(1-MeIm).0.28CH<sub>2</sub>Cl<sub>2</sub> (**2**), (TPP)Mn(NO)(1-MeIm).2.5toluene (**3**), and (T(*p*-OCH<sub>3</sub>)PP)Mn(NO)(1-MeIm).CH<sub>2</sub>Cl<sub>2</sub> (**4**).

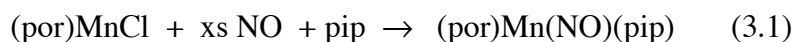
Compound	1	2	3	4
Formula	C <sub>49.90</sub> H <sub>43.33</sub> Cl <sub>0.27</sub> N <sub>5</sub> O <sub>2.77</sub> Mn	C <sub>52.28</sub> H <sub>42.56</sub> Cl <sub>0.56</sub> NO Mn	C <sub>65.50</sub> H <sub>53.50</sub> N <sub>7</sub> O Mn	C <sub>53</sub> H <sub>44</sub> Cl <sub>2</sub> N <sub>7</sub> O <sub>5</sub> Mn
Fw	821.69	859.65	1009.59	984.79
<i>T</i> (K)	96(2)	120(2)	120(2)	178(2)
Crystal system	Triclinic	Triclinic	Triclinic	Triclinic
Space group	P $\bar{1}$	P $\bar{1}$	P $\bar{1}$	P $\bar{1}$
<i>a</i> (Å), $\alpha$ (°)	11.3170(6), 97.9110(10)	14.9067(8), 104.7090(10)	9.8071(7), 105.277(1)	12.1992(16), 90.136(2)
<i>b</i> (Å), $\beta$ (°)	12.3768(7), 102.9260(10)	15.0365(8), 90.8320(10)	13.0989(9), 97.316(1)	12.7458(17), 90.287(2)
<i>c</i> (Å), $\gamma$ (°)	23.0336(12), 97.0580(10)	15.8656(9), 97.3400(10)	21.4652(15), 98.166(1)	15.151(2), 99.228(2)
<i>V</i> , <i>Z</i>	3074.9(3) Å <sup>3</sup> , 3	3407.4(3) Å <sup>3</sup> , 3	2593.6(3) Å <sup>3</sup> , 2	2325.3(5) Å <sup>3</sup> , 2
<i>D</i> (calcd), g/cm <sup>3</sup>	1.331	1.257	1.293	1.407
Abs coeff, mm <sup>-1</sup>	0.389	0.370	0.307	0.457
F(000)	1288	1343	1057	1020
Crystal size (mm)	0.22 x 0.18 x 0.16	0.42 x 0.38 x 0.28	0.28 x 0.12 x 0.04	0.18 x 0.04 x 0.04
$\theta$ range for data collection (°)	1.68–27.00	1.84–26.50	1.66–28.26°	1.62–25.00
Index ranges	-14 ≤ <i>h</i> ≤ 14, -15 ≤ <i>k</i> ≤ 15, -29 ≤ <i>l</i> ≤ 29	-18 ≤ <i>h</i> ≤ 18, -18 ≤ <i>k</i> ≤ 18, -19 ≤ <i>l</i> ≤ 19	-13 ≤ <i>h</i> ≤ 12, -17 ≤ <i>k</i> ≤ 17, -28 ≤ <i>l</i> ≤ 27	-14 ≤ <i>h</i> ≤ 14, -14 ≤ <i>k</i> ≤ 15, -17 ≤ <i>l</i> ≤ 17
Reflns. collected	37158	36783	30030	23420
Independent reflns	13303 [R <sub>int</sub> = 0.0162]	13983 [R <sub>int</sub> = 0.0198]	12135 [R <sub>int</sub> = 0.0195]	8054 [R <sub>int</sub> = 0.0715]
Max and min transmission	0.9403 and 0.9193	0.9036 and 0.8602	0.9878 and 0.9191	0.9820 and 0.9223
Data/restraints/parameters	13303 / 124 / 916	13983 / 69 / 948	12135 / 0 / 680	8054 / 63 / 672
Good-of-fit on F <sup>2</sup>	1.127	1.193	1.053	1.004
Final R indices [I > 2σ(I)] <sup>a,b</sup>	R1 = 0.0670, wR2 = 0.1769	R1 = 0.0780, wR2 = 0.2205	R1 = 0.0448, wR2 = 0.1202	R1 = 0.0750, wR2 = 0.1721
R indices (all data) <sup>a,b</sup>	R1 = 0.0685, wR2 = 0.1778	R1 = 0.0811, wR2 = 0.2220	R1 = 0.0550, wR2 = 0.1303	R1 = 0.1437, wR2 = 0.1896
Largest diff. peak and hole, eÅ <sup>-3</sup>	1.311 and -0.776	1.257 and -0.592	1.099 and -0.426	1.190 and -0.458

$$^a R1 = \sum ||F_o| - |F_c|| / \sum |F_o|. \quad ^b wR2 = \{ \sum [w(F_o^2 - F_c^2)^2] / \sum [wF_o^4] \}^{1/2}$$

the four compounds are presented in Tables 3.6-3.13 in the appendix at the end of this dissertation.

### 3.3 Results and Discussion

**3.3.1 Synthesis and spectroscopic characterization.** The synthesis and chemistry of manganese- and other metalloporphyrin nitrosyl complexes has been reviewed.<sup>1</sup> Scheidt and coworkers showed, over thirty years ago, that reductive nitrosylation of manganese (III) porphyrins took place in the presence of aliphatic amines to generate manganese nitrosyl porphyrins.<sup>34,35</sup> We have used similar methodology for the preparation of (TTP)Mn(NO)(pip), (TPP)Mn(NO)(pip), and (T(*p*-OCH<sub>3</sub>)PP)Mn(NO)(pip) in 65%, 85%, and 81% isolated yields, respectively (eq. 3.1).

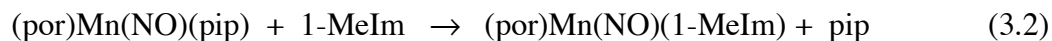


(por = TTP, TPP, or T(*p*-OCH<sub>3</sub>)PP; pip = piperidine)

These red-purple complexes are soluble in CH<sub>2</sub>Cl<sub>2</sub>, CHCl<sub>3</sub>, and acetone, but are only slightly soluble in hexane and methanol. The complexes are moderately stable in air in the solid state, showing no noticeable signs of decomposition over a one month period as judged by IR and <sup>1</sup>H NMR spectroscopy. Their solutions, however, are air-sensitive.

The IR spectra of the (por)Mn(NO)(pip) complexes (as KBr pellets) show new strong bands at 1746 cm<sup>-1</sup> (for TTP), 1744 cm<sup>-1</sup> (for TPP), and 1748 cm<sup>-1</sup> (for (T(*p*-OCH<sub>3</sub>)PP), respectively, which are attributed to the terminal NO ligands. These bands are similar to that reported for the crystallographically characterized (TPP)Mn(NO)(4-Mepip) compound ( $\nu_{\text{NO}}$  1740 cm<sup>-1</sup>) that exhibits a linear NO geometry.<sup>34,35</sup> Although the (por)Mn(NO)(pip) compounds are isoelectronic with their ferric-NO counterparts, the  $\nu_{\text{NO}}$ s of the manganese compounds are significantly lower than those of the isolable ferric [(por)Fe(NO)(*N*-base)]<sup>+</sup> complexes ( $\nu_{\text{NO}}$  1894-1921 cm<sup>-1</sup>) reported by Scheidt and Ellison.<sup>36</sup> Parthasarathi and Spiro have suggested, based on resonance Raman studies, that there is reduced metal→NO backbonding in Fe<sup>III</sup>-NO compared with Mn<sup>II</sup>-NO due to the higher effective charge on iron in Fe<sup>III</sup>-NO.<sup>16</sup> Clearly, such an effect is responsible for the differences in the observed NO stretching frequencies between the Mn and Fe compounds. We have not been able to observe the parent ions of the (por)Mn(NO)(pip) compounds in their ESI mass spectra; the spectra show ion fragments due to loss of both axial ligands. Attempts to grow crystals of the (TTP)Mn(NO)(pip) complex from dichloromethane/methanol resulted in the replacement of the piperidine ligand with methanol solvent to give (TTP)Mn(NO)(CH<sub>3</sub>OH) ( $\nu_{\text{NO}}$  1743 cm<sup>-1</sup>), as determined from the X-ray crystal structure of the crystallization product (see later).

The (TTP)Mn(NO)(1-MeIm), (TPP)Mn(NO)(1-MeIm) and (T(*p*-OCH<sub>3</sub>)PP)Mn(NO)(1-MeIm) derivatives were prepared in 62%, 80%, and 77% isolated yields, respectively, from the reaction of their piperidine precursors with an excess of 1-MeIm in CH<sub>2</sub>Cl<sub>2</sub> (eq. 3.2).



Prior to this work, the  $(\text{por})\text{Mn}(\text{NO})(\text{imidazole})$  compounds reported in the literature were prepared *in situ* from exposure of NO to solutions of  $\text{Mn}^{\text{II}}$ -porphyrins containing an excess of the imidazole ligand, and the success of this synthetic procedure was very limited.<sup>16,37</sup> We find that the preparative route described by eq. 3.2 provides a convenient method by which pure samples of the nitrosyl products can be obtained in sizeable quantities.

These products of eq. 3.2 are purple and have similar solubilities and stabilities as those of their piperidine precursors. The IR spectra of the  $(\text{por})\text{Mn}(\text{NO})(1\text{-MeIm})$  complexes (as KBr pellets) reveal bands at 1738/1732  $\text{cm}^{-1}$  (split band), 1737, and 1736  $\text{cm}^{-1}$  for the TTP, TPP, and T(*p*-OCH<sub>3</sub>)PP derivatives, respectively, assignable to  $\nu_{\text{NO}}$ . The split  $\nu_{\text{NO}}$  band of  $(\text{TTP})\text{Mn}(\text{NO})(1\text{-MeIm})$  is likely due to the presence of two orientations of the 1-MeIm ligand in the bulk solid. In any event, the  $\nu_{\text{NO}}$ s in  $(\text{por})\text{Mn}(\text{NO})(1\text{-MeIm})$  are  $\sim 12 \text{ cm}^{-1}$  lower in energy than the  $\nu_{\text{NO}}$ s of the precursor  $(\text{por})\text{Mn}(\text{NO})(\text{pip})$  complexes. This feature is consistent with the replacement of piperidine ligand with the  $\pi$ -interacting 1-MeIm ligand, which makes more electron density available for  $\text{Mn}^{\text{II}} \rightarrow \text{NO}$  backdonation, resulting in the lowering of  $\nu_{\text{NO}}$ .

The low temperature <sup>1</sup>H NMR spectra of the  $(\text{por})\text{Mn}(\text{NO})(1\text{-MeIm})$  complexes show, in addition to the peaks due to the porphyrin rings, the peaks of the bound 1-MeIm ligands. The ESI mass spectrum of  $(\text{TTP})\text{Mn}(\text{NO})(1\text{-MeIm})$  and

(TPP)Mn(NO)(1-MeIm) show ion fragments assigned to loss of the NO ligand or loss of both axial ligands, whereas that of (T(*p*-OCH<sub>3</sub>)PP)Mn(NO)(1-MeIm) shows ions fragments from loss of both axial ligands.

**3.3.2 X-ray Crystallographic Characterization.** We were successful in obtaining suitable crystals of (TTP)Mn(NO)(CH<sub>3</sub>OH), (TTP)Mn(NO)(1-MeIm), (TPP)Mn(NO)(1-MeIm), and (T(*p*-OCH<sub>3</sub>)PP)Mn(NO)(1-MeIm) for single-crystal X-ray crystallography. The molecular structures of the four compounds are shown in Figures 3.3-3.6. Selected structural parameters for all four compounds are reported in Table 3.2. As stated in the Experimental Section, the asymmetric units in the crystals of (TTP)Mn(NO)(CH<sub>3</sub>OH) and (TTP)Mn(NO)(1-MeIm) contain one crystallographically ordered molecule and a second disordered molecule. Only the more accurate data from the ordered components are discussed here.

The Mn-N-O moieties in all four complexes are linear, and this observed linearity is consistent with the classification of these (por)Mn(NO)(L) compounds as {MnNO}<sup>6</sup> species.<sup>9-11</sup> The axial Mn-N(O) bond length in (TTP)Mn(NO)(CH<sub>3</sub>OH) is 1.680(2) Å, and the N-O bond length is 1.165(2) Å. The Mn-N(por) distances fall in the 2.008(2)-2.032(2) Å range, and the Mn atom is displaced by 0.12 Å from the 24-atom mean porphyrin plane toward the  $\pi$ -acid NO ligand. The methanol ligand in (TTP)Mn(NO)(CH<sub>3</sub>OH) is oriented essentially between two porphyrin N-atoms (Fig. 3.3b). The Mn-O bond length is 2.086(2) Å and the Mn-O2-C49 angle is 124°. The Mn-O bond length is shorter than those observed in other structurally characterized Mn<sup>II</sup> and Mn<sup>III</sup> porphyrins containing alcohol ligands: [(TPP)Mn(CH<sub>3</sub>OH)<sub>2</sub>]ClO<sub>4</sub> (2.252(2) and 2.270 (2) Å),<sup>38</sup> [(TPP)Mn(CH<sub>3</sub>OH)<sub>2</sub>]SbCl<sub>6</sub> (2.283(5) Å),<sup>39</sup>

(TPP)Mn(N<sub>3</sub>)(CH<sub>3</sub>OH) (2.329(7) Å),<sup>40</sup> (P\*)Mn(CH<sub>3</sub>OH)(OH) (2.251(7) Å; P\* = D<sub>4</sub> symmetrical chiral porphyrin),<sup>41</sup> (TCPP)Mn(CH<sub>3</sub>OH)(H<sub>2</sub>O) (2.246 Å; TCPP = tetracarboxyphenylporphyrin),<sup>42</sup> and [(OEP)Mn(EtOH)]ClO<sub>4</sub> (2.145(2) Å).<sup>43</sup>

The axial Mn-N(O) bond lengths in the three (por)Mn(NO)(1-MeIm) complexes are 1.650(2)-1.645(3) Å and are similar to that observed previously in (TPP)Mn(NO)(4-Mepip) (1.644(5) Å)<sup>25,34</sup> but are *shorter* than that determined for (TTP)Mn(NO)(CH<sub>3</sub>OH) (1.680(2) Å). This feature is suggestive of greater Mn→NO π-backdonation in these (por)Mn(NO)(N-base) compounds. The lower  $\nu_{\text{NO}}$  of the 1-methylimidazole complexes compared with that of the methanol complex supports this view of a greater Mn→NO π-backdonation in (por)Mn(NO)(1-MeIm).

Importantly, the axial *trans* Mn-N(imidazole) bond lengths of 2.096(2), 2.0882(13), and 2.097(3) Å for the (TTP)Mn(NO)(1-MeIm), (TPP)Mn(NO)(1-MeIm), and (T(*p*-OCH<sub>3</sub>)Mn(NO)(1-MeIm) compounds, respectively, are *shorter* than that reported for the five-coordinate high-spin (TPP)Mn(1-MeIm) complex (2.192(2) Å)<sup>44</sup> reflecting the influence of the strong field π-acid NO ligand on these *trans* Mn-N(imidazole) bond lengths. A comparison of the structural data of the (por)Mn(NO)(1-MeIm) compounds with those of the previously reported and *isoelectronic* [(OEP)Fe(NO)(1-MeIm)]<sup>+</sup> shows that in both classes of compounds, the metal-NO groups are linear. Furthermore, the Mn-N(O) bond lengths (1.645(3)-1.650(2) Å) are similar to that in [(OEP)Fe(NO)(1-MeIm)]<sup>+</sup> (1.6465(17) Å)<sup>36</sup> although the N-O bond lengths in (por)Mn(NO)(1-MeIm) (1.174(3)-1.176(4) Å) are slightly longer than that observed in [(OEP)Fe(NO)(1-MeIm)]<sup>+</sup> (1.135(2) Å).

**Table 3.2** Selected Bond Lengths in (Å) and Angles in (°) of (TTP)Mn(NO)(CH<sub>3</sub>OH) (**1**), (TTP)Mn(NO)(1-MeIm) (**2**), (TPP)Mn(NO)(1-MeIm) (**3**), and (T(*p*-OCH<sub>3</sub>)PP)Mn(NO)(1-MeIm) (**4**).

Compound	<b>1</b>	<b>2</b>	<b>3</b>	<b>4</b>
Mn-N(NO) (Å)	1.680(2)	1.650(2)	1.6411(13)	1.645(3)
Mn-X <sup>a</sup> (Å)	2.086(2)	2.096(2)	2.0882(13)	2.097(3)
Mn-N(por) (Å)	2.001(1)- 2.032(2)	2.023(2)- 2.029(2)	2.019(1)- 2.080(12)	2.015(3)- 2.097(3)
N-O (Å)	1.165(2)	1.174(3)	1.1718(17)	1.176(4)
Mn-N-O (°)	175.66(18)	176.6(2)	178.42(12)	178.3(3)
X-Mn-N(NO) (°)	177.36(7)	176.76(11)	178.30(5)	179.31(13)

<sup>a</sup> X = oxygen atom in compound (**1**) and nitrogen atom in all other compounds

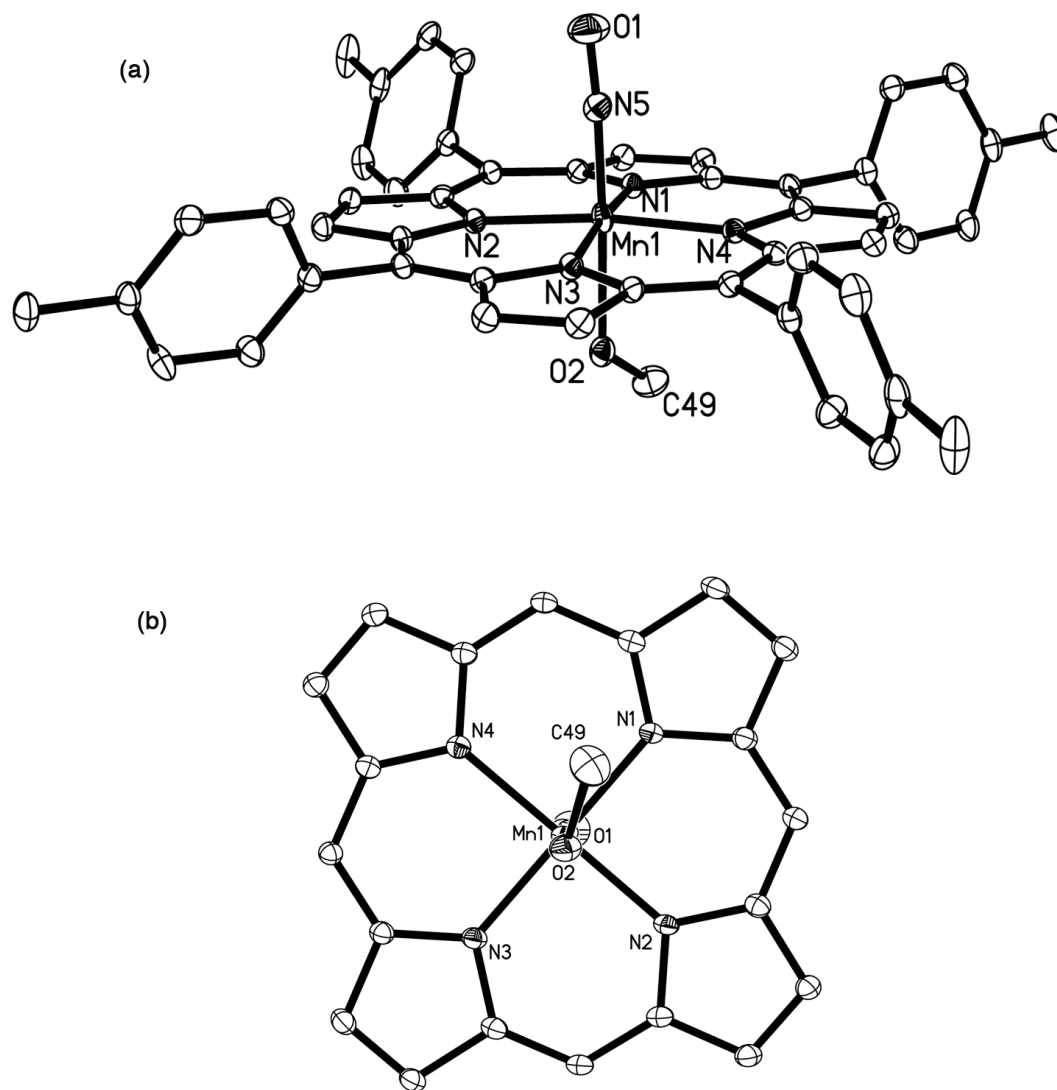


**Figure 3.3.** (a) Molecular structure of  $(\text{TTP})\text{Mn}(\text{NO})(\text{CH}_3\text{OH})$ . Only the crystallographically ordered molecule is shown. (b) View of the orientation of the methanol ligand relative to the porphyrin skeleton. The porphyrin tolyl substituents have been omitted for clarity.

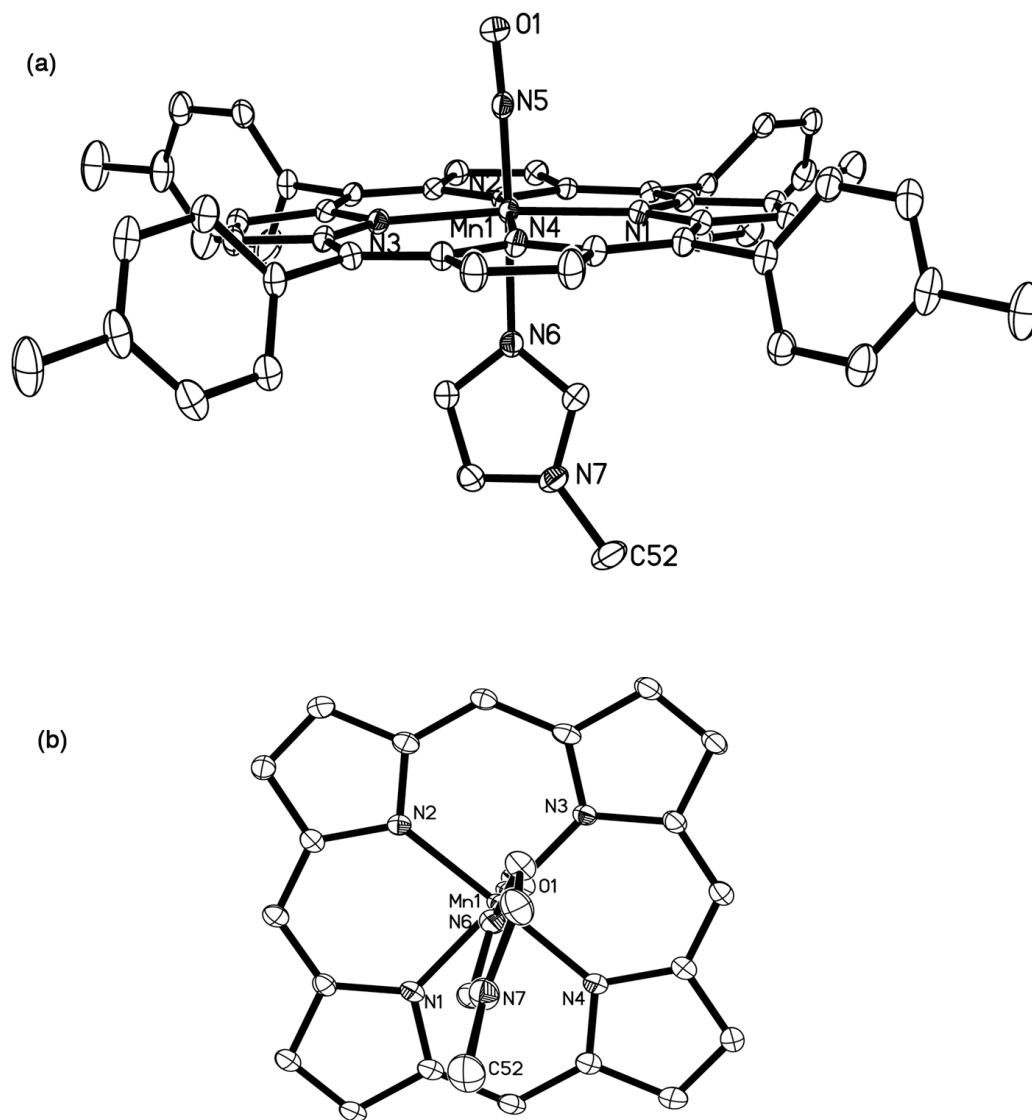


**Figure 3.4.** (a) Molecular structure of (TTP)Mn(NO)(1-MeIm). Hydrogen atoms have been omitted for clarity. Only the crystallographically ordered molecule is shown. (b) View of the orientation of the 1-MeIm ligand relative to the porphyrin skeleton. The porphyrin tolyl substituents have been omitted for clarity.

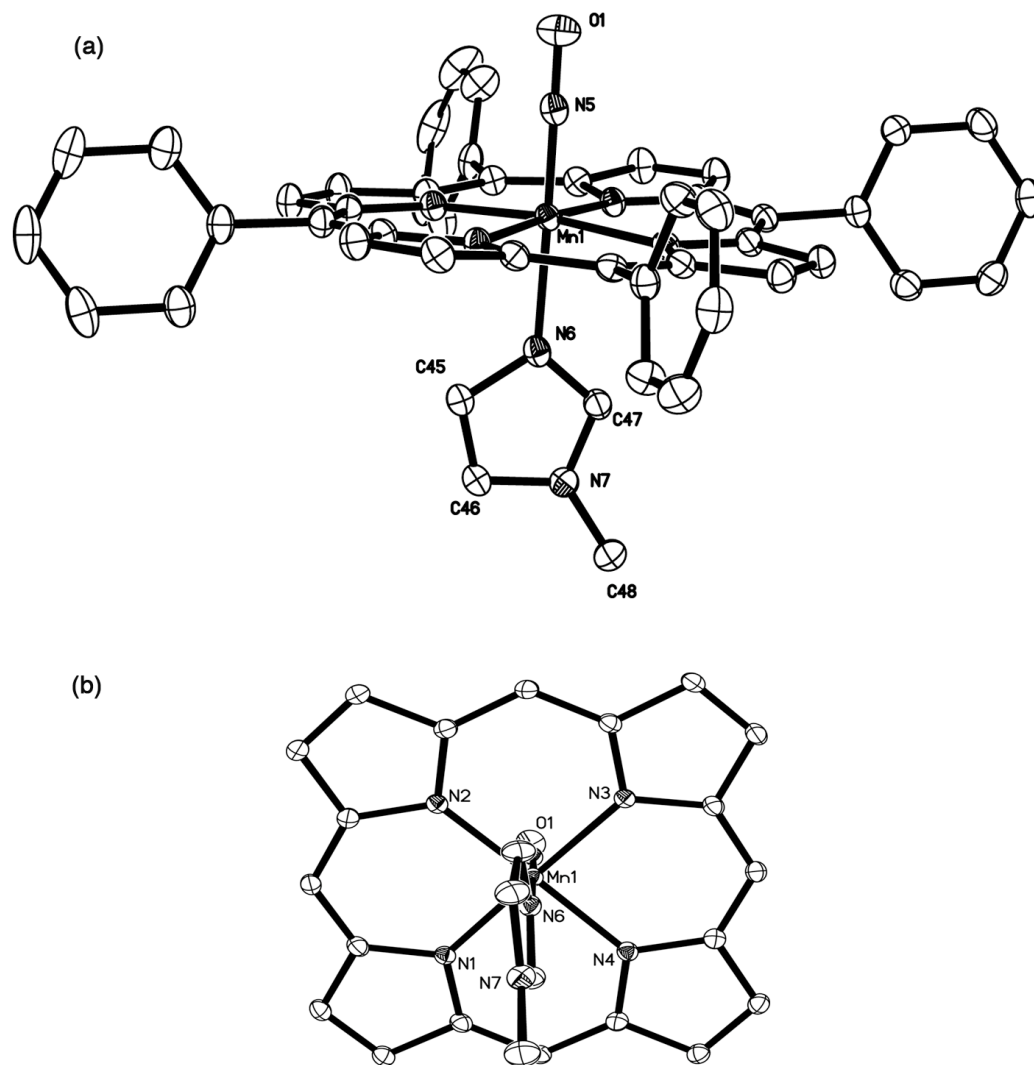


**Figure 3.5.** (a) Molecular structure of (TPP)Mn(NO)(1-MeIm). Hydrogen atoms have been omitted for clarity. (b) View of the orientation of the 1-MeIm ligand relative to the porphyrin skeleton. The porphyrin *p*-phenyl substituents have been omitted for clarity.

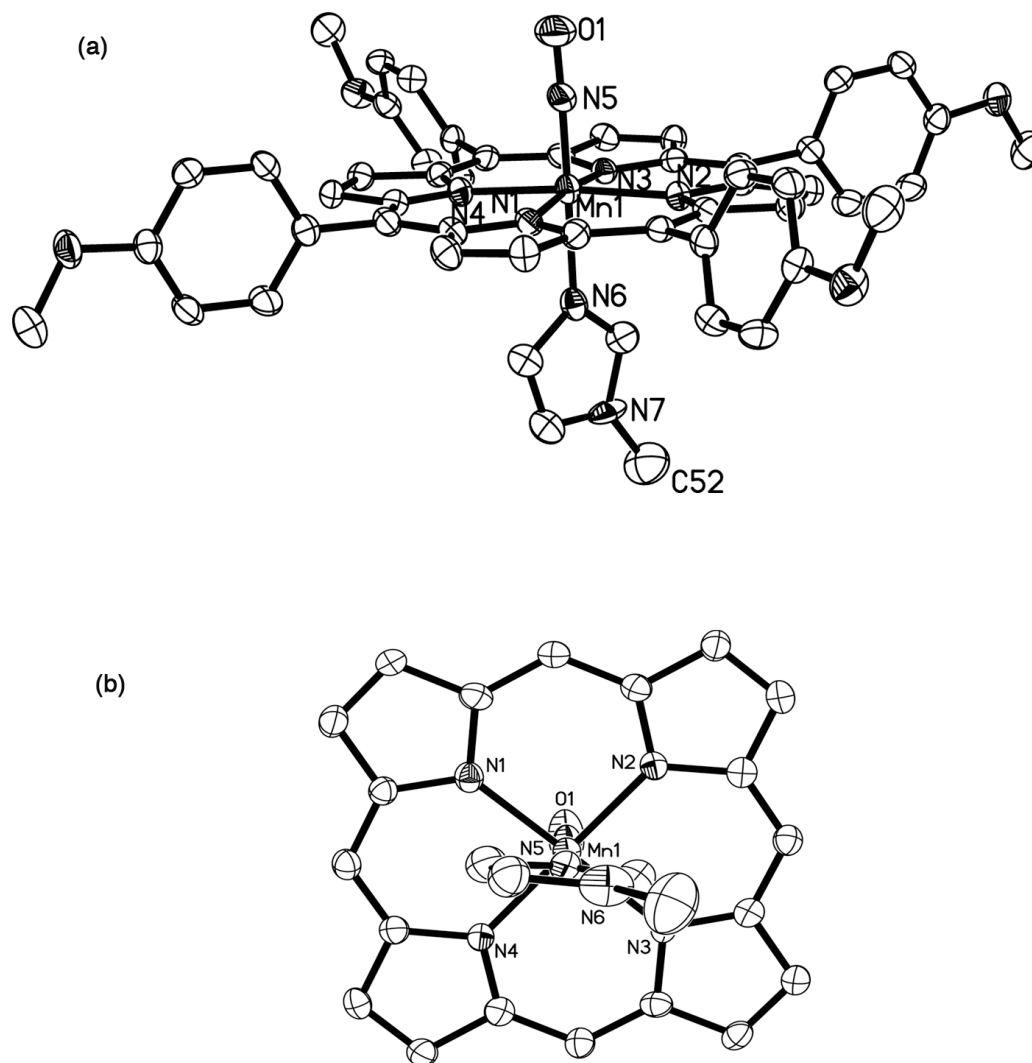


**Figure 3.6.** (a) Molecular structure of  $(T(p\text{-OCH}_3)\text{PP})\text{Mn}(\text{NO})(1\text{-MeIm})$ . Hydrogen atoms have been omitted for clarity. (b) View of the orientation of the 1-MeIm ligand relative to the porphyrin skeleton. The porphyrin *p*-methoxyphenyl substituents have been omitted for clarity.

### 3.3.3 Fiber-optic Infrared Spectroelectrochemical Studies of

*(por)Mn(NO)(1-MeIm) (por = TPP, TTP, and T(p-OCH<sub>3</sub>)PP) in Nonaqueous*

*Media.* We have examined the electrochemical properties of the three compounds, (TPP)Mn(NO)(1-MeIm), (TTP)Mn(NO)(1-MeIm), and (T(p-OMe)PP)Mn(NO)(1-MeIm) at a platinum disc electrode in a typically non-coordinating solvent (CH<sub>2</sub>Cl<sub>2</sub>) and in a coordinating solvent (THF). The electrochemical properties for the three compounds are similar within a given set of conditions of solvent and temperature. The data for (T(p-OCH<sub>3</sub>)PP)Mn(NO)(1-MeIm) will be described as a representative example. The data for the other two compounds are presented in Tables 3.3 and 3.4. We will consider oxidation processes first, followed by the reduction processes.

*(a) Oxidations.* The cyclic voltammogram of (T(p-OCH<sub>3</sub>)PP)Mn(NO)(1-MeIm) at 100 mV s<sup>-1</sup> in CH<sub>2</sub>Cl<sub>2</sub>/0.1M NBu<sub>4</sub>PF<sub>6</sub> is shown in Figure 3.7. The compound exhibits a chemically irreversible oxidation at  $E_{pa}(1) = -0.15$  V (peak 1 in Figure 3.7) vs the ferrocene-ferrocenium couple as an internal standard, and this oxidation has associated with it a small return reduction peak at  $-0.85$  V (peak 1<sup>//</sup>) coupled with an anodic peak in a chemically reversible manner (not shown). The analysis of the data for the second oxidation ( $E_{pa}(2) = 0.66$  V; peak 2) suggests that this process consists of a slow one-electron transfer followed by a rapid irreversible chemical reaction (see later). The third and fourth oxidations, represented by couples 3/3<sup>'</sup> ( $E^{\circ}(3) = 0.78$  V) and 4/4<sup>'</sup> ( $E^{\circ}(4) = 1.05$  V) respectively, were chemically reversible. In all cyclic voltammograms shown, the primed numbers (e.g., 3<sup>'</sup>) refer to the associated return peaks in reversible processes, whereas the double-primed

numbers (e.g., 1'') refer to peaks associated with products from follow-up chemical reactions.

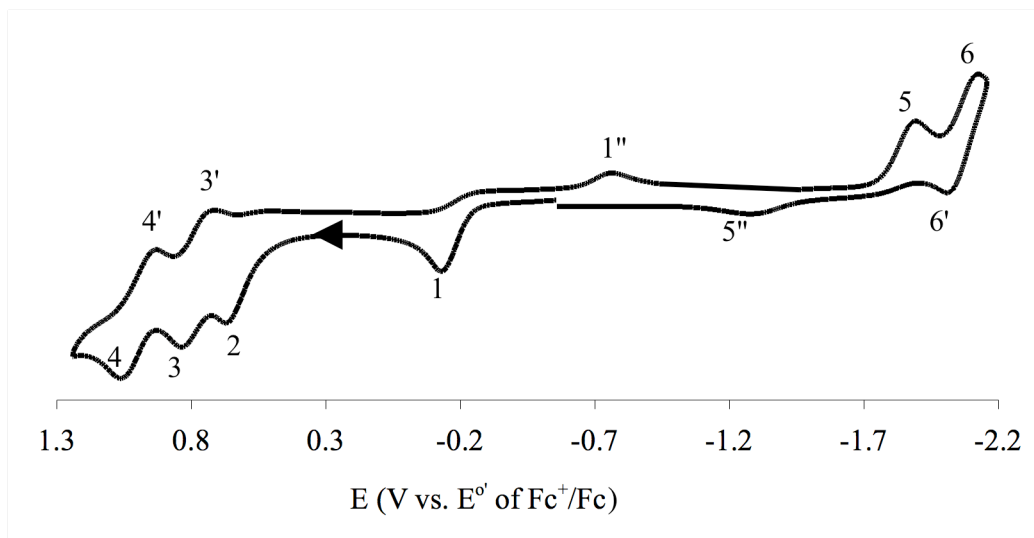
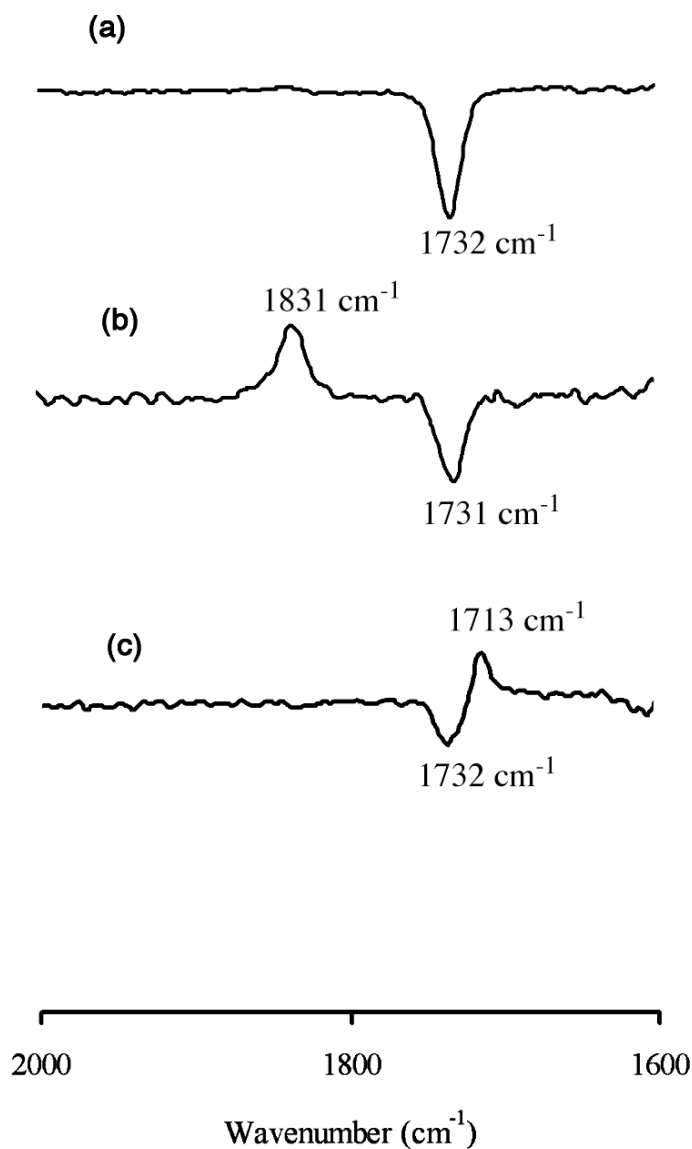


**Figure 3.7.** Cyclic voltammogram of  $(T(p\text{-OCH}_3)\text{PP})\text{Mn}(\text{NO})(1\text{-MeIm})$  in  $\text{CH}_2\text{Cl}_2$  at 23 °C. Conditions: 1 mM analyte, 100 mV/s, 0.1M  $\text{NBu}_4\text{PF}_6$ .

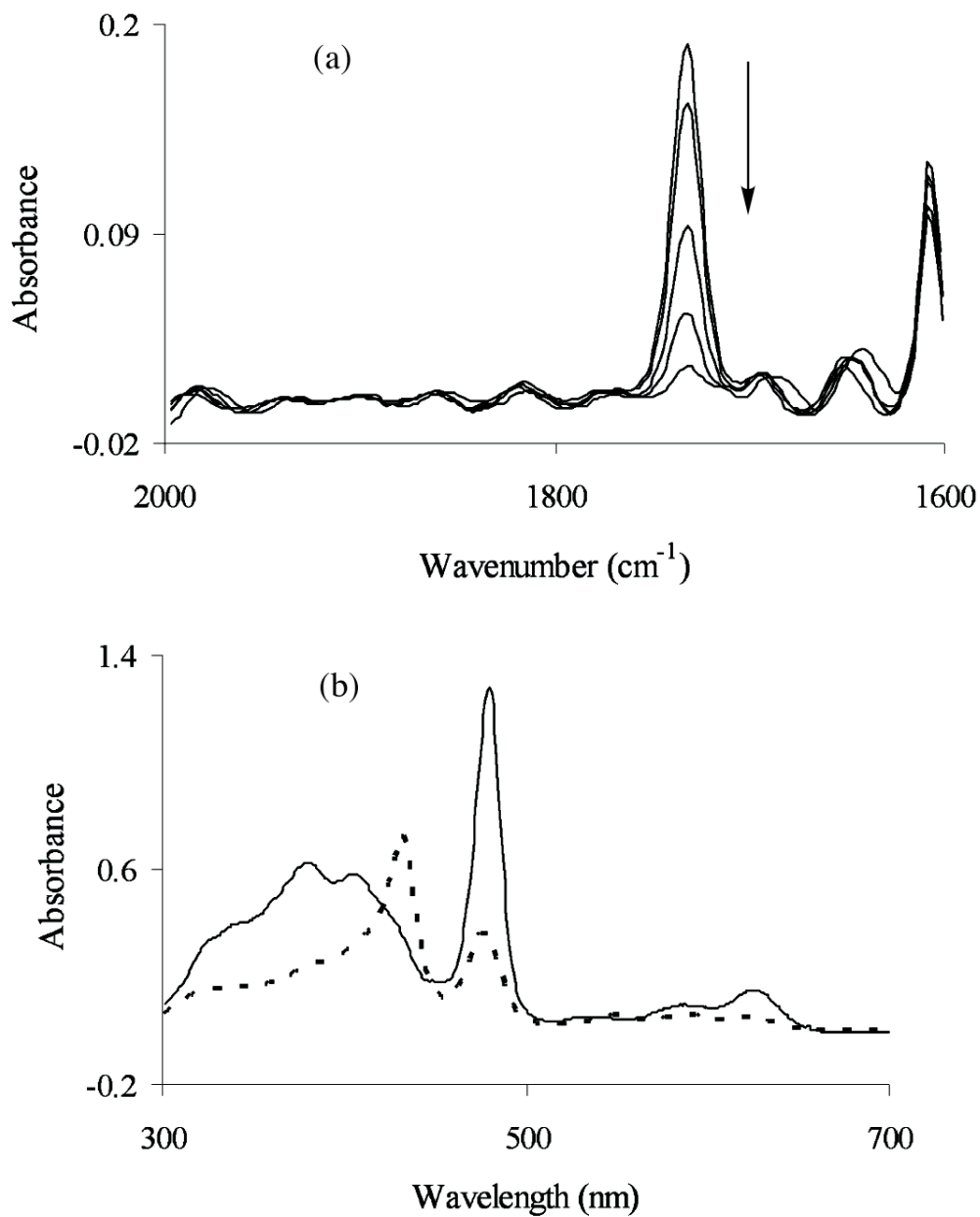
The first oxidation process is chemically irreversible even at higher scan rates up to 1.6 V/s; an analysis of the cyclic voltammograms as a function of scan rate and the geometry of the peak ( $|E_{\text{pa}}(1) - E_{\text{pa}/2}(1)| = 60 \pm 10 \text{ mV}$ ) suggests an electrochemically reversible one-electron transfer followed by a fast irreversible chemical reaction ( $E_r C_i$ ; see later). To investigate the first oxidation process further, fiber-optic IR-potential step experiments were performed at room temperature where the electrode was held at the potential corresponding to the first oxidation peak for 70 s while FTIR spectra were collected, and a cyclic voltammogram was recorded immediately after this period. The difference IR spectrum, where the unoxidized  $(T(p\text{-OCH}_3)\text{PP})\text{Mn}(\text{NO})(1\text{-MeIm})$  was used as the background/reference is shown in

Figure 3.8a. The data reveal a consumption of starting (T(*p*-OCH<sub>3</sub>)PP)Mn(NO)(1-MeIm) near the electrode surface after the first oxidation, indicated by the loss of the NO stretching frequency at 1732 cm<sup>-1</sup> (i.e., the negative peak in Figure 3.8a) without formation of a new nitrosyl-containing species.

Bulk electrolysis at the first oxidation potential was performed on (T(*p*-OCH<sub>3</sub>)PP)Mn(NO)(1-MeIm), and IR and UV-vis spectra were collected during the electrolysis experiment (Figures 3.9a and 3.9b, respectively). Coulombic integration of one Faraday equivalent was obtained from the experiment for the first oxidation process. The IR spectra in Figure 3.9a show the loss of NO from the compound (similar to that observed in Figure 3.8a), and the UV-vis spectra show the conversion to a Mn<sup>III</sup> species<sup>28,45</sup>; the initial Soret band at  $\lambda$  429 nm is converted into two split broad bands at 384 and 411 nm, and the Q band at 481 nm remains at the same position but becomes more intense. This implies that the first oxidation results in a net formal oxidation at the metal center at the timescale of the bulk electrolysis with concomitant loss of NO, similar to that observed for (TPP)Mn(NO).



**Figure 3.8.** Difference IR spectra of  $(T(p\text{-OCH}_3)\text{PP})\text{Mn}(\text{NO})(1\text{-MeIm})$  and its products in  $\text{CH}_2\text{Cl}_2$ : (a) showing the consumption of starting  $(T(p\text{-OCH}_3)\text{PP})\text{Mn}(\text{NO})(1\text{-MeIm})$  after the first oxidation without the formation of a new nitrosyl-containing species at  $23 \text{ }^\circ\text{C}$ , (b) showing the consumption of starting  $(T(p\text{-OCH}_3)\text{PP})\text{Mn}(\text{NO})(1\text{-MeIm})$  after the first oxidation with the concomitant formation of a new nitrosyl-containing species at  $-78 \text{ }^\circ\text{C}$ , and (c) showing the consumption of starting  $(T(p\text{-OCH}_3)\text{PP})\text{Mn}(\text{NO})(1\text{-MeIm})$  and the formation of a new nitrosyl-containing species when the electrode potential is held at half of the peak reduction potential at  $23 \text{ }^\circ\text{C}$ .



**Figure 3.9.** Infrared (a) and UV-visible (b) spectra recorded during the bulk electrolysis (first oxidation) of  $(T(p\text{-OCH}_3)\text{PP})\text{Mn}(\text{NO})(1\text{-MeIm})$  in  $\text{CH}_2\text{Cl}_2$ . Conditions: 1 mM analyte, 0.29 V, 0.1M  $\text{NBu}_4\text{PF}_6$ . The dotted line in (b) represents the spectrum of starting  $(T(p\text{-OCH}_3)\text{PP})\text{Mn}(\text{NO})(1\text{-MeIm})$ .

The low temperature ( $-78\text{ }^{\circ}\text{C}$ ) cyclic voltammogram of  $(\text{T}(p\text{-OCH}_3)\text{PP})\text{Mn}(\text{NO})(1\text{-MeIm})$  in  $\text{CH}_2\text{Cl}_2$  is shown in Figure 3.10, and it shows that the first oxidation process becomes *chemically reversible* ( $E^{\circ}(1) = -0.19\text{ V}$ ) at low temperature. The difference IR spectra obtained after the first oxidation is shown in Figure 3.8b (see Discussion). The other chemically reversible oxidation peaks, at  $E^{\circ}(2) = 0.57\text{ V}$  (couple 7/7') and  $E^{\circ}(3) = 0.91\text{ V}$  (couple 8/8'), are attributed to further oxidation of this cationic species at low temperature.

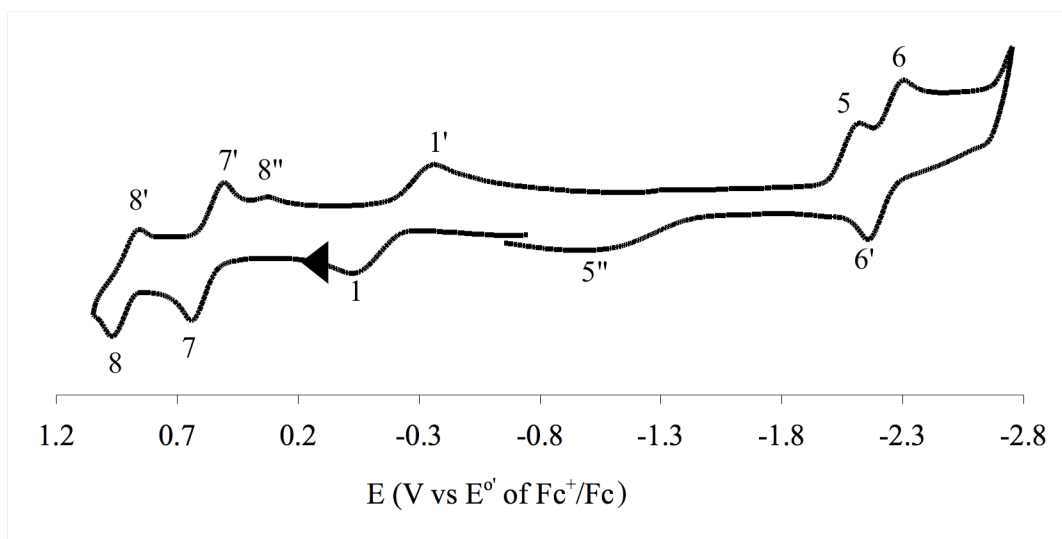


**Figure 3.10.** Cyclic voltammogram of  $(\text{T}(p\text{-OCH}_3)\text{PP})\text{Mn}(\text{NO})(1\text{-MeIm})$  in  $\text{CH}_2\text{Cl}_2$  at  $-78\text{ }^{\circ}\text{C}$ . Conditions: 1 mM analyte, 100 mV/s, 0.1M  $\text{NBu}_4\text{PF}_6$ .

The cyclic voltammogram of  $(\text{T}(p\text{-OCH}_3)\text{PP})\text{Mn}(\text{NO})(1\text{-MeIm})$  in the coordinating solvent THF is shown in Figure 3.11. The compound exhibits an irreversible oxidation (peak 1;  $E_{\text{pa}}(1) = -0.05\text{ V}$ ) in this solvent, similar to that seen in  $\text{CH}_2\text{Cl}_2$ . Monitoring the first oxidation in THF by IR spectroelectrochemistry reveals the loss of the NO band at  $1739\text{ cm}^{-1}$  due to  $(\text{T}(p\text{-OCH}_3)\text{PP})\text{Mn}(\text{NO})(1\text{-MeIm})$

without build-up of a new NO-containing species (similar to that observed in Figure 3.8a). There is no significant difference in the electrochemistry of (T(*p*-OCH<sub>3</sub>)PP)Mn(NO)(1-MeIm) in THF at -78 °C and at 23 °C.

Tables 3.3-3.5 summarize the electrochemical data for the three (por)Mn(NO)(1-MeIm) compounds in both solvents.

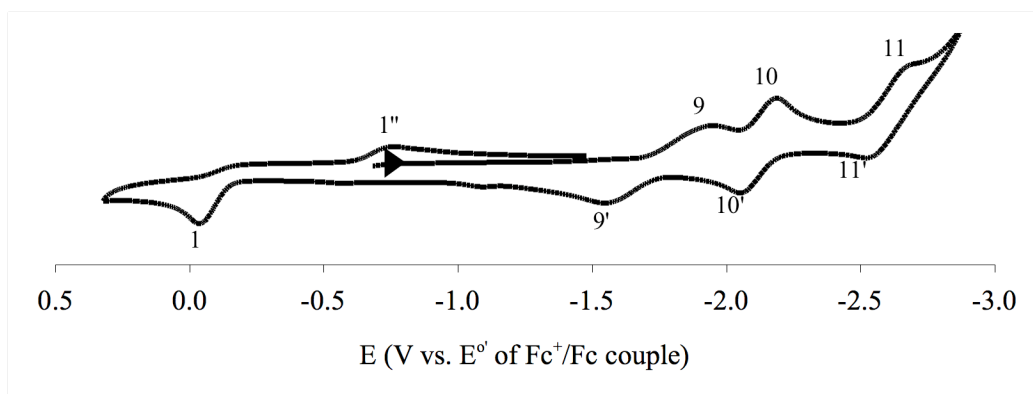


**Figure 3.11.** Cyclic voltammogram of (T(*p*-OCH<sub>3</sub>)PP)Mn(NO)(1-MeIm) in THF at 23 °C. Conditions: 1 mM analyte, 100 mV/s, 0.1M NBu<sub>4</sub>PF<sub>6</sub>.

**Table 3.3.** Infrared ( $\text{cm}^{-1}$ ) and Electrochemical Data for the (por)Mn(NO)(1-MeIm) Compounds in  $\text{CH}_2\text{Cl}_2$  at  $23\text{ }^\circ\text{C}$ .<sup>a</sup>

Por	$\nu_{\text{NO}}$	Oxidations				Reductions	
		$E_{\text{pa}}(1)$	$E_{\text{pa}}(2)$	$E^{\circ}(3)$	$E^{\circ}(4)$	$E_{\text{pc}}(5)$	$E^{\circ}(6)$
TPP	1735	-0.12	0.70	0.89	1.10	-1.93	-2.11
TTP	1731	-0.15	0.69	0.83	1.05	-1.95	-2.05
T( <i>p</i> -OCH <sub>3</sub> )PP	1732	-0.15	0.66	0.78	1.05	-1.94	-2.02

<sup>a</sup> Potentials are in volts, and are referenced to the ferrocene-ferrocenium couple set at 0.00 V. Conditions: 1 mM analyte, 100 mV/s, 0.1 M NBu<sub>4</sub>PF<sub>6</sub>.

**Table 3.4.** Electrochemical Data for the (por)Mn(NO)(1-MeIm) Compounds in  $\text{CH}_2\text{Cl}_2$  at  $-78\text{ }^\circ\text{C}$ .<sup>a</sup>

Por	Oxidations			Reductions	
	$E^{\circ}(1)$	$E^{\circ}(7)$	$E^{\circ}(8)$	$E_{\text{pc}}(5)$	$E^{\circ}(6)$
TPP	-0.15	0.94	1.22	-2.24	-2.32
TTP	-0.16	0.74	1.10	-2.20	-2.26
T( <i>p</i> -OCH <sub>3</sub> )PP	-0.19	0.57	0.91	-2.15	-2.20

<sup>a</sup> Potentials are in volts, and are referenced to the ferrocene-ferrocenium couple set at 0.00 V. Conditions: 1 mM analyte, 100 mV/s, 0.1 M NBu<sub>4</sub>PF<sub>6</sub>.

**Table 3.5.** Infrared ( $\text{cm}^{-1}$ ) and Electrochemical Data for the (por)Mn(NO)(1-MeIm) Compounds in THF at 23 °C.<sup>a</sup>

Por	$\nu_{\text{NO}}$	Oxidation	Reductions		
		$E_{\text{pa}}(1)$	$E^{\circ/}(9)$	$E^{\circ/}(10)$	$E^{\circ/}(11)$
TPP	1741	-0.01	-1.74	-2.11	-2.59
TTP	1740	-0.03	-1.73	-2.10	-2.59
T( <i>p</i> -OCH <sub>3</sub> )PP	1739	-0.05	-1.74	-2.12	-2.60

<sup>a</sup> Potentials are in volts, and are referenced to the ferrocene-ferrocenium couple set at 0.00 V. Conditions: 1 mM analyte, 100 mV/s, 0.1 M NBu<sub>4</sub>PF<sub>6</sub>.

**(b) Reductions.** The reduction behavior of the (por)Mn(NO)(1-MeIm) compounds at low temperature were not different from those observed at room temperature. The cyclic voltammogram of (T(*p*-OCH<sub>3</sub>)PP)Mn(NO)(1-MeIm) in CH<sub>2</sub>Cl<sub>2</sub> displays a chemically irreversible peak at -1.94 V (peak 5 in Figure 3.7) that has with it an associated small return peak at -1.25 V (labeled 5'' in the Figure). The ratio  $i_{\text{pc}}(5)/\nu^{1/2}$  increased linearly with increase in scan rate. In addition, the peak geometry  $|E_{\text{pc}}(5) - E_{\text{pc}1/2}(5)|$  remained essentially constant at 62 mV over the potential scan range 50–1000 mV/s.

The product of the first reduction of (T(*p*-OCH<sub>3</sub>)PP)Mn(NO)(1-MeIm) was examined by IR spectroelectrochemistry. Figure 3.8c shows the difference IR spectrum when the electrode was held at the mid-point potential  $E_{\text{pc}/2}(5)$ . The spectrum shows the presence of a new band that is shifted to a lower wavenumber by 19  $\text{cm}^{-1}$ , assigned to the  $\nu_{\text{NO}}$  of the monoanion [(T(*p*-OCH<sub>3</sub>)PP)Mn(NO)(1-MeIm)]<sup>-</sup>

(there is a slow loss of NO at this potential, however). The other two (por)Mn(NO)(1-MeIm) compounds display similar  $\nu_{\text{NO}}$  shifts ( $\Delta\nu_{\text{NO}} = 22 \text{ cm}^{-1}$  for TPP, and  $21 \text{ cm}^{-1}$  for TTP).

In THF, the compound shows a chemically reversible reduction with slow electron-transfer kinetics (Figure 3.11, peak 9; with an associated peak 9'), and two chemically reversible reductions (couples 10/10' and 11/11') on the cyclic voltammetry timescale.

*(c) Discussion.* As mentioned earlier, the electrochemical properties of the three (por)Mn(NO)(1-MeIm) complexes are similar. Hence, the more general “por” macrocycle will be used in the equations described below. The cyclic voltammogram of (T(*p*-OCH<sub>3</sub>)PP)Mn(NO)(1-MeIm) in CH<sub>2</sub>Cl<sub>2</sub>/[Bu<sub>4</sub>N]PF<sub>6</sub> is shown in Figure 3.7, and the cyclic voltammograms of the (por)Mn(NO)(1-MeIm) compounds reveal an interesting comparison with that of (TPP)Mn(NO) in CH<sub>2</sub>Cl<sub>2</sub>/[Bu<sub>4</sub>N]ClO<sub>4</sub> reported earlier by Kadish and coworkers.<sup>26</sup>

*(i) Oxidations.* The first oxidation of (T(*p*-OCH<sub>3</sub>)PP)Mn(NO)(1-MeIm) is irreversible, and the peak geometry indicates an *E<sub>c</sub>* mechanism for the first oxidation. This peak geometry is similar to that determined for (TPP)Mn(NO)<sup>26</sup> in which NO dissociation has been shown to occur after the first oxidation process. The first oxidation of the related (TPP)Mn(NO)(1-MeIm) compound (−0.12 V; Table 3.3) occurs at a more negative potential than that required for the first oxidation of the five-coordinate (TPP)Mn(NO) (−0.01 vs Fc), and this is due to the destabilization of the Mn(II) formal oxidation state relative to the Mn(III) state in the six-coordinate (por)Mn(NO)(1-MeIm) compounds.

Our IR spectroelectrochemical studies (Figure 3.8a) are consistent with the loss of the NO ligand after the first oxidation of  $(T(p\text{-OCH}_3)\text{PP})\text{Mn}(\text{NO})(1\text{-MeIm})$  without formation of a new NO-containing species. Further evidence of the loss of NO upon oxidation comes from the detection of NO gas in the headspace of a  $\text{CH}_2\text{Cl}_2$  solution of  $(\text{TTP})\text{Mn}(\text{NO})(1\text{-MeIm})$  (1.7 mM) upon chemical oxidation using the TDLAS technique (Figure 3.12).<sup>46</sup>

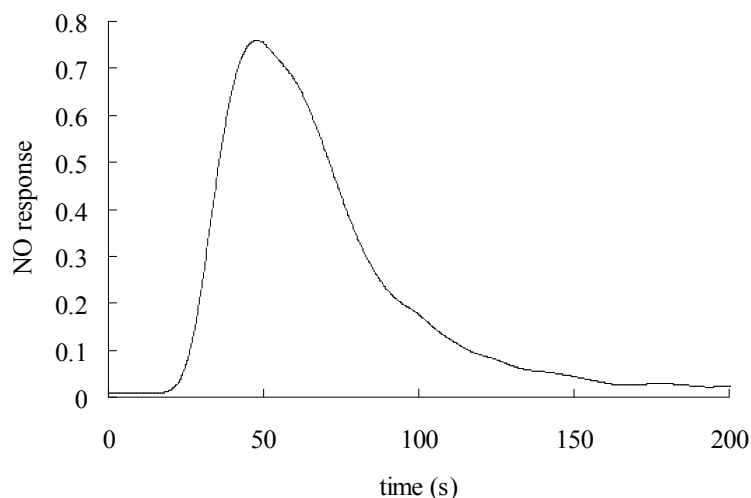


**Figure 3.12.** NO release from  $(\text{TTP})\text{Mn}(\text{NO})(1\text{-MeIm})$  (1.7 mM in  $\text{CH}_2\text{Cl}_2$ ) after addition of  $\text{AgBF}_4$  (10 mM) at time  $t = \sim 20$  sec.

Thus, we assign the first oxidation to the  $E_rC_i$  process described by eqs 3.3 and 3.4.



Indeed, adding a sample of the known compound (TPP)Mn(1-MeIm)<sup>44,47</sup> to the solution of (TPP)Mn(NO)(1-MeIm) during the cyclic voltammetry experiments resulted in an increase in the intensity of the redox couple at  $E^{o'} = -0.77$  V associated with the 1'' peak in Figure 3.7 (i.e., eq 3.5),



as expected if  $[(\text{por})\text{Mn}(1\text{-MeIm})]^+$  was indeed produced from eq 3.4. The intensities of the peaks in Figure 3.7 associated with the second (peak 2), third (couple 3/3'), and fourth (couple 4/4') oxidations also increased as well, suggesting that these further oxidations are due to electrogenerated  $[(\text{por})\text{Mn}(1\text{-MeIm})]^+$  or its products. This Mn(III)/Mn(II) couple (eq 3.5) is similar to the Mn(III)/Mn(II) couple determined for (TPP)MnCl in CH<sub>2</sub>Cl<sub>2</sub>/[Bu<sub>4</sub>N]BF<sub>4</sub> (-0.81 V)<sup>48</sup> and in CH<sub>2</sub>Cl<sub>2</sub>/[Bu<sub>4</sub>N]ClO<sub>4</sub> (-0.78V).<sup>26</sup>

The irreversibility of peak 2 in Figure 3.7 suggests a loss of the axial 1-MeIm ligand after this second oxidation (eqs 3.6 and 3.7).



We note that the previously reported second (*reversible*) oxidation of the five-coordinate (TPP)Mn(NO) compound (presumably the reversible oxidation of electrogenerated [(TPP)Mn]<sup>+</sup>) is at  $E_{1/2} = 0.69$  V (vs Fc),<sup>26</sup> whereas the second

(*irreversible*) oxidation of (TPP)Mn(NO)(1-MeIm) is at  $E_{pa}(2) = 0.70$  V. This difference is not unexpected, since the products of the first oxidation of (TPP)Mn(NO) and (TPP)Mn(NO)(1-MeIm) are different. Indeed, this result is consistent with the presence of 1-MeIm in the latter compound making it easier to oxidize.

The large difference between  $E_{pa}(1)$  and  $E_{pa}(2)$  is not inconsistent with a change from a metal-centered oxidation ( $E_{pa}(1)$ ) to a ring-centered oxidation ( $E_{pa}(2)$ ). The relatively smaller difference between the second and third oxidations ( $|E^{o'}(3) - E_{pa}(2)| = 0.12$  V), and the third and fourth oxidations ( $|E^{o'}(4) - E^{o'}(3)| = 0.27$  V) suggests ring-centered redox processes.<sup>29</sup>

Rogers and Goff<sup>49</sup> have examined the products of chemical and electrochemical oxidation of tetraarylporphyrin manganese complexes in  $\text{CH}_2\text{Cl}_2$ , and have proposed the formation of isoporphyrins from some highly oxidized (por)MnX compounds (por = TPP, TMP; X = Cl, OAc). For example, a peak at +0.6 V vs SCE in the room temperature cyclic voltammogram of (TPP)MnX was tentatively assigned to an isoporphyrin derivative. In the presence of 4-Mepy, however, the peak assigned to the isoporphyrin was not observed.<sup>49</sup> We do not observe such a 0.6 V peak (0.14 V vs Fc) in our experiments involving the (por)Mn(NO)(1-MeIm) compounds on the cyclic voltammetry timescale, although we cannot rule out the formation of such species on longer experimental timescales.

We focused on the identities of the products of the first oxidation processes for the (por)Mn(NO)(1-MeIm) compounds, and we were interested in stabilizing the first oxidation products at low temperature. Our group have previously reported a

simple infrared reflectance spectroelectrochemical set-up for the study of short-lived species generated at the electrode surface.<sup>32</sup> We have modified the glassware slightly to allow for jacketing of the cell compartment with a dry ice bath, and we have found this practical for low temperature infrared spectroelectrochemistry.

The cyclic voltammogram of (T(*p*-OCH<sub>3</sub>)PP)Mn(NO) in CH<sub>2</sub>Cl<sub>2</sub> at -78 °C is shown in Figure 3.10, reveals that the product of the first oxidation (eq 3.3) is indeed stabilized at low temperature.



Further evidence for a stable [(por)Mn(NO)(1-MeIm)]<sup>+</sup> oxidation product from eq 3.3 comes from IR spectroelectrochemistry at -78 °C. The difference IR spectrum upon oxidation of (T(*p*-OCH<sub>3</sub>)PP)Mn(NO)(1-MeIm) at -78 °C is shown in Figure 3.8b, and it reveals a new IR  $\nu_{\text{NO}}$  band that is 100 cm<sup>-1</sup> *higher* in energy than that of the parent compound. Such a large shift in  $\nu_{\text{NO}}$  is indicative of metal-NO-centered oxidations in nitrosyl metalloporphyrins, although larger  $\nu_{\text{NO}}$  shifts of 166-187 cm<sup>-1</sup> have been observed upon similar electrooxidations of some iron nitrosyl porphyrins;<sup>50</sup> however, these latter cases likely involve a change in geometry of the FeNO linkages from bent to linear. The other two (por)Mn(NO)(1-MeIm) compounds have similar  $\nu_{\text{NO}}$  shifts ( $\Delta\nu_{\text{NO}} = 111$  cm<sup>-1</sup> for TPP, and 108 cm<sup>-1</sup> for TTP; spectra not shown) upon low-temperature oxidations in CH<sub>2</sub>Cl<sub>2</sub>.

Follow-up reversible redox processes are observed in the cyclic voltammogram of (T(*p*-OCH<sub>3</sub>)PP)Mn(NO)(1-MeIm), as observed in Figure 3.10, and we assign these tentatively to the processes described by eqs 3.8 and 3.9.



The product of eq 3.9 is not very stable, generating a secondary species with an associated peak at 8'' in Figure 3.10. The large 1/1' peak separation ( $\Delta E = 315$  mV) in Figure 3.10 suggests slow electron transfer kinetics for this metal-centered process, relative to the fast electron processes associated with the ring-centered 7/7' and 8/8' redox couples. In general, the voltammograms shown in Figures 3.7 and 3.10 are representative of the voltammograms obtained for all three (por)Mn(NO)(1-MeIm) compounds in CH<sub>2</sub>Cl<sub>2</sub>.

We also examined the redox behavior of the compounds in the coordinating solvent THF. The first oxidation is irreversible, and we suggest an electrochemical oxidation (eq. 3.3) followed by loss of NO involving coordination of the solvent (eq. 3.10).



The peak at 1<sup>//</sup> can then be represented by the reduction of the product of eq. 3.10 (i.e., eq. 3.11).



The cyclic voltammogram is not altered when the data are recorded at  $-78\text{ }^\circ\text{C}$ , indicating that THF coordination (eq 3.10) results in a significant denitrosylation of the first oxidation product.

**(ii) Reductions.** The data for the reduction of (T(*p*-OCH<sub>3</sub>)PP)Mn(NO)(1-MeIm) in CH<sub>2</sub>Cl<sub>2</sub> (peak 5 in Figure 3.7) are consistent with an *E<sub>r</sub>C<sub>i</sub>* mechanism (eqs 3.12 and 3.13).



Evidence for the existence of the short-lived  $[(\text{por})\text{Mn}(\text{NO})(1\text{-MeIm})]^-$  monoanion is provided by IR spectroelectrochemistry as shown in Figure 3.8c. The relatively small shift in  $\nu_{\text{NO}}$  ( $\Delta\nu_{\text{NO}}$  19 cm<sup>-1</sup>) upon reduction suggests that the reduction is centered on the porphyrin ring rather than on the MnNO fragment. *The new  $\nu_{\text{NO}}$  band disappears completely at  $E_{\text{pc}}(5)$  or at lower potentials, indicative of a fast rate of NO loss at  $E_{\text{pc}}(5)$ .* The first reduction peak is coupled to a return peak at  $-1.25\text{ V}$  labeled 5<sup>//</sup> in

Figure 3.7. We thus assign peak 5'' to the oxidation of electrogenerated [(T(*p*-OCH<sub>3</sub>)PP)Mn(1-MeIm)]<sup>-</sup> as shown in eq. 3.14.



In the case of the previously reported five-coordinate compound (TPP)Mn(NO), the first reduction process occurs at -1.41 V<sup>26</sup> and is reversible. The reduction of (TPP)Mn(NO)(1-MeIm) thus occurs at a more negative potential (at -1.93 V; Table 3.3), a shift of -0.52 V due to the presence of the axial 1-MeIm ligand. We note that the reduction of (TPP)Mn(NO)(py) also occurs at a potential that is more negative (by -0.40 V) than that needed for (TPP)Mn(NO)<sup>26</sup> and it also exhibits irreversible reduction behavior. In contrast to the first reduction of (TPP)Mn(NO)(1-MeIm) in CH<sub>2</sub>Cl<sub>2</sub>/[Bu<sub>4</sub>N]PF<sub>6</sub>, however, the irreversible reduction of (TPP)Mn(NO)(py) in CH<sub>2</sub>Cl<sub>2</sub>/[Bu<sub>4</sub>N]ClO<sub>4</sub> results in the loss of the axial py ligand rather than NO on the cyclic voltammetry timescale.

A second chemically reversible reduction in CH<sub>2</sub>Cl<sub>2</sub> (represented by the 6/6' couple in Figure 3.7) is thus attributed to the reduction of the electrogenerated [(por)Mn(1-MeIm)]<sup>-</sup> species.

We attribute the first reduction of (T(*p*-OCH<sub>3</sub>)Mn(NO)(1-MeIm) in THF (peak 9 in Figure 3.11) to the process described by eq 3.12. However, the slow loss of NO upon reduction in THF suggests an additional process (eq 3.15) which may be intimately coupled with eq 3.12.



This positive shift in the first reduction potential in THF (−1.74 V) compared to that in CH<sub>2</sub>Cl<sub>2</sub> (−1.94 V) is indicative of solvent coordination in the product. Consistent with this is the observation that holding the potential at  $E_{\text{pc}}(9)$  or at values more negative to this value results in complete loss of NO.

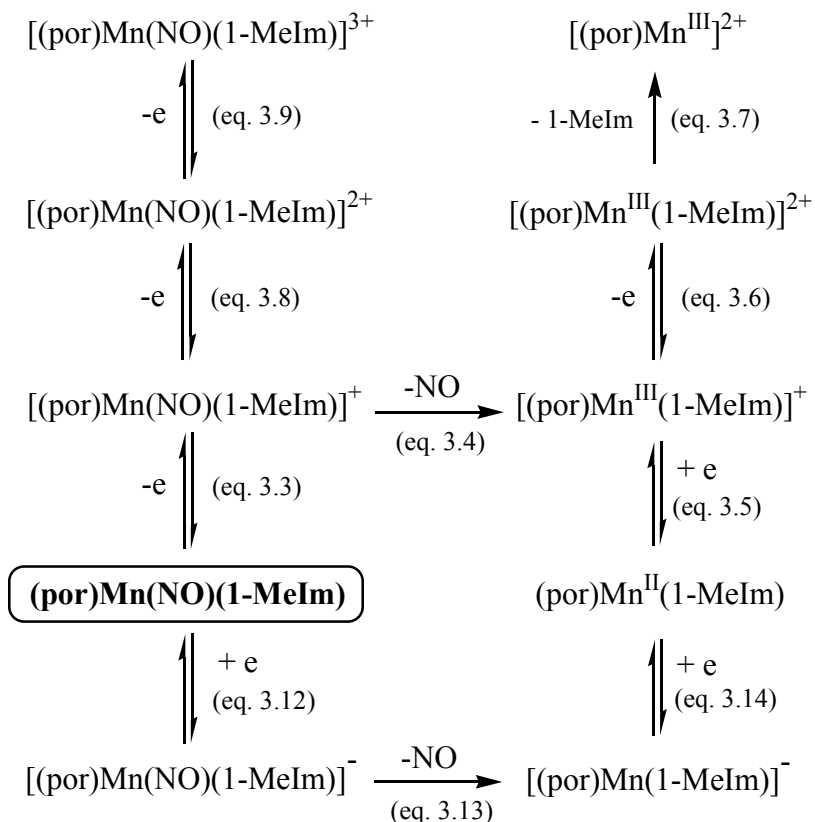
Interesting comparisons can thus be made between the electroreductions of the  $(\text{por})\text{Mn}(\text{NO})(1\text{-MeIm})$  complexes and the electroreductions of the five-coordinate  $(\text{TPP})\text{Mn}(\text{NO})$  compound in the presence of Lewis bases. Reduction of  $(\text{TPP})\text{Mn}(\text{NO})$  in the mixed solvent systems CH<sub>2</sub>Cl<sub>2</sub>/DMF, CH<sub>2</sub>Cl<sub>2</sub>/Me<sub>2</sub>SO, and CH<sub>2</sub>Cl<sub>2</sub>/py, results in the formation of the  $[(\text{TPP})\text{Mn}(\text{NO})(\text{S})]^-$  anion (S = donor solvent); NO remains coordinated in the shorter timescale of cyclic voltammetry, but is dissociated at longer experimental timescales.<sup>26</sup> For example, in neat pyridine, the electrochemical reduction of  $(\text{TPP})\text{Mn}(\text{NO})(\text{py})$  is neat and reversible, and produces  $[(\text{TPP})\text{Mn}(\text{NO})(\text{py})]^-$ .

The other two redox processes (couples 10/10' and 11/11') are thus due to the reductions of non-nitrosyl containing species and are reversible.

**(d) Summary.** The redox behavior of the  $(\text{por})\text{Mn}(\text{NO})(1\text{-MeIm})$  compounds in CH<sub>2</sub>Cl<sub>2</sub> at room temperature and at −78 °C may be summarized as shown in Scheme 3.1. As mentioned before, only one other electrochemical study of manganese nitrosyl porphyrins was reported prior to this study, namely that of the five-coordinate compound  $(\text{TPP})\text{Mn}(\text{NO})$ .<sup>26</sup>

The first oxidation of (por)Mn(NO)(1-MeIm) at room temperature is essentially irreversible and follows an  $E_rC_i$  mechanism resulting in the net loss of NO (eqs 3.3 and 3.4). This is similar to that reported for (TPP)Mn(NO) (i.e., denitrosylation upon oxidation), except that in the present study the product of the first oxidation is a five-coordinate [(por)Mn(1-MeIm)]<sup>+</sup> species which undergoes an irreversible oxidation (eqs 3.6 and 3.7) to lose the axial ligand. We have stabilized the product of the first oxidation (eq 3.3) by recording the redox behavior at -78 °C. At this temperature, the initial oxidized product [(por)Mn(NO)(1-MeIm)]<sup>+</sup> undergoes two further reversible oxidations (eqs 3.8 and 3.9). The reduction behavior of (por)Mn(NO)(1-MeIm) is different from that of the five-coordinate (TPP)Mn(NO). In the case of (TPP)Mn(NO),<sup>26</sup> this compound undergoes two successive reductions without loss of NO. For the six-coordinate (por)Mn(NO)(1-MeIm), however, denitrosylation occurs after the first reduction (eqs 3.12 and 3.13). Importantly, our infrared spectroelectrochemistry set-up<sup>32</sup> which we have now adapted for low-temperature work, has allowed us to identify several of the nitrosyl-containing species in the redox reactions of the six-coordinate manganese nitrosyl porphyrins (por)Mn(NO)(1-MeIm).

### Scheme 3.1



### 3.4 Conclusion

Our study complemented previous structural studies by Scheidt and coworkers<sup>25,34</sup> on the five- coordinate (TTP)Mn(NO) and the six- coordinate (TPP)Mn(NO)(4-Mepip) (TPP = tetraphenylporphyrinato dianion) compounds. In summary, we have prepared several isolable six-coordinate manganese nitrosyl porphyrins and have characterized them by spectroscopy. Our successful crystallization of four of these derivatives, which were characterized by single-crystal X-ray crystallography, significantly increases the number of available structures of

manganese nitrosyl porphyrins. In particular, the *trans* influence of the linear NO group observed in these structures provides a convenient entry into further studies of this structural effect. Comparisons between these manganese(II) nitrosyl derivatives and the ferric nitrosyl derivatives suggest that there are structural similarities between these formally isoelectronic Mn<sup>II</sup>-NO and Fe<sup>III</sup>-NO species. However, care must be taken in the interpretation of these results, since subtle  $\pi$ -backbonding differences exist between them.

We also studied the room and low temperature ( $-78\text{ }^{\circ}\text{C}$ ) cyclic voltammetric behavior of the six coordinate (por)Mn(NO)(1-MeIm) (por = TPP, TTP, or T(*p*-OCH<sub>3</sub>)PP) complexes at a Pt disc electrode in two nonaqueous solvents (CH<sub>2</sub>Cl<sub>2</sub> and THF). This study significantly increased the number of the manganese nitrosyl porphyrin complexes that have been electrochemically characterized in the literature and represent the only spectroelectrochemically characterized manganese nitrosyl porphyrin complexes in the literature.

### 3.5 References

- (1) Cheng, L.; Richter-Addo, G. B. In *The Porphyrin Handbook*; Guillard, R., Smith, K., Kadish, K. M., Eds.; Academic Press: New York, 2000; Vol. 4 (Biochemistry and Binding: Activation of Small Molecules), p 219-291.
- (2) Deinum, G.; Stone, J. R.; Babcock, G. T.; Marletta, M. A. *Biochemistry* **1996**, *35*, 1540-1547.
- (3) Ballou, D. P.; Zhao, Y.; Brandish, P. E.; Marletta, M. A. *Proc. Natl. Acad. Sci., USA* **2002**, *99*, 12097-12101, and references therein.
- (4) Dierks, E. A.; Hu, S.; Vogel, K. M.; Yu, A. E.; Spiro, T. G.; Burstyn, J. N. *J. Am. Chem. Soc.* **1997**, *119*, 7316-7323.
- (5) Kharitonov, V. G.; Sharma, V. S.; Magde, D.; Koesling, D. *Biochemistry* **1997**, *36*, 6814-6818.
- (6) Ford, P. C.; Lorkovic, I. M. *Chem. Rev.* **2002**, *102*, 993-1017.
- (7) Walker, F. A.; Monfort, W. R. *Adv. Inorg. Chem.* **2001**, *51*, 295-358.

- (8) Wyllie, G. R. A.; Scheidt, W. R. *Chem. Rev.* **2002**, *102*, 1067-1089.
- (9) Westcott, B. L.; Enemark, J. H. In *Inorganic Electronic Structure and Spectroscopy*; Lever, A. B. P., Solomon, E. I., Eds.; Wiley and Sons: New York, 1999; Vol. 2 (Applications and Case Studies), p Chapter 7.
- (10) Enemark, J. H.; Feltham, R. D. *Coord. Chem. Rev.* **1974**, *13*, 339-406.
- (11) Feltham, R. D.; Enemark, J. H. *Top. Stereochem.* **1981**, *12*, 155-215.
- (12) Yonetani, T.; Yamamoto, H.; Erman, J. E.; J. S. Leigh, J.; Reed, G. H. *J. Biol. Chem.* **1972**, *247*, 2447-2455.
- (13) Dickinson, L. C.; Chien, J. C. W. *J. Biol. Chem.* **1977**, *252*, 6156-6162.
- (14) Hemmens, B.; Gorren, A. C. F.; Schmidt, K.; Werner, E. R.; Mayer, B. *Biochem. J.* **1998**, *332*, 337-342.
- (15) Bender, A. T.; Kamada, Y.; Kleaveland, P. A.; Osawa, Y. *J. Inorg. Biochem.* **2002**, *91*, 625-634.
- (16) Parthasarathi, N.; Spiro, T. G. *Inorg. Chem.* **1987**, *26*, 2280-2282.
- (17) Hori, H.; Ikeda-Saito, M.; Lang, G.; Yonetani, T. *J. Biol. Chem.* **1990**, *265*, 15028-15033.
- (18) Masuya, F.; Hori, H. *Biochim. Biophys. Acta* **1993**, *1203*, 99-103.
- (19) Gibson, Q. H.; Hoffman, B. M. *J. Biol. Chem.* **1979**, *254*, 4691-4697.
- (20) Lan, E. H.; Dave, B. C.; Fukuto, J. M.; Dunn, B.; Zink, J. I.; Valentine, J. S. *J. Mater. Chem.* **1999**, *9*, 45-53.
- (21) Diab, N.; Schuhmann, W. *Electrochim. Acta* **2001**, *47*, 265-273.
- (22) Spasojevic, I.; Batinic-Haberle, I.; Fridovich, I. *Nitric Oxide: Biol. Chem.* **2000**, *4*, 526-533.
- (23) Ferrer-Sueta, G.; Quijano, C.; Alvarez, B.; Radi, R. *Methods Enzymol.* **2002**, *349*, 23-37.
- (24) Shimanovich, R.; Hannah, S.; Lynch, V.; Gerasimchuk, N.; Mody, T. D.; Magda, D.; Sessler, J.; Groves, J. T. *J. Am. Chem. Soc.* **2001**, *123*, 3613-3614 and references therein.
- (25) Scheidt, W. R.; Hatano, K.; Rupprecht, G. A.; Piciulo, P. L. *Inorg. Chem.* **1979**, *18*, 292-299.
- (26) Kelly, S.; Lançon, D.; Kadish, K. M. *Inorg. Chem.* **1984**, *23*, 1451-1458.
- (27) Mu, X. H.; Schultz, F. A. *Inorg. Chem.* **1995**, *34*, 3835-3837.
- (28) Kelly, S. L.; Kadish, K. M. *Inorg. Chem.* **1982**, *21*, 3631-3639.
- (29) Kadish, K. M.; Van Caemelbecke, E.; Royal, G. In *The Porphyrin Handbook*; Kadish, K. M., Smith, K. M., Guillard, R., Eds.; Academic Press: San Diego, CA, 2000; Vol. 8 (Electron Transfer), p Chapter 55. Pages 1-114 (pp 11-44, and 92-93).
- (30) Adler, A. D.; Longo, F. R.; Finarelli, J. D.; Goldmacher, J.; Assour, J.; Korsakoff, L. *J. Org. Chem.* **1967**, *32*, 476.
- (31) Adler, A. D.; Longo, F. R.; Kampas, F.; Kim, J. *J. Inorg. Nucl. Chem.* **1970**, *32*, 2443-2445.
- (32) Shaw, M. J.; Henson, R. L.; Houk, S. E.; Westhoff, J. W.; Jones, M. W.; Richter-Addo, G. B. *J. Electroanal. Chem.* **2002**, *534*, 47-53.
- (33) Connelly, N. G.; Geiger, W. E. *Chem. Rev.* **1996**, *96*, 877-910.

- (34) Piciulo, P. L.; Rupprecht, G.; Scheidt, W. R. *J. Am. Chem. Soc.* **1974**, *96*, 5293-5295.
- (35) Piciulo, P. L.; Scheidt, W. R. *Inorg. Nucl. Chem. Lett.* **1975**, *11*, 309-311.
- (36) Ellison, M. K.; Scheidt, W. R. *J. Am. Chem. Soc.* **1999**, *121*, 5210-5219.
- (37) Yu, N.-T.; Lin, S.-H.; Chang, C. K.; Gersonde, K. *Biophys. J.* **1989**, *55*, 1137-1144.
- (38) Hatano, K.; Anzai, K.; Iitaka, Y. *Bull. Chem. Soc. Jpn.* **1983**, *56*, 422-427.
- (39) Scheidt, W. R.; Pearson, W. B.; Gosal, N. *Acta Crystallogr.* **1988**, *C44*, 927-929.
- (40) Day, V. W.; Stults, B. R.; Tasset, E. L.; Day, R. O.; Marianelli, R. S. *J. Am. Chem. Soc.* **1974**, *96*, 2650-2652.
- (41) Lai, T.-S.; Kwong, H.-L.; Che, C.-M.; Peng, S.-M. *Chem. Commun.* **1997**, 2373-2374.
- (42) Diskin-Posner, Y.; Patra, G. K.; Goldberg, I. *Eur. J. Inorg. Chem.* **2001**, 2515-2523.
- (43) Cheng, B.; Scheidt, W. R. *Acta Crystallogr.* **1996**, *C52*, 585-588.
- (44) Kirner, J. F.; Reed, C. A.; Scheidt, W. R. *J. Am. Chem. Soc.* **1977**, *99*, 2557-2563.
- (45) Boucher, L. J. *J. Am. Chem. Soc.* **1970**, *92*, 2725-2730.
- (46) Yi, J.; Namjou, K.; Zahran, Z. N.; McCann, P. J.; Richter-Addo, G. B. *Nitric Oxide* **2006**, *15*, 154-162.
- (47) Gonzalez, B.; Kouba, J.; Yee, S.; Reed, C. A.; Kirner, J. F.; Scheidt, W. R. *J. Am. Chem. Soc.* **1975**, *97*, 3247-3249.
- (48) Foran, G. J.; Armstrong, R. S.; Crossley, M. J.; Lay, P. A. *Inorg. Chem.* **1992**, *31*, 1463-1470.
- (49) Rodgers, K. R.; Goff, H. M. *J. Am. Chem. Soc.* **1988**, *110*, 7049-7060.
- (50) Mu, X. H.; Kadish, K. M. *Inorg. Chem.* **1988**, *27*, 4720-4725.

## Chapter 4. Ligand Conformations in Derivatives of Manganese- and Cobalt-Substituted Horse Heart Myoglobin As Determined by X-ray Crystallography

### 4.1 Introduction

Heme-containing enzymes serve a wide range of biological functions ranging from oxygen storage and transport, oxoanion reduction, hydrocarbon oxidation and electron transport to multi-electron catalysis.<sup>1-3</sup> The heme prosthetic groups in these enzymes have been replaced by other synthetic metal-hemes mainly to examine their effects on structure and function or to probe the active site via the altered electronic and steric requirements of using different metal ions. Among these metal-hemes, cobalt-<sup>4</sup> and manganese-protoporphyrin IX<sup>5-7</sup> have the greatest attention.

Manganese protoporphyrin IX-reconstituted heme proteins are well known for hemoglobin (Hb),<sup>8,9</sup> myoglobin (Mb),<sup>10-12</sup> cytochrome P450,<sup>13</sup> soluble guanylyl cyclase,<sup>14</sup> cytochrome *c*,<sup>15</sup> nitric oxide synthase,<sup>16</sup> horse radish peroxidase,<sup>9,11,17</sup> cytochrome *b5*,<sup>18</sup> cytochrome *c* peroxidase (CcP),<sup>11,19,20</sup> and prostaglandin H<sub>2</sub> synthase-1.<sup>21</sup> These manganese protoporphyrin IX- reconstituted enzymes were fully characterized by the traditional spectroscopic techniques such as UV-vis,<sup>11,19</sup> resonance Raman,<sup>22,23</sup> EPR,<sup>9</sup> and NMR spectroscopy. However, no X-ray structure of any of these manganese protoporphyrin IX- reconstituted proteins or enzymes was reported except that of the unrefined X-ray difference Fourier crystallographic studies

---

\* Taken in part from;

i-“Crystal Structures of Manganese- and Cobalt-substituted Myoglobin in Complex with NO and Nitrite Reveal Unusual Ligand Conformations” Zahran Z. N.; Chooback L.; Copeland D. M.; West A. H.; Richter-Addo G. B. *J. Inorg. Biochem.* **2007**, in press, with permission from Elsevier.

on the metmanganohemoglobin<sup>24,25</sup> and that recently reported for prostaglandin H<sub>2</sub> synthase-1.<sup>21</sup>

The preparation and functional properties of manganese protoporphyrin IX-reconstituted Mb and its reaction with, oxygen,<sup>11</sup> hydrogen peroxide,<sup>11</sup> carbon monoxide,<sup>11</sup> cyanide, nitrite, azide,<sup>11,26</sup> and nitric oxide<sup>27,28</sup> have been extensively investigated and compared with that of the native iron Mb. Although the protein fold of the native Mb and the manganese protoporphyrin IX-reconstituted Mb are expected to be similar, their ligation properties are quite different. Thus, for example, oxygen, carbon monoxide, cyanide, nitrite, azide, and nitric oxide bind to Mb at the iron-heme moiety, whereas the oxidized or the reduced manganese protoporphyrin IX-reconstituted Mb did not form complexes with oxygen and carbon monoxide.<sup>11</sup> Azide<sup>11,26</sup> binds to the oxidized form, and nitric oxide<sup>23,28</sup> binds to the reduced form of the Mn-heme moiety while cyanide binds to the oxidized Mn<sup>III</sup>Mb away from the Mn-heme moiety.<sup>29</sup>

Interestingly, Mn-substituted hemoglobin (MnHb) exhibits allosteric effects in its binding of NO.<sup>5,7,30,31</sup> The resulting adduct, written simply as Mn<sup>II</sup>HbNO, has been prepared and characterized.<sup>15,31,32</sup> The NO adduct of Mn-substituted Mb is also known,<sup>31,32</sup> as are the NO adducts of Mn-substituted sGC,<sup>14</sup> cytochrome *c*,<sup>15</sup> CcP,<sup>32</sup> cytochrome P450,<sup>13</sup> and that of a monomeric MnHb from the insect *Chironomus thummi thummi*.<sup>33</sup> Lan and coworkers have examined the ability of sol-gel encapsulated Mn<sup>II</sup>Mb to act as an NO sensor under physiological conditions (since it binds NO but not O<sub>2</sub>).<sup>34</sup> We, and others, have prepared and characterized several synthetic manganese porphyrins ((por)Mn) that bind NO.<sup>35-40</sup> In some cases, synthetic

(por)Mn compounds have been shown to electrocatalyze the reduction of NO to hydroxylamine and ammonia.<sup>41</sup>

We are interested in the structures of the heme pockets in Mb derivatives of nitrogen oxides, and in particular how the distal amino acid residues might affect the binding preferences of nitrogen oxide ligands. In this chapter, we describe, for the first time, the crystal structures of Mn-substituted Mb; namely the as-isolated Mn<sup>III</sup>Mb and the reduced Mn<sup>II</sup>Mb derivative. The crystal structures obtained for these compounds may help explain some of the contradictory results on the spectroscopy previously reported in the literature. Azide is a known inhibitor of heme enzymes.<sup>42</sup> The physiological role of nitrite is only now being fully recognized<sup>43,44</sup> and its interaction with Hb and Mb has been shown to result, under conditions of hypoxia, in enzymatic NO production.<sup>43</sup> To this end, we also report the crystal structures of the MnMb adducts with methanol, azide, and nitric oxide (NO). Further, we report the structures of the nitrite adducts of MnMb and CoMb.

## 4.2 Materials and Methods

Manganese(III) protoporphyrin IX chloride ((PPIX)Mn<sup>III</sup>Cl), sodium dithionite (85%), and 2-butanone were purchased from Aldrich Chemical Company. Tris(hydroxymethyl)aminomethane hydrochloride (Tris-HCl, molecular biology grade), and ammonium sulfate (99.5%) were obtained from Fluka. Sodium nitrite (98.0%) was obtained from Baker and Adamson. Cobalt(III) protoporphyrin IX chloride ((PPIX)Co<sup>III</sup>Cl) was purchased from Frontier Scientific Company. Nitric

oxide (98%, Matheson Gas) was passed through KOH pellets and two cold traps (dry ice/acetone,  $-78\text{ }^{\circ}\text{C}$ ) to remove higher nitrogen oxides.

Horse heart *met*-myoglobin (hh *met*Mb) was purchased from Sigma. The heme group was removed from *met*Mb (30 mg/ml) using the method of Yonetani<sup>19</sup> and Teale.<sup>45</sup>  $\text{Mn}^{\text{III}}$ PPIX was reconstituted into apoMb following the method of Yonetani<sup>11</sup> and the product characterized by UV-vis spectroscopy ( $\lambda_{\text{max}}$  378 and 471 nm).<sup>11,12</sup> The  $\text{Co}^{\text{III}}$ Mb complex was similarly prepared and characterized ( $\lambda_{\text{max}}$  425 nm).<sup>4</sup> The purity of the metal-reconstituted myoglobins were established by SDS PAGE.

### 4.3 Crystallization and Complex Formation

All eight Mn- and Co-substituted myoglobin crystalline complexes were prepared and structurally characterized in (at least) duplicate.

**4.3.1  $\text{Mn}^{\text{III}}$ Mb and  $\text{Co}^{\text{III}}$ Mb.** Crystals of  $\text{Mn}^{\text{III}}$ Mb and  $\text{Co}^{\text{III}}$ Mb were grown using identical procedures. The crystals were grown at room temperature ( $\sim 23\text{ }^{\circ}\text{C}$ ) using the hanging-drop vapor diffusion method. A hanging drop (10  $\mu\text{L}$ ) containing 0.45 mM protein (8 mg/mL) and 0.8 M  $(\text{NH}_4)_2\text{SO}_4$  in 10 mM Tris-HCl buffer at pH 7.4, was suspended over a well containing 500  $\mu\text{L}$  of 3.4 M  $(\text{NH}_4)_2\text{SO}_4$  in 10 mM Tris-HCl buffer at pH 7.4. The crystals grew in clusters of plates and reached a suitable size in 3-5 days. A suitable crystal was harvested with a cryoloop, transferred to 10  $\mu\text{L}$  of artificial mother liquor containing 10% glycerol as a cryoprotectant, and flash frozen in liquid nitrogen.

**4.3.2  $Mn^{III}Mb(MeOH)$ .** The  $Mn^{III}Mb(MeOH)$  complex was prepared by adding 20  $\mu$ L MeOH to a  $Mn^{III}Mb$  solution (180  $\mu$ L, 0.9 mM) in 10 mM Tris-HCl buffer at pH 7.4. The mixture was kept at 4°C for 10 min before setting up for crystallization using the hanging drop vapor diffusion method employing the same conditions as described above for  $Mn^{III}Mb$ . A suitable crystal was harvested and soaked for 10 min in a droplet of 10 mM Tris-HCl buffer (pH 7.4) containing  $(NH_4)_2SO_4$  (3.4 M), 10% glycerol as cryoprotectant, and MeOH (2% v/v). The crystal was then flash frozen in liquid nitrogen.

**4.3.3  $Mn^{II}Mb$ .** The reduced  $Mn^{II}Mb$  crystal was obtained by soaking a crystal of  $Mn^{III}Mb$  anaerobically in a 20  $\mu$ L droplet of the buffer (10 mM Tris-HCl, pH 7.4) containing  $(NH_4)_2SO_4$  (3.4 M), 10% glycerol as cryoprotectant, and sodium dithionite (114 mM) for at least 20 min. The crystal and the droplet were submerged in mineral oil under an atmosphere of nitrogen. During the soaking of the crystal, it cracked into several pieces and its color changed from purple-red to orange-red indicative of the formation of the reduced  $Mn^{II}Mb$ .<sup>11,46</sup> A suitable crystal was harvested with a cryoloop and flash frozen in liquid nitrogen.

**4.3.4  $Mb^{III}Mb(N_3^-)$ .** The azide complex was prepared as reported previously<sup>22,26</sup> by adding 20  $\mu$ L of a sodium azide solution (200 mM) directly into a solution of  $Mn^{III}Mb$  (180  $\mu$ L, 0.9 mM) in 10 mM Tris-HCl buffer at pH 7.4. The mixture was left at 4 °C for 10 min, and the resulting azide complex crystallized using the hanging-drop vapor diffusion method employing the same conditions as described above for  $Mn^{III}Mb$ . Crystals grew in 3-5 days. A suitable crystal was harvested and soaked in a 10  $\mu$ L droplet of 10 mM Tris-HCl buffer (pH 7.4)

containing  $(\text{NH}_4)_2\text{SO}_4$  (3.4 M), 10% glycerol as cryoprotectant, and  $\text{NaN}_3$  (200 mM) for 10 min, and flash frozen in liquid nitrogen. The excess  $\text{NaN}_3$  added to the cryoprotectant was to maximize the occupancy of the azide ligand in the complex.

**4.3.5  $\text{Mn}^{\text{II}}\text{MbNO}$ .** This complex was obtained by transferring a crystal of  $\text{Mn}^{\text{II}}\text{Mb}$  into a 10  $\mu\text{L}$  droplet of the buffer (10 mM Tris-HCl, pH 7.4) under anaerobic conditions and submerged in mineral oil. The droplet contained  $(\text{NH}_4)_2\text{SO}_4$  (3.4 M), 10% glycerol as cryoprotectant, and NO ( $\sim 2$  mM). The crystal was soaked in this solution for  $\sim 2$  min, and the color changed from orange-red to pink suggesting formation of the nitrosyl adduct  $\text{Mn}^{\text{II}}\text{MbNO}$ . The crystal was harvested with a cryoloop and flash frozen in liquid nitrogen.

**4.3.6  $\text{Mn}^{\text{III}}\text{Mb}(\text{ONO}^-)$ .** The nitrito-liganded complex,  $\text{Mn}^{\text{III}}\text{Mb}(\text{ONO}^-)$ , was obtained by soaking crystals of  $\text{Mn}^{\text{III}}\text{Mb}$  in a 10  $\mu\text{L}$  droplet of the buffer (10 mM Tris-HCl, pH 7.4) under anaerobic conditions by submerging the droplet in mineral oil. The droplet contained  $(\text{NH}_4)_2\text{SO}_4$  (3.4 M), 7.5% glycerol as cryoprotectant, sodium dithionite (187 mM). Sodium nitrite (to give 100 mM) was then added to the droplet, and the crystal soaked for 2 min in this mixture. The crystals were then harvested with cryoloops and flash frozen in liquid nitrogen. We note that in our hands, the  $\text{Mn}^{\text{III}}\text{Mb}(\text{ONO}^-)$  complex could not be obtained either by soaking the  $\text{Mn}^{\text{III}}\text{Mb}$  crystals in a droplet free of sodium dithionite (but containing the other components), or from co-crystallization of  $\text{Mn}^{\text{III}}\text{Mb}$  in presence of excess  $\text{NaNO}_2$ .

**4.3.7  $\text{Co}^{\text{III}}\text{Mb}(\text{ONO}^-)$ .** The  $\text{Co}^{\text{III}}\text{Mb}(\text{ONO}^-)$  complex was prepared by mixing a solution of  $\text{Co}^{\text{III}}\text{Mb}$  (10 mg/mL) with a solution of  $\text{NaNO}_2$  (0.5 M) solutions in a 1:1 v/v ratio and keeping the mixture at 4  $^\circ\text{C}$  for 30 min. The product was then

crystallized using the vapor diffusion method using the same conditions as used for  $\text{Co}^{\text{III}}\text{Mb}(\text{H}_2\text{O})$ , and suitable size crystals grew in 3-5 days. Suitable crystals were harvested with cryoloops and flash frozen in liquid nitrogen. The complex was also obtained by soaking  $\text{Co}^{\text{III}}\text{Mb}$  crystals in a droplet of Tris-HCl buffer (10 mM, pH 7.4) containing  $(\text{NH}_4)_2\text{SO}_4$  (3.4 M), 10% glycerol as cryoprotectant, and  $\text{NaNO}_2$  (500 mM) for 30 min. However, this latter method resulted in a product containing nitrite at only ~60 % occupancy as determined by crystallography.

#### 4.4 X-ray Diffraction Data Collection and Processing

Diffraction data sets were collected at 100 K by using  $\text{CuK}\alpha$  radiation ( $\lambda = 1.5418 \text{ \AA}$ ) produced from a RigakuMSC RU-H3R X-ray generator operated at 50 kV/100 mA. Diffracted X-rays were detected using an R-AXIS IV<sup>++</sup> dual image plate detector system. The crystal-to-detector distance was set at 100 mm, and 220 frames of data were collected for each crystal, with  $1^\circ$  oscillations and a 5 min exposure time per frame. X-ray intensity data were indexed and processed with the stand-alone *d\*TREK* program (Macintosh v.2D)<sup>47</sup> available from Molecular Structure Corporation.

#### 4.5 Structure Solution and Refinement

The CCP4 Suite of programs<sup>48</sup> was used for structure solution and the subsequent refinement of all structures reported here. Phase information was obtained using molecular replacement as implemented in CCP4 (*MOLREP*).<sup>49</sup> The search model was the 1.3  $\text{\AA}$  resolution structure of  $\text{Mb}^{\text{II}}\text{NO}$  (PDB access code 2FRJ)<sup>50</sup>

with all the solvent molecules, sulfate anions and the NO ligand removed from the structure. After molecular replacement, the iron atom was replaced by manganese or cobalt. In all the structures, no electron density was observed for the C-terminal residue Gly153, thus it was not included in the models. In all cases, *ARP/wARP* was used to add water molecules to the structure during refinement. Lys47 was refined in two positions at 50% occupancy each. Also, two sulfate groups (three in case of reduced Mn<sup>II</sup>Mb) were added to the models based on the initial  $F_o-F_c$  map. After completion of the refinement of the individual structures, the interactive macromolecular structure validation tool *MolPROBITY* (available online from the Richardson Lab at Duke University at <http://kinemage.biochem.duke.edu/molprobability/>)<sup>51,52</sup> was utilized to assign the final rotamer orientations of Asn, Gln, and His side chains, and to test for any unusual side chain contacts.

In general, the structure solution and refinement procedures were similar for all eight structures reported here. The statistics of the data collection and refinement are summarized in Table 4.1. The  $F_o-F_c$  difference electron density maps shown in Figures 4.1 and 4.2 were generated using *CNS*<sup>53</sup> and  $F_c$ s were calculated using the final model but by omitting the ligand from the structure. All figures were drawn using *PyMOL* (Delano Scientific, 2002; <http://www.pymol.org>), and labels added using Adobe® Photoshop.

**4.5.1 Mn<sup>III</sup>Mb(H<sub>2</sub>O).** After molecular replacement, the *R*-factor was 30.98%. After 10 cycles of restrained refinement, the *R*-factor was 24.86% and initial electron density maps were generated. At this stage, the initial  $F_o-F_c$  difference electron density map revealed the presence of cone-shaped electron density in the distal Mn-

heme pocket. We initially tried to model this as a methanol molecule (see Results Section). This cone-shaped electron density was finally refined as a single water molecule in two disordered positions with 70% and 30% occupancies. Two conformations of the distal His64 residue were modeled into the electron density, and the occupancies refined to 70% and 30%. Solvent water molecules were added, followed by an additional 15 cycles of refinement with *B*-factors refined anisotropically, and the *R*-factor dropped to 17.9%.

**4.5.2 *Mn<sup>II</sup>Mb*.** After molecular replacement the *R*-factor was 33.09%. After 10 cycles of restrained refinement the *R*-factor dropped to 22.09% and the initial  $F_o - F_c$  difference electron density map showed the absence of electron density for any ligand in the Mn-heme distal pocket. After the addition of the water molecules and further cycles of refinement, the *R*-factor dropped to 19.4%.

**4.5.3 *Mn<sup>III</sup>Mb(MeOH)*.** At the start of refinement the *R*-factor was 28.79%. After 10 cycles of restrained refinement the *R*-factor dropped to 22.74% and initial electron density maps were generated. The  $F_o - F_c$  difference electron density map showed clear electron density for the methanol ligand in the Mn-heme distal pocket, and methanol was modeled into this density. After the addition of solvent molecules and further cycles of refinement, the *R*-factor dropped to 17.4%. The methanol ligand refined to full occupancy with thermal factors of 14.25 and 11.69 Å<sup>2</sup> for its O and C atoms, respectively.

**4.5.4 *Mn<sup>III</sup>Mb(N<sub>3</sub><sup>-</sup>)*.** After molecular replacement, the *R*-factor was 31.52%. Ten cycles of restrained refinement resulted in the lowering of the *R*-factor to 24.93%. The  $F_o - F_c$  difference electron density map showed clear density for the

azide ligand in the Mn-heme distal pocket, and azide was modeled into the density. Solvent molecules were added, and further cycles of refinement dropped the *R*-factor to 18.4%. The azide ligand refined to near-full (94%) occupancy, with thermal factors of 17.95, 20.28 and 22.17 Å<sup>2</sup> for its N1, N2, and N3 atoms, respectively.

**4.5.5 *Mn<sup>II</sup>Mb(NO)*.** At the start of refinement, the *R*-factor was 30.77%. After 10 cycles of restrained refinement, the *R*-factor dropped to 22.23%. The  $F_o-F_c$  difference electron density map showed clear density for the nitrosyl ligand in the Mn-heme distal pocket, and NO was modeled into the density. After the addition of solvent molecules and further cycles of refinement, the final *R*-factor dropped to 17.7%. The NO ligand refined to 70% occupancy. Two conformations of the distal His64 were modeled into the electron density associated with this residue, and were refined with 70% and 30% occupancies.

**4.5.6 *Mn<sup>III</sup>Mb(ONO<sup>-</sup>)*.** At the start of refinement, the *R*-factor was 32.11%. After 15 cycles of restrained refinement, the *R*-factor dropped to 24.36%. The  $F_o-F_c$  difference electron density map showed clear density for the nitrite ligand in the Mn-heme distal pocket, and nitrite was modeled into the density. After the addition of solvent molecules and further cycles of refinement, the *R*-factor dropped to 18.6%.

**4.5.7 *Co<sup>III</sup>Mb(H<sub>2</sub>O)*.** After molecular replacement, the *R*-factor was 33.50%. After 10 cycles of restrained refinement, the *R*-factor dropped to 24.38%. The  $F_o-F_c$  difference electron density map showed the presence of electron density consistent with the presence of a bound water molecule (bound to the heme cobalt atom). After the addition of solvent molecules and further cycles of refinement, the *R*-factor dropped to 19.3%.

**4.5.8  $Co^{III}Mb(ONO^-)$ .** After molecular replacement,  $R$ -factor was 30.52%. After 10 cycles of restrained refinement, the  $R$ -factor dropped to 24.49%. The  $F_o-F_c$  difference electron density map showed clear density for the nitrite ligand in the Co-heme distal pocket, and nitrite was modeled into the density. After the addition of solvent molecules and further cycles of refinement, the final  $R$ -factor dropped to 17.4%.

#### 4.6 Protein Data Bank accession numbers

Atomic coordinates and structure factor amplitudes have been deposited with the RCSB Protein Data Bank. The accession codes are listed in Table 4.1.

#### 4.7 Results

The crystal structures of the Mn- and Co-substituted myoglobin derivatives reported here display the normal protein fold expected for the native horse heart myoglobin. The differences lie with the nature of the heme axial ligand and the resulting distal pocket structure. Hence, we focus on the heme environment in these complexes. Selected structural data for all eight complexes whose structures are reported here are shown in Table 4.2.

**4.7.1  $Mn^{III}Mb(H_2O)$ .** The  $Mn^{III}$ -reconstituted myoglobin ( $Mn^{III}Mb$ ) was prepared from the reaction of  $Mn^{III}$ -protoporphyrin IX chloride and apo-Mb in solution, and its formation confirmed by UV-vis spectroscopy. The compound in solution displays a characteristic split Soret absorption at 378 and 471 nm as reported by Yonetani *et al.*<sup>19</sup> We determined the crystal structure of this complex to 1.65 Å

resolution. The Mn<sup>III</sup>-heme environment is shown in Figure 4.1a. We also show the final  $F_o-F_c$  difference electron density map, contoured at  $3\sigma$ , that reveals the presence of the axial water ligand. This axial water is best refined as a disordered molecule in two distinct positions, with 70% (coordinated) and 30% (uncoordinated) occupancies. We located two positions for the distal His64 residue, and the occupancies correlate with the two water molecule positions. The  $2F_o-F_c$  map showing the electron density associated with the two His64 conformations is shown in Figure 4.2. The distance between the N<sup>ε</sup> atoms of the two His64 conformations is 0.74 Å, with the minor conformation closer to the interior of the protein and closer to the uncoordinated water molecule.

The major disordered position of the water ligand is close to the Mn<sup>III</sup> center, with a Mn–O distance of 2.52 Å. This Mn<sup>III</sup>–O(H<sub>2</sub>O) distance is longer than those determined for the six-coordinate model compound [(TPP)Mn<sup>III</sup>(H<sub>2</sub>O)<sub>2</sub>]ClO<sub>4</sub> (2.271(2) Å)<sup>54</sup> and the five-coordinate compounds [(TPP)Mn<sup>III</sup>(H<sub>2</sub>O)]SbF<sub>6</sub> (2.145(5) Å),<sup>54</sup> [(TPP)Mn<sup>III</sup>(H<sub>2</sub>O)]OTf (2.105(4) Å),<sup>55</sup> and [(OEP)Mn<sup>III</sup>(H<sub>2</sub>O)]ClO<sub>4</sub> (2.149(3) Å).<sup>56</sup> The O-atom of the water ligand in Mn<sup>III</sup>Mb(H<sub>2</sub>O) is 2.62 Å from the N<sup>ε</sup> atom of the major conformation of the distal His64 residue, indicative of hydrogen-bonding between these moieties. In addition, the O-atom of the coordinated water ligand is tilted 15° from the normal to the heme four-nitrogen (4N) plane towards to the interior of the protein.

The minor (30%) disordered position of the distal water molecule is 3.96 Å from the Mn<sup>III</sup> center, and is 2.84 Å from the N<sup>ε</sup> atom of the corresponding minor conformation of the His64 residue; this distance between the water molecule and this

**Table 4.1.** Statistics of X-Ray Data Collection and Refinement.

	Mn <sup>III</sup> Mb(H <sub>2</sub> O)	Mn <sup>II</sup> Mb	Mn <sup>III</sup> Mb(MeOH)	Mn <sup>III</sup> Mb(N <sub>3</sub> )	Mn <sup>II</sup> Mb(NO)	Mn <sup>III</sup> Mb(ONO)	Co <sup>III</sup> Mb(H <sub>2</sub> O)	Co <sup>III</sup> Mb(ONO)
PDB code	2O58	2O5B	2O5L	2O5M	2O5Q	2O5O	2O5T	2O5S
Data collection <sup>a</sup>								
Space group	<i>P</i> 2 <sub>1</sub>	<i>P</i> 2 <sub>1</sub>	<i>P</i> 2 <sub>1</sub>	<i>P</i> 2 <sub>1</sub>	<i>P</i> 2 <sub>1</sub>	<i>P</i> 2 <sub>1</sub>	<i>P</i> 2 <sub>1</sub>	<i>P</i> 2 <sub>1</sub>
Cell Dimen.								
<i>a</i> (Å)	35.41	35.21	35.41	35.48	35.47	35.43	35.31	35.17
<i>b</i> (Å)	28.65	28.74	28.59	28.75	28.64	28.67	28.75	28.68
<i>c</i> (Å)	62.94	64.20	63.20	62.91	63.19	62.99	63.03	63.36
β (°)	106.0	105.45	105.74	105.9	105.7	105.5	106.5	106.1
Resolution (Å)	1.65	2.00	1.70	1.65	1.90	1.60	1.60	1.60
Mean <i>I</i> /σ( <i>I</i> )	15.2 (4.4)	9 (2.7)	12.5 (3.9)	17.0 (4.6)	9.0 (2.5)	14.5 (4.0)	10.1 (2.9)	20.4 (4.7)
No. Reflections								
Observed	63842	25281	58562	64306	35301	68845	64903	65732
Unique	14874	8510	13275	14301	9669	16177	15721	15758
Comp. (%)	99.6 (98.2)	98.7 (96.0)	96.8 (93.7)	95.3 (91.0)	97.8 (99.9)	98.5 (95.9)	96.2 (87.2)	96.5 (86.6)
<i>R</i> <sub>merge</sub> (%) <sup>b</sup>	5.6 (26.4)	7.6 (31.8)	6.8 (36.4)	5.1 (27.2)	9.5 (23.6)	5.3 (31.6)	7.7 (34.8)	4.4 (16.8)
Refinement								
Res. Range (Å)	19.47-1.65	20.63-2.00	21.91 – 1.70	26.75- 1.65	26.57-1.90	25.92-1.60	26.61-1.60	26.58-1.60
<i>R</i> -factor (%)	17.9	19.4	17.4	18.4	17.7	18.6	19.3	17.4
<i>R</i> <sub>free</sub> (%) <sup>c</sup>	22.3	23.9	23.3	22.1	21.8	22.4	24.8	22.5
rmsd bond dist.	0.015	0.023	0.014	0.015	0.021	0.013	0.017	0.012
rmsd angles (°)	1.57	2.05	1.53	2.29	2.49	2.26	2.47	2.28
B factor (Å <sup>2</sup> )								
Mean	17.6	32.12	18.17	16.2	22.02	16.88	21.59	15.36
rmsd main	0.82	1.15	0.86	0.81	1.05	0.81	0.85	0.77
rmsd side	2.40	3.06	2.48	2.34	2.80	2.27	2.49	2.37

<sup>a</sup> Values in parentheses correspond to the highest resolution shells for Mn<sup>III</sup>Mb(H<sub>2</sub>O) (1.71–1.65 Å), Mn<sup>II</sup>Mb (2.07–2.00), Mn<sup>III</sup>Mb(MeOH) (1.76–1.70 Å), Mn<sup>III</sup>Mb(N<sub>3</sub>-) (1.71–1.65 Å), Mn<sup>II</sup>Mb(NO) (1.97–1.90 Å), Mn<sup>III</sup>Mb(ONO) (1.66–1.60 Å), Co<sup>III</sup>Mb(H<sub>2</sub>O) (1.66–1.60 Å), and Co<sup>III</sup>Mb(ONO) (1.66–1.60 Å). <sup>b</sup> *R*<sub>merge</sub> = Σ|*I* - <*I*>|/Σ(*I*) where *I* is the individual intensity observation and <*I*> is the mean of all measurements of *I*. <sup>c</sup> *R*<sub>free</sub> is calculated using randomly selected reflections comprising 5% of the data not used throughout refinement.

**Table 4.2.** Selected Geometrical Data for the Mn- and Co-substituted Myoglobin Complexes.

Compound	M–N(por) (Å)	M–X(axial) <sup>a</sup> (Å)	M–X–Y (°)	$\alpha$ (°) <sup>b</sup>	M–N(His93)	(M)X···N(His64) <sup>c</sup> (Å)	$\Delta M^d$ (Å)
Mn <sup>III</sup> Mb(H <sub>2</sub> O)	2.04-2.08	2.52 <sup>e</sup>	–	15.3 <sup>e</sup>	2.22	2.62 <sup>e</sup>	–0.18
Mn <sup>III</sup> Mb(MeOH)	2.02-2.07	2.48	119	8.2	2.29	2.56	–0.07
Mn <sup>II</sup> Mb	2.03-2.10	–	–	–	2.27	–	–0.34
Mn <sup>II</sup> Mb(N <sub>3</sub> <sup>–</sup> )	2.04-2.06	2.37	121	8.9	2.50	2.64	–0.08
Mn <sup>II</sup> Mb(NO) <sup>f</sup>	2.06-2.11	2.53 <sup>f</sup>	130	12.5	2.20 <sup>f</sup>	2.60	–0.20 <sup>f</sup>
Mn <sup>III</sup> Mb(ONO <sup>–</sup> )	2.07-2.10	2.33	112	9.7	2.34	2.57	–0.07
Co <sup>III</sup> Mb(H <sub>2</sub> O)	2.02-2.09	2.46	–	11.7	2.15	2.54	–0.04
Co <sup>III</sup> Mb(ONO <sup>–</sup> )	2.06-2.07	2.14	105	8.8	2.02	2.71	–0.04

<sup>a</sup> Distance between the metal and the coordinating atom of the ligand in the distal pocket. <sup>b</sup> Tilt of the coordinating atom X (of the distal ligand) from the normal to the heme 4N plane. <sup>c</sup> Distance between the coordinating atom X (of the distal ligand) and the nearest N-atom of the distal His64 residue. <sup>d</sup> Apical displacement of the central metal atom from the heme 4N plane towards the distal ligand. <sup>e</sup> These data are for the component with coordinated H<sub>2</sub>O (70% occupancy). <sup>f</sup> The NO ligand refined to 70% occupancy. Hence, these data likely represent an average of the Mn<sup>II</sup>Mb (30%) and Mn<sup>II</sup>Mb(NO) (70%) components (see text). The hydrogen bonding distance to the distal His64 residue is for the major His64 component.

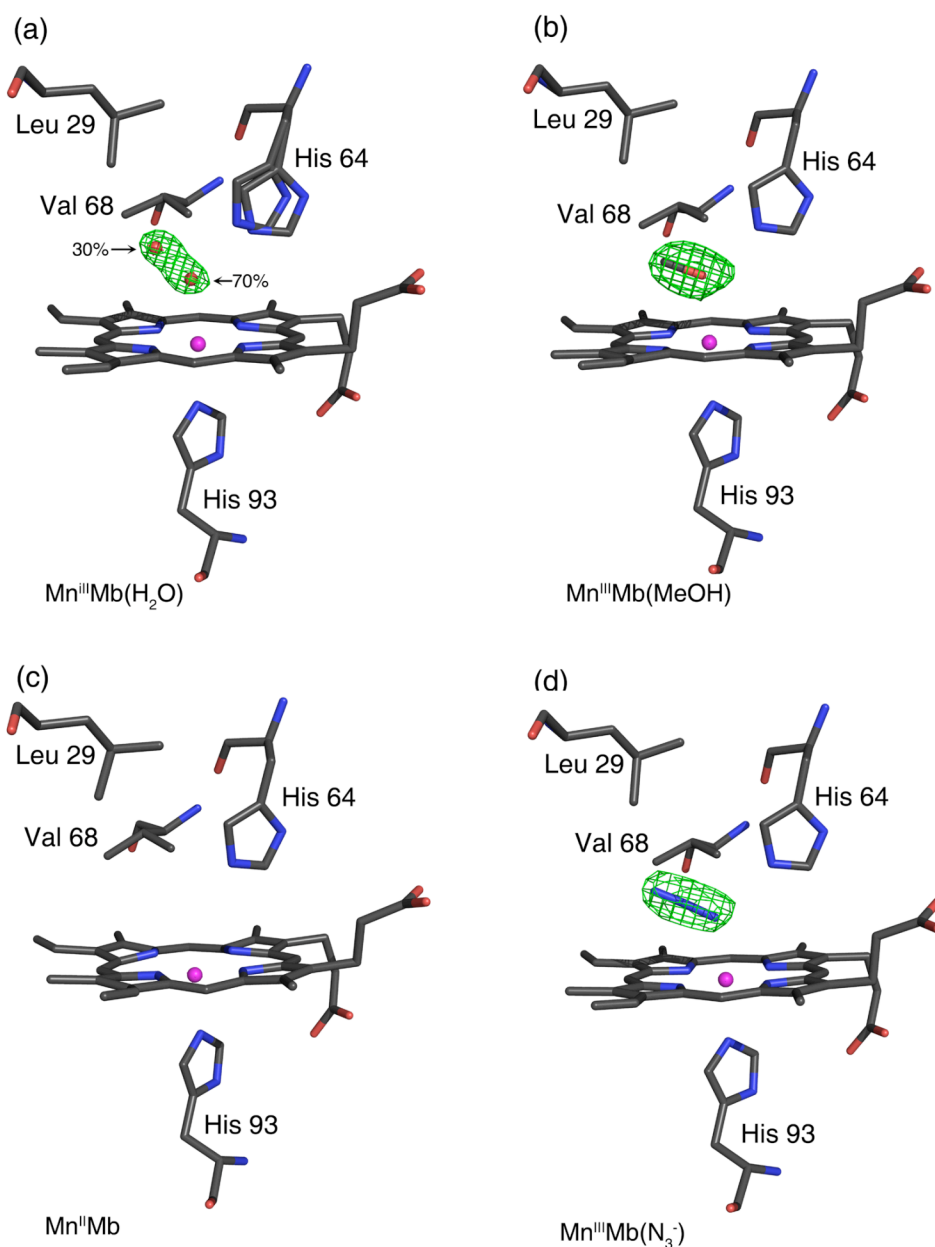


**Figure 4.1.** Final models and final  $F_o - F_c$  difference electron density maps showing side views of hh MnMb derivatives. Carbon, oxygen, nitrogen, and Mn atoms are colored grey, red, blue, and magenta, respectively. The bonds to Mn are not shown for clarity. (a)  $\text{Mn}^{\text{III}}\text{Mb}(\text{H}_2\text{O})$ : The difference electron density map contoured at 30 shows a single water molecule in two different positions. (b)  $\text{Mn}^{\text{III}}\text{Mb}(\text{MeOH})$ : The difference electron density map is contoured at  $3\sigma$ . (c) The reduced  $\text{Mn}^{\text{II}}\text{Mb}$  showing the absence of electron density for a coordinated water molecule in the active site. (d)  $\text{Mn}^{\text{III}}\text{Mb}(\text{N}_3^-)$ : The difference electron density map is contoured at  $3\sigma$ .

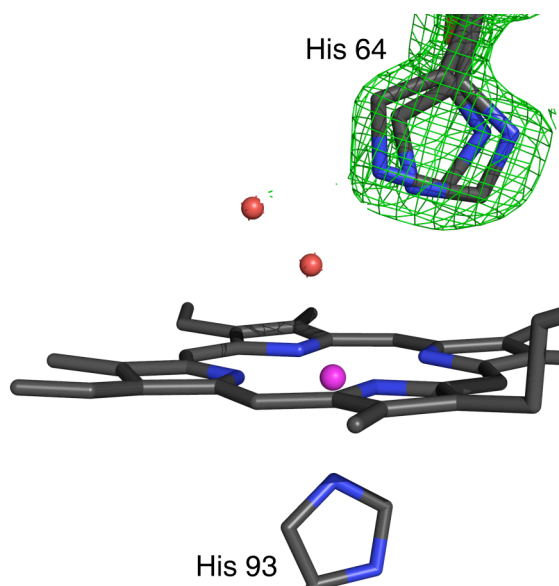


**Figure 4.2.** Final model of the Mn-heme environment in  $\text{Mn}^{\text{III}}\text{Mb}(\text{H}_2\text{O})$ , and the  $2F_o - F_c$  electron density map, contoured at  $1\sigma$ , associated with the two conformations of the distal His64 residue.

distal His64 residue is consistent with hydrogen-bond stabilization of this non-coordinated water in the distal pocket. The Leu29 and Val68 residues are the closest distal pocket moieties to this water molecule; the distance between the water O-atom and the nearest C-atoms of Leu29 and Val68 are 3.14 and 3.32 Å, respectively. The distance between the O-atom positions of the coordinated and uncoordinated water molecules is 1.70 Å.

We attempted to refine the Mn atom at two positions to correlate with the presence of coordinated and uncoordinated water, but we were not successful. Thus, it is likely that the Mn atom position represents an average between two close-by positions. In the final refined structure, the Mn atom is apically displaced by 0.18 Å from the heme 4N plane towards the proximal His93 residue, with a  $\text{Mn}^{\text{III}}-\text{N}(\text{His93})$

distance of 2.22 Å. The displacement of the Mn atom towards the proximal His93 residue is common feature for all the structures reported here (see Table 4.2), although variations in the extent of apical displacement are observed depending on the compound being examined.

**4.7.2 Mn<sup>III</sup>Mb(MeOH).** As part of a control experiment (see Discussion), we prepared the methanol adduct of Mn<sup>III</sup>Mb to determine the binding geometry of this ligand. The structure of the Mn<sup>III</sup>-heme environment is shown in Figure 4.1b. The Mn–O(MeOH) bond length is 2.48 Å, which is longer than the analogous Mn–O distance in the *d<sup>4</sup>* high-spin model non-protein complexes (TPP)Mn<sup>III</sup>(N<sub>3</sub>)(MeOH) (2.329(7) Å),<sup>57</sup> [(TPP)Mn<sup>III</sup>(MeOH)<sub>2</sub>]ClO<sub>4</sub> (2.252(2), 2.270(2) Å),<sup>58</sup> and for the five-coordinate [(OEP)Mn(EtOH)]ClO<sub>4</sub> (2.145(2) Å).<sup>59</sup>

The major differences between the structure of Mn<sup>III</sup>Mb(MeOH) and Mn<sup>III</sup>Mb(H<sub>2</sub>O) are (i) only one position of MeOH was found, at full occupancy, (ii) only one His64 conformation was found in Mn<sup>III</sup>Mb(MeOH), and (iii) the Mn<sup>III</sup> atom was displaced only 0.07 Å from the heme 4N plane towards the proximal His93 residue. The methyl group of the MeOH ligand is oriented towards the interior of the protein in the direction of the Leu29 and Ile107 amino acid residues; the distance between the C-atom of the MeOH ligand and the nearest carbon atom of the closest residue Val68 is 3.51 Å. The Mn<sup>III</sup>–O–C(Me) angle is 119°, and the distance between the O-atom of the MeOH ligand and the N<sup>ε</sup> atom of the distal His64 is 2.56 Å, indicative of a hydrogen-bonding interaction. This Mn<sup>III</sup>–O–C(Me) angle is more acute than that observed in the model compound [(TPP)Mn<sup>III</sup>(MeOH)<sub>2</sub>]ClO<sub>4</sub> (124.6(3), 124.0(3)°),<sup>58</sup> perhaps due to the presence of the hydrogen-bonding

interaction present in  $\text{Mn}^{\text{III}}\text{Mb}(\text{MeOH})$  which might also be responsible for the slightly longer Mn-O bond in the protein.

**4.7.3 The reduced  $\text{Mn}^{\text{II}}\text{Mb}$ .** Crystals of the reduced  $\text{Mn}^{\text{II}}\text{Mb}$  complex were prepared by soaking crystals of  $\text{Mn}^{\text{III}}\text{Mb}$  in buffer containing dithionite. The structure of the Mn-heme environment in the resulting  $\text{Mn}^{\text{II}}\text{Mb}$  is shown in Figure 4.1c. The absence of electron density in the  $F_o-F_c$  map was consistent with the absence of an axial water ligand in the distal pocket. Notable features of this structure include (i) a 0.34 Å apical displacement of the Mn atom from the heme 4N plane towards the proximal His93 residue in this five-coordinate compound, with a  $\text{Mn}^{\text{II}}-\text{N}(\text{His93})$  distance of 2.27 Å. This is a larger apical displacement of the Mn atom than that observed for the six-coordinate  $\text{Mn}^{\text{III}}\text{Mb}(\text{H}_2\text{O})$  compound (0.18 Å). The  $\text{Mn}^{\text{II}}-\text{N}(\text{His93})$  distance is, however, similar to that in the oxidized  $\text{Mn}^{\text{III}}\text{Mb}(\text{H}_2\text{O})$  analogue (i.e., only a 0.05 Å difference).

The structure of the heme environment of  $\text{Mn}^{\text{II}}\text{Mb}$  reported here has some similarities with the structure of the model five-coordinate compound  $(\text{TPP})\text{Mn}^{\text{II}}(1\text{-MeIm})$ .<sup>60</sup> Both  $\text{Mn}^{\text{II}}\text{Mb}$  and  $(\text{TPP})\text{Mn}^{\text{II}}(1\text{-MeIm})$  have a vacant sixth coordination site, with the  $\text{Mn}^{\text{II}}$  centers displaced from the porphyrin 4N planes towards the imidazole groups. In the model compound  $(\text{TPP})\text{Mn}^{\text{II}}(1\text{-MeIm})$ , the axial Mn–N(MeIm) bond length is 2.192(2) Å, with the Mn atom apically displaced by 0.51 Å from the four-nitrogen plane of the porphyrin towards the imidazole ligand.<sup>60</sup> Thus, the Mn–N(imidazole) bond length is ~0.08 Å longer in  $\text{Mn}^{\text{II}}\text{Mb}$  compared with the related distance in the model complex, but the apical displacements of the Mn atom towards the proximal imidazole (His93) ligands are similar.

**4.7.4  $Mn^{III}Mb(N_3^-)$ .** Figure 4.1d shows the  $Mn^{III}$ -heme environment of the 1.65 Å resolution structure of  $Mn^{III}Mb(N_3^-)$ . The azide ligand is coordinated to the  $Mn^{III}$  center with a Mn–N(azide) distance of 2.33 Å. This distance is longer than that observed in the model complexes (TPP) $Mn^{III}(N_3^-)(MeOH)$  (2.176(9) Å),<sup>57</sup> (TPP) $Mn^{III}(N_3^-)$  (2.045 Å),<sup>61</sup> and (Schiff base) $Mn^{III}(N_3^-)$  (2.221(4) Å).<sup>62</sup>

The azide ligand in  $Mn^{III}Mb(N_3^-)$  is oriented towards the interior of the protein, with a Mn–N–N(azide) angle of 121° and a tilt of 8.9° of the coordinating N-atom from the normal to the Mn-heme 4N plane. The coordinating atom of the azide ligand is 2.64 Å away from the N<sup>ε</sup> atom of the distal His64 residue, indicative of a hydrogen-bonding stabilization of the azide ligand in the distal pocket. The next closest nonbonding distance between the azide ligand and distal pocket residues is that between the terminal N3 atom of the azide with the side-chain of Leu29, with an (azide)N-to-Leu(C-atom) distance of 3.46 Å. Related distances between the azide terminal N-atom and distal pocket residues are with Ile107 (3.70 Å) and Val68 (3.74 Å). The Mn atom is apically displaced by 0.08 Å from the Mn-heme 4N plane towards the proximal His93 residue, with a Mn–N(His93) distance of 2.37 Å.

**4.7.5  $Mn^{II}Mb(NO)$ .** The interaction of NO with reduced  $Mn^{II}Mb$  in solution results in a blue shift of the Soret absorption band of  $Mn^{II}Mb$  at 442 nm to 429 nm (with  $\beta$  and  $\alpha$  bands at 544 and 583 nm, respectively) indicative of the formation of  $Mn^{II}Mb(NO)$ .<sup>32</sup> Related absorption bands at (i) 424, 538 and 580 nm<sup>34</sup> and (ii) 433, 538 and 580 nm<sup>23,32</sup> have been reported for  $Mn^{II}Mb(NO)$ . For convenience, we will use this oxidation state formalism to describe the adduct between NO and  $Mn^{II}Mb$

(i.e., to distinguish it from the adduct between NO and Mn<sup>III</sup>Mb). We discuss the oxidation state formalism later in the Discussion.

We were not able to obtain, from solution, crystals of the preformed Mn<sup>II</sup>Mb(NO) complex. Fortunately, soaking crystals of Mn<sup>II</sup>Mb (obtained by reacting crystals of Mn<sup>III</sup>Mb with dithionite) with NO also produced the desired nitrosyl product. We determined the 1.9 Å resolution structure of this product, with the NO ligand refining to 70% occupancy. We also located two conformations of the distal His64 residue that refined to 70% and 30% occupancies, with the major conformation assigned to Mn<sup>II</sup>Mb(NO), and the minor conformation assigned to Mn<sup>II</sup>Mb. Figure 4.3a shows the Mn-heme environment of the crystalline Mn<sup>II</sup>Mb(NO) product.

The Mn-NO moiety is distinctly bent with a Mn–N–O angle of 130°. The nitrosyl N-atom is tilted by 12° from the normal to the Mn-heme 4N plane, and the NO group is oriented away from the distal His64 residue in the direction of Leu29. The nitrosyl N and O atoms are, respectively, 2.60 and 3.28 Å from the N<sup>ε</sup> atom of the major conformation of the distal His64 residue, consistent with hydrogen-bonding stabilization of the NO group in the distal pocket. The next closest distance between the NO group and the distal pocket residues is with a carbon atom of Val68 (3.37 Å from the nitrosyl O-atom).

In the structure of this Mn<sup>II</sup>Mb(NO) complex, the NO ligand refined to 70% occupancy. The apical displacement of Mn by 0.20 Å from the Mn-heme 4N plane towards the proximal His93 residue suggests that the structure shown in Figure 4.3a is likely a mixture of Mn<sup>II</sup>Mb(NO) and Mn<sup>II</sup>Mb (note that ΔMn for Mn<sup>II</sup>Mb is 0.34 Å). We were not able to refine the two separate Mn positions, and the rather long

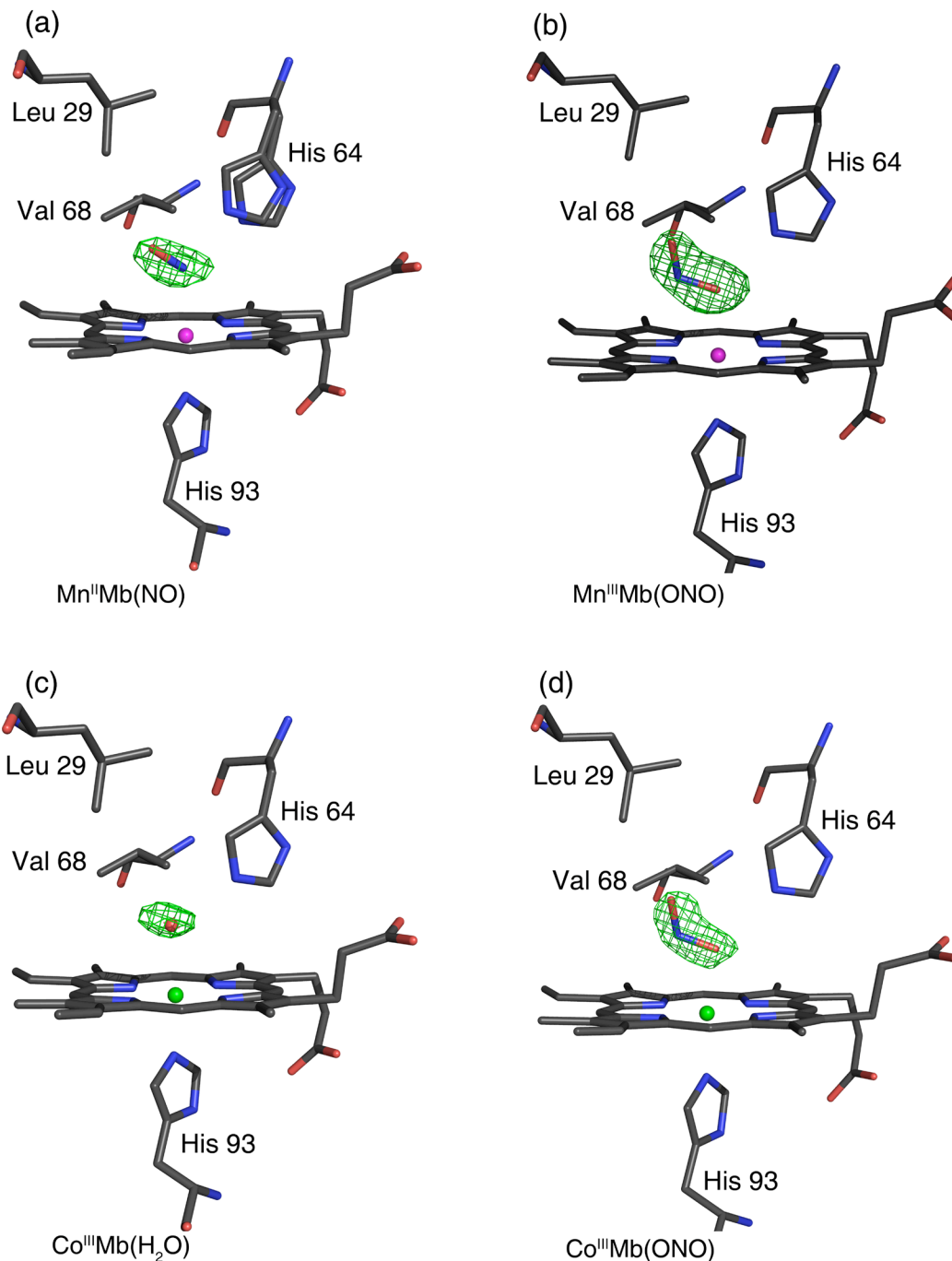


**Figure 4.3.** Final models and final  $F_o - F_c$  difference electron density maps showing side views of hh MnMb and CoMb derivatives. Carbon, oxygen, nitrogen, Mn, and Co atoms are colored grey, red, blue, magenta, and green, respectively. The bonds to Mn and Co are not shown for clarity. (a)  $\text{Mn}^{\text{II}}\text{Mb}(\text{NO})$ : The difference electron density map contoured at  $3\sigma$  shows an NO molecule that refined to 70% occupancy. (b)  $\text{Mn}^{\text{III}}\text{Mb}(\text{ONO})$ : The difference electron density map is contoured at  $2.5\sigma$ . (c)  $\text{Co}^{\text{III}}\text{Mb}(\text{H}_2\text{O})$ : The difference electron density map is contoured at  $2.5\sigma$ . (d)  $\text{Co}^{\text{III}}\text{Mb}(\text{ONO})$ : The difference electron density map is contoured at  $2.5\sigma$ .

Mn–N(O) distance of 2.53 Å may thus not correctly represent this bond length. For comparison, the Mn–N(O) bond length in the model compound (TPP)Mn(NO)(1-MeIm) is 1.641(1) Å.<sup>39</sup>

**4.7.6 Mn<sup>III</sup>Mb(ONO<sup>-</sup>).** We were not able to crystallize this complex from the addition of nitrite to Mn<sup>III</sup>Mb(H<sub>2</sub>O); either by co-crystallization or by soaking of the Mn<sup>III</sup>Mb(H<sub>2</sub>O) crystals with nitrite. Further, we did not observe any spectral change in the Soret region of the UV-vis spectrum upon addition of nitrite to a solution of Mn<sup>III</sup>Mb(H<sub>2</sub>O), consistent with the results from a previous study by Lan *et al.*<sup>34</sup> However, addition of nitrite to reduced Mn<sup>II</sup>Mb results in a spectral shift in the UV-vis spectrum from 442 nm to a new “split” Soret peak at 471 and 378 nm indicative of the formation of a new Mn<sup>III</sup>Mb species. Indeed, we were successful in obtaining crystals of Mn<sup>III</sup>Mb(ONO<sup>-</sup>) by this method, by adding nitrite to crystals of reduced Mn<sup>II</sup>Mb.

As demonstrated in Figure 4.3b, the nitrito (i.e., O-bonded) mode of coordination of the nitrite ligand is present in the Mn<sup>III</sup>Mb(ONO) complex. The conformation of the Mn–O–N–O moiety is *trans*. The Mn–O(nitrite) bond length is 2.33 Å, and the coordinating O-atom of the nitrite ligand is tilted 10° from the normal to the Mn-heme 4N plane. The Mn–O–N and O–N–O angles are 112° and 119°, respectively. The coordinating atom of the nitrite ligand is 2.57 Å from the N<sup>ε</sup> atom of the distal His64 residue, indicative of a strong hydrogen-bonding interaction. Further, the nitrite N-atom is 3.3 Å from the His64 N<sup>ε</sup> atom and the Val68 (nearest C-atom) residues. The terminal O-atom of the nitrite is 3.26 Å from the His64 N<sup>ε</sup> atom, but is only 3.07 Å from the Leu29 (nearest C-atom) residue. The bond length

between the Mn atom and the proximal His93 residue is 2.37 Å, and the Mn atom is displaced by 0.07 Å from the Mn-heme 4N plane towards His93.

**4.7.7  $\text{Co}^{\text{III}}\text{Mb}(\text{H}_2\text{O})$ .** The Co-heme environment in the crystal structure of  $\text{Co}^{\text{III}}\text{Mb}(\text{H}_2\text{O})$  is shown in Figure 4.3c. In this six-coordinate complex, the Co–O(water) distance is 2.46 Å, and the distance between the O-atom (of the coordinated water) and the  $\text{N}^\epsilon$  atom of His64 is 2.54 Å. The O-atom of the water ligand is tilted 12° from the normal to the Co-heme 4N plane towards the interior of the protein. The Co atom is displaced 0.04 Å from the heme plane towards the proximal His93 residue, with a Co–N(His93) distance of 2.15 Å. We note that the 1.65 Å resolution structure for sperm whale  $\text{Co}^{\text{III}}\text{Mb}(\text{H}_2\text{O})$ , (Co–O = 2.19 Å; Co–N(His93) = 2.06 Å; (Co)O···N(His64) = 2.87 Å) has been reported previously.<sup>63</sup> The superposition of the heme environments of horse heart (this work) and sperm whale  $\text{Co}^{\text{III}}\text{Mb}(\text{H}_2\text{O})$  is shown in Figure 4.4.

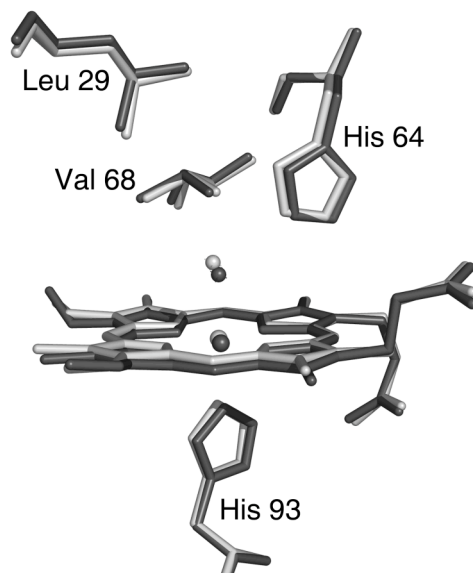


**Figure 4.4.** A superposition of the heme environments in the crystal structures of hh  $\text{Co}^{\text{III}}\text{Mb}(\text{H}_2\text{O})$  (this work, shown in light grey) and sw  $\text{Co}^{\text{III}}\text{Mb}(\text{H}_2\text{O})$  (pdb code 1YOH,<sup>63</sup> shown in dark grey) using a global  $C_\alpha$  structural alignment.

**4.7.8  $\text{Co}^{\text{III}}\text{Mb}(\text{ONO}^-)$ .** Addition of excess nitrite to a solution of  $\text{Co}^{\text{III}}\text{Mb}(\text{H}_2\text{O})$  results in a 6 nm shift of  $\lambda_{\text{max}}$  from 425 nm to 431 nm. This shift is not immediately noticeable (e.g, even after 1 min), but is clearly evident several minutes after mixing of the nitrite and  $\text{Co}^{\text{III}}\text{Mb}(\text{H}_2\text{O})$  solutions. This 6 nm red-shift is larger than the 3 nm red-shift observed in the reaction of nitrite ion with native *aquometMb* ( $\lambda_{\text{max}}$  409 nm) to form  $\text{Mb}(\text{ONO})$  ( $\lambda_{\text{max}}$  412 nm).<sup>50,64</sup>

Co-crystallization of  $\text{Co}^{\text{III}}\text{Mb}(\text{H}_2\text{O})$  in the presence of excess sodium nitrite gives crystals of the desired complex with full occupancy of the nitrite ion ligand as determined by crystallography. Soaking crystals of  $\text{Co}^{\text{III}}\text{Mb}(\text{H}_2\text{O})$  in a solution containing a high concentration of nitrite for at least 30 min gives the same  $\text{Co}^{\text{III}}\text{Mb}(\text{ONO})$  product, but with only ~60% occupancy of the nitrite ligand.

The Co-heme environment of the  $\text{Co}^{\text{III}}\text{Mb}(\text{ONO})$  complex obtained from the co-crystallization experiment (with full occupancy of the nitrite ligand) is shown in Figure 4.3d. As with the  $\text{Mn}^{\text{III}}\text{Mb}(\text{ONO})$  complex described earlier (Figure 4.3b), the nitrite ligand displays the nitrito (O-bound) coordination mode with respect to the metal center, and the Co–O–N–O moiety is in a *trans* conformation. The axial Co–O(nitrite) distance is 2.14 Å, and the Co–O–N(nitrite) and O–N–O angles are 105° and 117°, respectively. The coordinating atom of the nitrite ligand is within hydrogen-bonding distance to the  $\text{N}^\epsilon$  atom of the distal His64 residue (at a distance of 2.71 Å), and is tilted by 9° from the normal to the Co-heme 4N plane. The terminal O-atom of the nitrite ligand is situated 3.32 Å from the  $\text{N}^\epsilon$  atom of the distal His64 residue, and is 3.09 and 3.27 Å from the distal Leu29 and Val68 residues, respectively.

The nitrite (Co)O1–N and N–O2 bond lengths are 1.29 and 1.30 Å, respectively; these are identical within the limitation of this 1.60 Å resolution structure. The Co atom is 0.04 Å out of the heme plane towards the proximal histidine with a Co–N(His 93) of 2.02 Å, and the axial (His93)N–Co–O1 bond angle is 172°.

#### 4.8 Discussion

The preparation and ligand binding properties of Mn-substituted Mb have been studied in detail by spectroscopic methods. Both Mn<sup>III</sup>Mb and Mn<sup>II</sup>Mb are high-spin species.<sup>6,9,46,65</sup> In this chapter, we report the high-resolution crystal structures of the as-isolated Mn<sup>III</sup>Mb, its reduced product, and the methanol, azide, nitrosyl, and nitrite derivatives. In addition, we report the crystal structures of Co-substituted hh Mb and its nitrite adduct.

The overall structure of Mn-substituted horse heart Mb is very similar to that of the iron-containing analogue, and the protein retains the typical Mb fold. Maurus *et al.* compared the crystal structures of natural and recombinant wild-type horse heart myoglobin, and showed that small differences existed in the structures.<sup>66</sup> When the final Mn<sup>III</sup>Mb model is superimposed on the 1.7 Å resolution crystal structure of recombinant horse heart Mb reported by Maurus *et al.* (pdb access code 1WLA),<sup>66</sup> the root-mean square deviations in the backbone and side-chain atomic positions are 0.32 Å and 1.01 Å, respectively. When compared with the structure of natural Mb (pdb access code 1YMB),<sup>67</sup> these values are 0.32 and 1.12 Å, respectively. We find that the structures of the heme environments in our Mn-substituted horse heart myoglobins

more closely match those of the recombinant iron analogues, particularly with the Leu29 and Val68 side-chain orientations. The superposition of the heme environment structures of Mn<sup>III</sup>Mb(H<sub>2</sub>O) and the two *aquomet*Mb structures are shown in Figure 4.5. It is interesting to note that Atassi reported earlier that Mn<sup>III</sup>Mb and wild-type Mb exhibit identical immunological properties.<sup>10</sup> In this chapter, we focus on the Mn-heme active sites and their immediate environments.

#### ***4.8.1 The Nature of the Heme Site in Mn<sup>III</sup>-Substituted Myoglobin.***

Manganese-substituted myoglobin (MnMb) has been prepared and studied in solution for decades. However, the coordination environment around the metal center in MnMb derivatives has been a subject of considerable debate. Mn<sup>III</sup>Mb displays a characteristic “split” Soret band pattern at  $\lambda_{\text{max}}$  378 and 471 nm, whereas Mn<sup>II</sup>Mb displays a single Soret peak at  $\lambda_{\text{max}}$  438 nm.<sup>6,19,46</sup> Mitra and coworkers used multinuclear NMR and optical spectroscopy to determine that the sixth axial position in Mn<sup>III</sup>Mb was unlikely to be occupied by a water molecule.<sup>29</sup> In the latter study, they did not observe a change in the optical spectrum of Mb<sup>III</sup>Mb in the pH 4–11 range, suggesting the absence of an aquo $\leftrightarrow$ hydroxo equilibrium for a hypothetical axial water ligand. This result differed somewhat from that reported by Spiro and coworkers who studied the resonance Raman spectra of Mn<sup>III</sup>Mb and found evidence for a weakly interacting axial water ligand in the sixth position.<sup>23</sup> As stated in the Introduction, there is a noticeable paucity of crystal structures of Mn-substituted

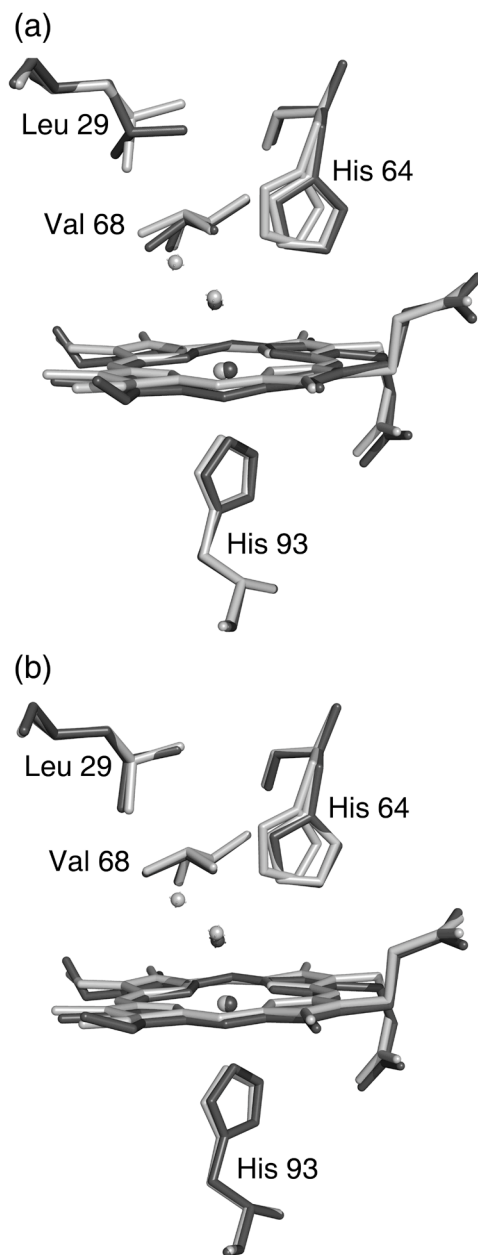


**Figure 4.5.** A superposition of the heme environments in the crystal structures of hh Mn<sup>III</sup>Mb(H<sub>2</sub>O) (this work, shown in light grey) and (a) natural hh Fe<sup>III</sup>Mb(H<sub>2</sub>O) (pdb code 1YMB,<sup>67</sup> shown in dark grey), and (b) recombinant hh Fe<sup>III</sup>Mb(H<sub>2</sub>O) (pdb code 1WLA,<sup>66</sup> shown in dark grey), using a global C<sub>α</sub> structural alignment. The major conformation of His64 in hh Mn<sup>III</sup>Mb(H<sub>2</sub>O) is similar to the conformation in Fe<sup>III</sup>Mb(H<sub>2</sub>O). The Leu29 and Val68 conformations of the Mn- and Fe-proteins overlay better in the structures shown in Figure 4.5b.

heme proteins in the literature. Using X-ray difference Fourier techniques, Moffat and coworkers determined that for Mn<sup>III</sup>Hb, the  $\alpha$  hemes contained six-coordinate Mn<sup>III</sup> centers (with axial water) whereas the  $\beta$  hemes were five-coordinate (i.e., no axial water).<sup>24</sup>

Farmer and coworkers investigated the electrochemical properties of Mn<sup>III</sup>Mb in dimethyldidodecylammonium bromide surfactant films.<sup>68</sup> They discovered a dynamic exchange between two Mn<sup>III</sup>/Mn<sup>II</sup> redox couples ( $E_1 = -0.25$  V vs SCE;  $E_2 = -0.41$  V vs SCE), and they attributed this to the presence of two forms of Mn<sup>III</sup>Mb that probably differed in heme site geometry. Interestingly, Hoffman and Gibson reported that Mn<sup>III</sup>Mb reacted with azide in two kinetically separable steps, and that this was likely due to the presence of two forms of the Mn-porphyrin that differed in the extent of metal displacement from the porphyrin plane.<sup>26</sup>

The crystal structure of Mn<sup>III</sup>Mb(H<sub>2</sub>O) reported here sheds new light on this debate regarding the axial coordination geometry of the metal site in this protein. Three independent preparations, crystallizations, and structure solutions at 1.65 Å resolution yielded identical Mn<sup>III</sup>Mb(H<sub>2</sub>O) crystal structures. In the structure, there is a mixture of a six-coordinate species (with axial water; 70% occupancy) and a five-coordinate species (without axial water; a non-bonded water refined to 30% in the distal pocket). We also found two conformations for the distal His64 residue, and these conformations refined to the corresponding 70% and 30% occupancies (Figures 4.1a and 4.2).

During the initial stages of refinement of the structure, we were unsure if the electron density (attributed to an axial ligand) observed in the  $F_o - F_c$  difference map

was due to an adventitious solvent molecule such as methanol. To test this, we performed the following additional experiments. (i) We effected reduction of the purple-red  $\text{Mn}^{\text{III}}\text{Mb}$  crystal with dithionite, and obtained the structure of the resulting orange-red five-coordinate reduced compound  $\text{Mn}^{\text{II}}\text{Mb}$  (see later). We then reoxidized this  $\text{Mn}^{\text{II}}\text{Mb}$  crystal with ferricyanide and determined its 1.9 Å resolution structure; it was identical to that obtained for  $\text{Mn}^{\text{III}}\text{Mb}(\text{H}_2\text{O})$  as shown in Figure 4.1a. This result reaffirmed to us that the electron density in the distal pocket was not due to an adventitious exogenous ligand such as methanol. (ii) In addition, we prepared the previously unknown methanol adduct by cocrystallizing  $\text{Mn}^{\text{III}}\text{Mb}$  in the presence of methanol, and determining the structure of the resulting  $\text{Mn}^{\text{III}}\text{Mb}(\text{MeOH})$  product. The positive electron density in the  $F_o - F_c$  difference map is consistent with the presence of a methanol ligand that refined to full occupancy. Importantly, the geometry of the bound MeOH ligand in the structure of  $\text{Mn}^{\text{III}}\text{Mb}(\text{MeOH})$  (Figure 4.1b) is clearly different from that shown for  $\text{Mn}^{\text{III}}\text{Mb}(\text{H}_2\text{O})$  (Figure 4.1a).

The presence of distal-pocket uncoordinated water in the structure of  $\text{Mn}^{\text{III}}\text{Mb}(\text{H}_2\text{O})$  is, while initially unexpected, not without precedent in crystal structures of native and mutant iron myoglobins. For example, a similar distal-pocket (uncoordinated) water has been located in the 1.15 Å resolution crystal structures of wild-type ferrous *deoxyMb* (horse heart and sperm whale), and this water is stabilized by hydrogen-bonding with the distal His64 residue ( $\text{HOH} \cdots \text{N}(\text{His})$  distance of 2.8 Å).<sup>69,70</sup> In the case of hh *deoxyMb*, this distal pocket water was located 3.53(5) Å from the Fe center (*c.f.* 2.13 Å for liganded water in *aquometMb*).<sup>69</sup> Further, distal

pocket water has been observed in other reported structures of wild-type<sup>71-73</sup> and mutant (V68A,<sup>72</sup> V68F,<sup>72</sup> V68N (molecule B)<sup>74</sup>) *deoxyMb*'s.

The crystal structure of the Val68Thr mutant of pig *deoxyMb* provides an interesting comparison with the structure of hh Mn<sup>III</sup>Mb(H<sub>2</sub>O) reported here. In molecule A of the Val68Thr *deoxyMb*, a single water molecule is distributed between two positions; one position is within direct bonding distance to Fe (Fe–O = 1.9 Å; 30% occupancy of H<sub>2</sub>O), and the other is positioned 3.5 Å from the Fe (70% occupancy of H<sub>2</sub>O) yet within hydrogen-bonding distance of the distal His64 residue (HOH···N<sup>ε</sup>(His) = 2.6 Å).<sup>75</sup> In molecule B, a single position of the distal water located 3 Å from Fe is observed, and this is also within hydrogen-bonding distance to the His64 residue (HOH···N<sup>ε</sup>(His) = 2.6 Å).<sup>75</sup>

The distance between the two distal pocket water molecule positions in Mn<sup>III</sup>Mb(H<sub>2</sub>O) is 1.70 Å. This distance is inconsistent with the presence of a dioxygen ligand (*c.f.*, the O–O distance of 1.24 Å in *oxyMb*),<sup>69</sup> as are the refined occupancies of the O atoms. Further, this 1.70 Å distance is too short for a HOH···OH<sub>2</sub> hydrogen-bonding interaction, and rules out the presence of both coordinated and unligated H<sub>2</sub>O in the same molecule (such presence of coordinated and uncoordinated H<sub>2</sub>O has been observed in the 1.9 Å resolution structure of native *sw aquometMb*).<sup>71</sup>

The location of the distal pocket (uncoordinated) water molecule in Mn<sup>III</sup>Mb(H<sub>2</sub>O) is reminiscent of the distal docking site for photodissociated CO from MbCO as determined by X-ray crystallography.<sup>76-78</sup> For example, the crystal structure of photolyzed hh MbCO shows the CO ligand in a position that is 3.6 Å from the Fe

atom and atop a carbon pyrrole.<sup>76</sup> This site is in the general area as, but not the same as, the distal pocket Xe binding site (i.e., the Xe<sub>4</sub> site).<sup>79</sup>

Importantly, the displacement of the distal pocket water in *deoxyMb* has been linked to the kinetic barriers for CO binding to ferrous Mb.<sup>71,80</sup> It is thus likely that the presence of two types of distal H<sub>2</sub>O in Mn<sup>III</sup>Mb(H<sub>2</sub>O) (i.e., coordinated and uncoordinated) helps explain the presence of two Mn<sup>III</sup>/Mn<sup>II</sup> redox couples for the electrochemical reduction of Mn<sup>III</sup>Mb<sup>68</sup> and the two kinetically separable steps for the reaction of azide with Mn<sup>III</sup>Mb.<sup>26</sup> Finally, we note that Moffat and coworkers have utilized X-ray difference Fourier techniques to determine that the Mn center in the  $\alpha$ -heme of Mn<sup>III</sup>Hb binds H<sub>2</sub>O as a sixth ligand, whereas the  $\beta$ -heme does not and is five-coordinate.<sup>24</sup>

**4.8.2 The Structure of the Reduced Mn<sup>II</sup>Mb Complex.** The reduction of Mn<sup>III</sup>Mb to Mn<sup>II</sup>Mb in solution is a well-studied reaction, and the reduction can be effected using dithionite,<sup>11,46,81</sup> radiolysis,<sup>46</sup> electrochemical methods employing surfactant films,<sup>68</sup> or employing the mediator oxazine-170 perchlorate.<sup>82</sup> Hori *et al.* employed powder and single-crystal multifrequency EPR spectroscopy to determine that the metal center in Mn<sup>II</sup>Mb is high-spin  $3d^5$  ( $S = 5/2$ )<sup>65</sup> and this is consistent with a singly-occupied strongly antibonding  $d_{x^2-y^2}$  orbital.<sup>6</sup>

Arnone and coworkers reported the 3.0 Å resolution crystal structure of the metallohybrid hemoglobin Hb( $\alpha$ -Fe<sup>II</sup>CO)( $\beta$ -Mn<sup>II</sup>) that crystallizes in the *deoxyHb* T-state.<sup>83</sup> They determined that the  $\beta$ -Mn<sup>II</sup> subunit is structurally isomorphous with the normal *deoxy*  $\beta$ -Fe subunit.

The crystal structure of Mn<sup>II</sup>Mb reported here reveals that the distal pocket water molecules are displaced upon dithionite reduction of Mn<sup>III</sup>Mb(H<sub>2</sub>O). Thus, unlike the case of Mn<sup>III</sup>Mb(H<sub>2</sub>O), no water molecules were located in the vicinity of the Mn<sup>II</sup> center. This contrasts with several reported crystal structures of iron-containing *deoxy*Mb where a non-coordinated water molecule has been located in the distal pocket.<sup>69-73,84</sup>

The apical displacement of the Mn atom in Mn<sup>II</sup>Mb ( $\Delta\text{Mn} = 0.34 \text{ \AA}$ ) from the heme 4N plane is larger than that observed for Mn<sup>III</sup>Mb(H<sub>2</sub>O) ( $\Delta\text{Mn} = 0.18 \text{ \AA}$ ). This increase in apical displacement upon reduction of the protein is similar to that seen in the high-resolution structures of reduced Mb ( $\Delta\text{Fe} = 0.363(11) \text{ \AA}$ ) vs. *aquomet*Mb ( $\Delta\text{Fe} = 0.106(7) \text{ \AA}$ ).<sup>69</sup> The heme environments of Mn<sup>III</sup>Mb(H<sub>2</sub>O) and Mn<sup>II</sup>Mb, obtained from the overlay of the protein C<sub>α</sub> backbones, are shown in Figure 4.6. Differences are evident in the water ligation and distal His64 placement in these proteins. The His64 residue in the reduced Mn<sup>II</sup>Mb more closely overlaps the minor conformation of the His64 residue in Mn<sup>III</sup>Mb(H<sub>2</sub>O). Figure 4.7 shows an overlay of the heme sites in the reduced Mn<sup>II</sup>Mb and *deoxy*Mb (Fe<sup>II</sup>Mb, Figure 4.7). In the reduced Fe<sup>II</sup>Mb case, one of the two conformations of the distal His64 residue reveals an inward movement that supposedly helps stabilize the distal pocket water molecule through hydrogen-bonding, whereas in the reduced Mn<sup>II</sup>Mb case such a hydrogen-bond stabilization is not present due to the lack of distal pocket water. A superposition of the heme environments of Mn<sup>II</sup>Mb and Fe<sup>II</sup>Mb is shown in Figure 4.7 to illustrate these His64 positions.

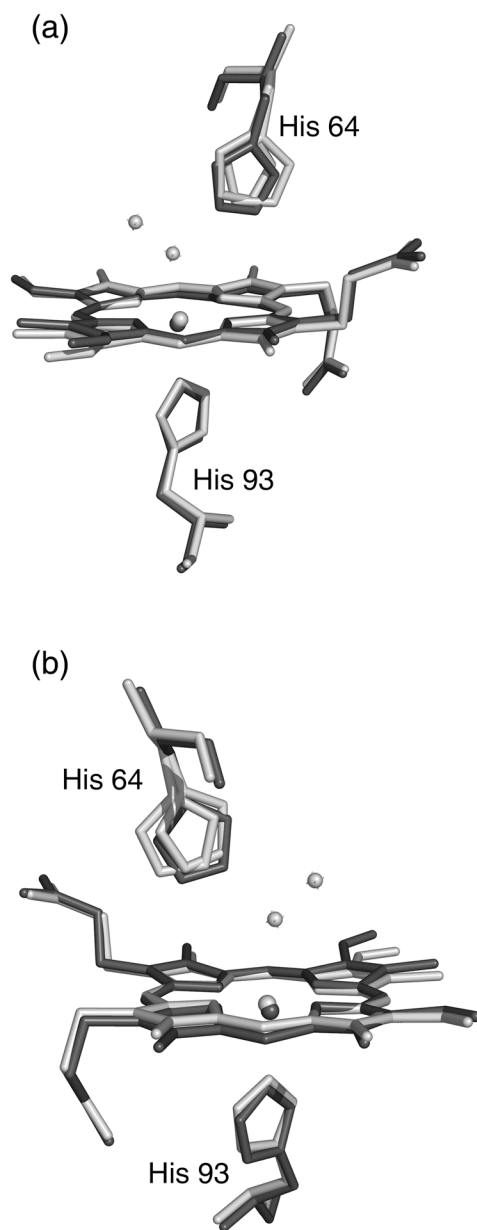


**Figure 4.6.** A superposition of the heme environments in the crystal structures of hh Mn<sup>III</sup>Mb(H<sub>2</sub>O) (this work, shown in light grey) and hh Mn<sup>II</sup>Mb (this work, shown in dark grey) using a global C<sub>α</sub> structural alignment, and shown from two different views. The N<sup>ε</sup> atoms of His64 and His93 residues of Mn<sup>II</sup>Mb are shifted from their major/minor positions in Mn<sup>III</sup>Mb(H<sub>2</sub>O) by 0.95/0.21 and 0.37 Å, respectively. Also, the Mn<sup>II</sup> center is shifted 0.25 Å from its Mn<sup>III</sup> position. A *meso* carbon and its connecting pyrrole ring A are shifted towards the proximal side in Mn<sup>II</sup>Mb relative to those in Mn<sup>III</sup>Mb(H<sub>2</sub>O).

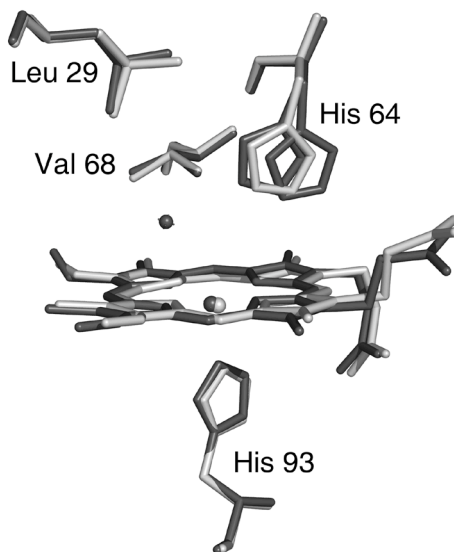


**Figure 4.7.** A superposition of the heme environments in the crystal structures of hh  $\text{Mn}^{\text{II}}\text{Mb}$  (this work, shown in light grey) and hh  $\text{Fe}^{\text{II}}\text{Mb}$  (pdb code 1A6N,<sup>69</sup> shown in dark grey) using a global  $\text{C}_\alpha$  structural alignment. The distal pocket water in hh  $\text{Fe}^{\text{II}}\text{Mb}$  is located 3.53 Å from Fe, and is 2.76 Å from the inward conformation of the distal His64 residue; the outer conformation overlaps with that of *aquometMb*

**4.8.3 The Structure of the Azide Complex.** The azide anion is a known inhibitor of cellular respiration, and it also inhibits the catalytic activities of catalase, cytochrome oxidase, and peroxidases.<sup>42</sup> The azide adduct of Mn-substituted Mb has been reported,<sup>11,81</sup> and has been characterized by optical and resonance Raman spectroscopy.<sup>22</sup> Hoffman and Gibson reported anomalous binding of azide to  $\text{Mn}^{\text{III}}\text{Mb}$ , and determined that the reaction of azide with  $\text{Mn}^{\text{III}}\text{Mb}$  proceeded in two kinetically separable steps to eventually generate  $\text{Mn}^{\text{III}}\text{Mb}(\text{N}_3^-)$ .<sup>26</sup> In contrast, azide binding to iron-containing *metMb* is consistent with a single binding equilibrium.<sup>85</sup>

The 2.8 Å resolution crystal structure of the azide complex of the iron-containing horse *metHb* is known.<sup>86,87</sup> The related crystal structure of the azide adduct of *metMb* was first reported by Stryer *et al.* in 1964.<sup>88</sup> A comparison of the crystal structures of hh Mb<sup>III</sup>(N<sub>3</sub><sup>-</sup>) (at 2.0 Å resolution) and its His64Thr mutant (at 1.8 Å resolution) was reported by Maurus *et al.* in 1998.<sup>89</sup> In the wild type adduct, the Fe–N–N(N) bond was 119°, and the Fe–N(azide) bond was 2.11 Å. In the His64Thr mutant structure, two conformations of the azide ligand were present; the major (~90%) conformation oriented the azide ligand towards the interior of the protein (as seen in the wild type structure), and the minor conformation oriented the azide ligand towards to exterior of the protein towards the solvent. The latter minor conformation is reminiscent of the 1.9 Å resolution crystal structure of the azide adduct of ferric myoglobin isolated from the buccal muscles of the Mediterranean mollusc *Aplysia limacine*, where the azide ligand is oriented towards the solvent<sup>90</sup>; this protein lacks a distal His64(E11) residue.

The crystal structure of hh Mn<sup>III</sup>Mb(N<sub>3</sub><sup>-</sup>) reported here, and shown in Figure 4.1d, is similar to that of wild type Mb<sup>III</sup>(N<sub>3</sub><sup>-</sup>),<sup>89</sup> in which only one conformation of the azide ligand was observed. In both compounds, the azide ligand is oriented towards the interior of the protein. As is the case of the iron-containing Mb<sup>III</sup>(N<sub>3</sub><sup>-</sup>), the azide ligand is oriented towards the distal Ile107 residue and in Van der Waal's contact with Leu29. The Mn atom in Mn<sup>III</sup>Mb(N<sub>3</sub><sup>-</sup>) is almost in the heme 4N plane, with an apical displacement of only 0.08 Å. The near in-plane position of Mn is consistent with the six-coordination of the metal center and near-complete (94%) occupancy of the azide ligand. The proximal Mn–N(His93) bond length in

$\text{Mn}^{\text{III}}\text{Mb}(\text{N}_3^-)$  of 2.50 Å is, however, longer than that observed in the iron-containing  $\text{Mb}^{\text{III}}(\text{N}_3^-)$  (2.06 Å), demonstrating the effect that the  $\text{Mn}^{\text{III}}$   $d^4$  center has on this axial bond length when compared with the ferric  $d^5$  center. Ferric  $\text{Mb}^{\text{III}}(\text{N}_3^-)$  has been shown to exhibit a ground-state low-spin electronic configuration and an observable low-spin/high-spin equilibrium at room temperature.<sup>85</sup> In contrast, the  $d^4$  complex  $\text{Mn}^{\text{III}}\text{Mb}(\text{N}_3^-)$  is known to be high-spin,<sup>26</sup> and this likely accounts for its longer proximal metal–N(His93) bond length.

**4.8.4 The Nitric Oxide Complex.** For convenience, the nitrosyl adduct of  $\text{Mn}^{\text{II}}\text{Mb}$  is represented as  $\text{Mn}^{\text{II}}\text{Mb}(\text{NO})$ , although it is perhaps better represented as  $\{\text{MnNO}\}^6$  (see later). In order to place the NO ligand conformation observed in  $\text{Mn}^{\text{II}}\text{Mb}(\text{NO})$  in proper context, some discussion of formalism is warranted.<sup>91,92</sup> For example, the oxidation state formalism has often been used to describe metal nitrosyl linkages. In this formalism, NO binding to a metal center (M) to generate a linear M–NO unit results in a complex formulated as  $\text{M}^-(\text{NO}^+)$ , where a formal electron transfer to the metal has occurred. Conversely, when a bent M–NO moiety is generated, the complex is formulated as  $\text{M}^+(\text{NO}^-)$ . Clearly, this formalism is overly simplistic. Although it does take into account that NO is a redox active ligand, it does not account for cases where the unpaired electron density on NO essentially still resides on the ligand in its metal complex. Enemark and Feltham developed a notation that treats the metal–NO fragment as a single unit, and the use of the resulting formalism avoids the oxidation state simplification of the metal–NO group.<sup>93-95</sup> In this  $\{\text{MNO}\}^n$  formalism,  $n$  denotes the number of assigned electrons to the metal  $d$  orbitals (without consideration of the NO ligand(s)) plus an electron for

each of the attached NO ligands. Thus, the (por)Mn(NO) complex belongs to the {MnNO}<sup>6</sup> class, and the (por)Fe(NO) belongs to the {MNO}<sup>7</sup> class. According to this formalism as applied to nitrosyl metalloporphyrins, {MNO}<sup>6</sup> compounds have preferred linear NO geometries, and {MNO}<sup>7</sup> compounds have bent (~145°) NO geometries. In synthetic six-coordinate iron nitrosyl porphyrins of the {MNO}<sup>7</sup> class, the FeNO angles are in the tight 137–140° range (avg. ~138.5°).<sup>96,97</sup> A much wider range of FeNO bond angles (112°–160°) is observed in nitrosyl heme proteins, however.<sup>50</sup> The reported 1.3 Å resolution crystal structures of hh MbNO showed that two reproducible FeNO angles (~144° and 120°) are obtained depending on the method of preparation of the complex.<sup>50</sup> The variability of FeNO angle in the heme pocket of MbNO had been demonstrated previously by Hori *et al.* using single crystal EPR spectroscopy; the FeNO angle was 153 ± 5 at 293K, but was 109 ± 5 at 77 K.<sup>98</sup> Chien and Dickenson showed, using single crystal EPR spectroscopy, that the FeNO angles in HbKNO were 167° in the α-subunits and 105° in the β-subunits.<sup>15</sup> It is thus likely that subtle distal pocket effects influence the metal-NO bond geometry in nitrosyl adducts of heme proteins. We now consider the case of Mn<sup>II</sup>Mb(NO) and compare the observed geometry to that expected from synthetic manganese nitrosyl porphyrins.

To date, all synthetic (por)Mn(NO)-containing compounds of the {MnNO}<sup>6</sup> class (i.e., Mn<sup>II</sup>NO) that have been characterized by X-ray crystallography display linear Mn-NO groups.<sup>39,40,99,100</sup> The expected and observed linearity of the MnNO bonds is supported by the spectroscopic characterization of several low-spin (por)Mn(NO)-containing compounds.<sup>35,37,92,101</sup> Yu *et al.* employed resonance Raman

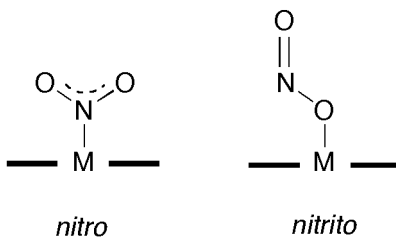
spectroscopy to demonstrate that steric constraints within the distal face of a synthetic “strapped” (por)Mn(NO) complex enhances the Mn–N–O bending mode, and they attributed this observation to a tilting of the *trans* Mn–N(*N*-base) bond.<sup>101</sup>

As stated in the Introduction, NO adducts of Mn-substituted heme proteins have been prepared and characterized by spectroscopy. Mn<sup>III</sup>Mb does not bind NO, however Mn<sup>II</sup>Mb does.<sup>32</sup> Interestingly, Gersonde and coworkers demonstrated, using resonance Raman spectroscopy, that the monomeric Mn<sup>III</sup>Hb compound from the insect *Chironomus thummi thummi* binds NO to give the Mn<sup>III</sup>NO adduct, but this undergoes autoreduction to the Mn<sup>II</sup>NO derivative.<sup>33</sup>

To the best of our knowledge, the crystal structure of Mn<sup>II</sup>Mb(NO) reported in this work (Figure 4.3a) represents the first distinctly bent MnNO moiety in a natural or synthetic manganese heme complex. The NO ligand refines to 70% occupancy, but the MnNO bend is clearly evident in the structure. The nitrosyl N atom is 2.6 Å away from the N<sup>ε</sup> atom of the major conformation of the distal His64 residue, suggesting strong hydrogen-bond stabilization of the NO molecule in the distal pocket. As mentioned in the Results section, the observed long Mn–NO distance of 2.53 Å is likely an average distance that has contributions from the unligated five-coordinate Mn<sup>II</sup>Mb complex and the nitrosyl adduct. Assuming that the Mn atom were in the heme 4N plane in Mn<sup>II</sup>Mb(NO), the resulting Mn–NO distance would still be rather long. Thus, we propose that the geometry of the MnNO moiety observed here represents that of a loosely bound NO molecule to the metal center that is held in place by strong hydrogen-bonding to the distal His64 residue. This geometry is also likely determined by the method of preparation of the complex, namely the

nitrosylation of the *performed* distal pocket in the Mn<sup>II</sup>Mb crystals. Such a procedure may disfavor linear (strong) binding of the NO ligand without significant movement of the distal His64 residue away from its position in Mn<sup>II</sup>Mb. We are continuing attempts to crystallize pre-formed Mn<sup>II</sup>Mb(NO) to test this hypothesis.

**4.8.5 The Nitrite Complex of Mn<sup>III</sup>Mb and Co<sup>III</sup>Mb.** There is renewed interest in the nature of binding of the nitrite anion to heme proteins.<sup>43,102</sup> It has long been appreciated that the heme-nitrite interaction is an essential one insofar as nitrite reduction by the heme-containing nitrite reductases (NiRs) is concerned. Nitrite is reduced to NO by the NiRs<sup>103-105</sup> and this process is believed to involve initial binding of nitrite directly to the iron center in the heme-containing NiRs. Crystal structures of the nitrite adducts of cytochrome *cd* 1 NiR from *P. Pantotrophus* reveals the N-binding (i.e., nitro) mode of nitrite to the iron center.<sup>106</sup>



Although this nitrite adduct was obtained by soaking crystals of ferrous NiR with nitrite, it is reasonable to assume that such an N-binding mode would facilitate protonation of a nitrite terminal O-atom to result in eventual release of NO and a water molecule. The crystal structure of the nitrite adduct of *ferric* cytochrome *c* NiR from *Wolinella succinogenes* also shows N-binding of the nitrite anion to the iron center, and density functional calculations on the related model compound (por)Fe<sup>III</sup>(NH<sub>3</sub>)(NO<sub>2</sub>) reveals that the N-binding mode is more stable than the nitrito O-binding mode by >10 kcal/mol.<sup>107</sup> The crystal structure of the nitrite adduct of the

sulfite reductase hemoprotein from *E. coli* similarly reveals an N-binding mode of the nitrite anion to the iron center.<sup>108</sup>

Interestingly, DFT calculations on the nitrite adduct of cytochrome *cd<sub>1</sub>* NiR provide intriguing possibilities for nitrite coordination to the heme center in this enzyme.<sup>109</sup> Although the nitrito O-binding mode was determined to be 4.5 kcal/mol higher in energy than the corresponding nitro N-binding mode in the ferric form (6 kcal/mol in the ferrous form), the nitrito form was considered to also be a viable intermediate in NiR catalysis.

The nitro N-binding mode has been determined for all crystallographically characterized synthetic iron porphyrins containing the nitrite ligand, regardless of whether the iron center is formally in the ferric or ferrous state.<sup>96</sup> The only exception to this is that for the nitrite in the anionic complex [(T<sub>piv</sub>PP)Fe(NO)(NO<sub>2</sub>)]<sup>-</sup> which displays both N-binding (nitro) and O-binding (nitrito) of the disordered nitrite group.<sup>110</sup> Results of DFT calculations on a model iron porphyrin with NO and nitrite ligands show that the nitrito linkage isomer (porphine)Fe(NO)(ONO) is only 4.3 kcal/mol higher in energy than the related nitro isomer (porphine)Fe(NO)(NO<sub>2</sub>).<sup>111</sup>

Our group reported the 1.3 Å resolution X-ray crystal structure of the nitrite adduct of ferric horse heart Mb and showed that the nitrite anion was bound to the ferric center via the nitrito O-binding mode.<sup>50</sup> Importantly, this structure was the first to demonstrate *that a stable O-binding mode of nitrite is possible in heme proteins*. Given this rather unexpected nitrito binding mode for the nitrite ligand in the iron-containing *d<sup>5</sup>* compound Mb<sup>III</sup>(ONO<sup>-</sup>) and the role of the distal pocket in stabilizing

this (to date) unusual binding mode, we sought to investigate the nitrite binding preferences within the distal pockets of the  $d^4$  Mn<sup>III</sup> and  $d^6$  Co<sup>III</sup> analogues.

To the best of our knowledge, there is only one report of a crystal structure of a synthetic manganese porphyrin containing nitrite, namely that of (TPP)Mn<sup>III</sup>(ONO).<sup>112</sup> This compound clearly reveals a nitrito O-binding mode of the nitrite anion. Interestingly, although continuous photolysis of this compound shows the formation of (TPP)Mn(O) and NO,<sup>112,113</sup> flash photolysis studies on this compound reveal dissociation of NO<sub>2</sub> from the metal center.<sup>114</sup> Recombination of NO<sub>2</sub> with the (TPP)Mn<sup>II</sup> photoproduct then proceeds via a nitro (TPP)Mn(NO<sub>2</sub>) intermediate that isomerizes to the more stable (TPP)Mn(ONO) compound.<sup>114</sup> Not surprisingly, therefore, the crystal structure of Mn<sup>III</sup>Mb(ONO<sup>-</sup>) also shows that the nitrite anion binds to the manganese center via the nitrito O-binding mode (Figure 4.3b).

The situation for cobalt was not expected, however. To date, all crystallographically characterized nitrite adducts of synthetic cobalt porphyrins demonstrate that the nitrite anion is bound to the cobalt centers via the nitro N-binding mode.<sup>115-118</sup> To the best of our knowledge, there is no exception to this observation for model cobalt porphyrin compounds. Indeed, it was demonstrated that during the recombination of NO<sub>2</sub> with (TPP)Co<sup>II</sup> (generated from flash photolysis of (TPP)Co<sup>III</sup>(NO<sub>2</sub>)), an intermediate forms which decays to (TPP)Co<sup>III</sup>(NO<sub>2</sub>); the intermediate was assigned as the nitrito linkage isomer (TPP)Co<sup>III</sup>(ONO).<sup>119</sup>

To the best of our knowledge, no nitrite adducts of cobalt-substituted heme proteins or related cobalt biomolecules have been characterized. Thus, the structure of Co<sup>III</sup>Mb(ONO<sup>-</sup>) represents the first report of a cobalt nitrite heme protein, and is

the first stable nitrito binding to cobalt porphyrins to be established. Clearly, it is evident that although information from crystal structures of cobalt nitrite compounds of model porphyrins have helped in understanding the mechanisms of action of these compounds as catalysts for chemical transformation such as O-atom transfers in oxidation reactions (generating (por)Co(NO) intermediates),<sup>118</sup> the structures may not correlate very well with the geometries present in cobalt-substituted heme proteins. The ability of the distal pocket in Co<sup>III</sup>Mb to effect the nitrito O-binding preference is significant, and suggests that the hydrogen-bonding provided by the distal His64 residue is primary in stabilizing this binding mode. Since such a moderate to strong hydrogen bonding capability is absent in most synthetic cobalt porphyrins with nitrite ligands, it is thus not surprising that this O-binding mode has yet to be observed in these model compounds. It is somewhat surprising, however, that even in the picket fence porphyrin derivatives such as (TpivPP)Co(NO<sub>2</sub>)(1-MeIm) which provide electrostatic interactions between “distal” NH groups and bound nitrite, that this stabilization is not sufficient to induce O-binding of the nitrite group,<sup>116</sup> perhaps due to the artificial symmetrical nature of the distal pockets.

In summary, the X-ray crystal structures reported to date of synthetic Mn, Fe, and Co porphyrins with nitrite ligands reveal a preference for nitrito O-binding for the Mn compound, and nitro N-binding for the Fe and Co compounds. In the Mb derivatives, however, all three metal-nitrite derivatives (Mn<sup>III</sup>, Fe<sup>III</sup>, and Co<sup>III</sup>) reveal the nitrito O-binding mode, suggesting that the distal pocket of Mb is the major determinant in this structural preference for these Mb nitrite derivatives.

## 4.9 Conclusion

The recent biological role of nitrite ion in many physiological processes such as hypoxic vasodilation, ischemia reperfusion, and mitochondrial respiration has been demonstrated to be due to its conversion to NO under enzymatic or nonenzymatic reduction. In the enzymatic pathway, deoxy hemoglobin and deoxy myoglobin have been reported to mediate this conversion. We are interested in the active site structure of the complexes formed from myoglobin–nitrite or myoglobin-NO adducts and how the metal-heme center and the peripheral amino acids in the distal pocket will affect the binding mode of these biologically important ligands. Our group has previously reported the unusual nitrito O-binding mode of coordinated nitrite in the iron-containing hh Mb<sup>III</sup>(ONO). In this chapter, we reported the 1.60 Å resolution crystal structures of the nitrite adducts of manganese and cobalt-substituted horse heart myoglobin (hh MnMb, hh CoMb). Interestingly, both of the structures reveal the O-binding mode (hh Mn<sup>III</sup>Mb(ONO), hh Co<sup>III</sup>Mb(ONO)) although all known cobalt nitrite model compounds are showing N-bound nitrite coordination mode suggesting the effective role of the distal histidine amino acid (His 64) in forcing the O-binding mode through the H-bonding with the coordinated oxygen atom of nitrite ion. In addition we reported the 1.90 Å resolution crystal structure of MnMb-NO adduct. The structure suggests a loosely bound NO in the distal pocket; the Mn–N–O moiety is surprisingly bent, and represents the first such distinctly bent metal-NO unit for a natural or synthetic manganese porphyrin complex. We also reported the high resolution crystal structures of the oxidized Mn-substituted horse heart myoglobin (hh Mn<sup>III</sup>Mb), the reduced form (hh Mn<sup>II</sup>Mb), and complexes of hh MnMb with

methanol, and azide. The Mn<sup>III</sup>Mb compound contains distal pocket water in two positions, one coordinated and the other uncoordinated. This finding explains the controversial spectroscopic, kinetic, and electrochemical properties reported in the literature. The reduced form, Mn<sup>II</sup>Mb, lacks a distal pocket water molecule, in contrast to that observed previously for the iron-containing *deoxy*Mb.

#### 4.10 References

- (1) Gray, H.; Ellis, W. *In: Bertini I, Gray HB, Lippard SJ, Valentine JS (eds), Bioinorganic Chemistry. University Science Books, Mill Valley, 1994, 315-364.*
- (2) Eichhorn, G.; Marzilli, L. *In: Heme proteins, Advances in inorganic biochemistry series No. 7, Elsevier, New York, 1988.*
- (3) Dawson, J. H. *Science* **1988**, *24*, 433.
- (4) Yonetani, T.; Yamamoto, H.; Woodrow, G. V. *J. Biol. Chem.* **1974**, *249*, 682-690.
- (5) Bull, C.; Fisher, R. G.; Hoffman, B. M. *Biochem. Biophys. Res. Commun.* **1974**, *59*, 140-145.
- (6) Boucher, L. J. *Coord. Chem. Rev.* **1972**, *7*, 289-329.
- (7) Gibson, Q. H.; Hoffman, B. M. *J. Biol. Chem.* **1979**, *254*, 4691-4697.
- (8) Fabry, T. L.; Simo, C.; Javaherian, K. *Biochim. Biophys. Acta* **1968**, *160*, 118-122.
- (9) Yonetani, T.; Drots, H. R.; Leigh, J. S.; Jr; Reed, G. H.; Waterman, M. R.; Asakura, T. *J. Biol. Chem.* **1970**, *245*, 2998-3003.
- (10) Atassi, M. Z. *Biochem. J.* **1967**, *103*, 29-35.
- (11) Yonetani, T.; Asakura, T. *J. Biol. Chem.* **1969**, *244*, 4580-4588.
- (12) Breslow, E. *J. Biol. Chem.* **1964**, *239*, 486-496.
- (13) Gelb, M. H.; Toscano, W. A., Jr.; Sligar, S. G. *Proc. Natl. Acad. Sci. U.S.A* **1982**, *79*, 5758-5762.
- (14) Dierks, E. A.; Hu, S.; Vogel, K. M.; Yu, A. E.; Spiro, T. G.; Burstyn, J. N. *J. Am. Chem. Soc.* **1997**, *119*, 7316-7323.
- (15) Chien, J. C. W.; Dickinson, L. C. *J. Biol. Chem.* **1977**, *252*, 1331-1335.
- (16) Hemmens, B.; Gorren, A. C. F.; Schmidt, K.; Werner, E. R.; Mayer, B. *Biochem. J.* **1998**, *332*, 337-342.
- (17) Theorell, H. *Nature (London)* **1945**, *156*, 474.
- (18) Ozols, J.; Strittmatter, P. *J. Biol. Chem.* **1964**, *239*, 1018-1023.
- (19) Yonetani, T. *J. Biol. Chem.* **1967**, *242*, 5008-5013.
- (20) Yonetani, T.; Asakura, T. *J. Biol. Chem.* **1968**, *243*, 3996-3998.

- (21) Gupta, K.; Selinsky, B. S.; Loll, P. J. *Acta Cryst.* **2006**, *D62*, 151–156.
- (22) Yu, N.-T.; Tsubaki, M. *Biochemistry* **1980**, *19*, 4647-4653.
- (23) Parthasarathi, N.; Spiro, T. G. *Inorg. Chem.* **1987**, *26*, 3792-3796.
- (24) Moffat, K.; Loe, R. S. *J. Mol. Biol.* **1976**, *104*, 669-685.
- (25) Moffat, K.; Loe, R. S.; Hoffman, B. M. *J. Am. Chem. Soc.* **1974**, *96*, 5259-5261.
- (26) Hoffman, B. M.; Gibson, Q. H. *Biochemistry* **1976**, *15*, 3405-3410.
- (27) Parthasarathi, N.; Spiro, T. G. *Inorg. Chem.* **1987**, *26*, 2280-2282.
- (28) Masuya, F.; Hori, H. *Biochimica et Biophysica Acta* **1993**, *1203*, 99-103.
- (29) Mondal, M. S.; Mazumdar, S.; Mitra, S. *Inorg. Chem.* **1993**, *32*, 5362-5367.
- (30) Gibson, Q. H.; Hoffman, B. M.; Crepeau, R. H.; Edelstein, S. J.; Bull, C. *Biochem. Biophys. Res. Commun.* **1974**, *59*, 146-151.
- (31) Hoffman, B. M.; Gibson, Q. H.; Bull, C.; Crepeau, R. H.; Edelstein, S. J.; Fisher, R. G.; McDonald, M. J. *Ann. N. Y. Acad. Sci.* **1975**, *244*, 174-186.
- (32) Yonetani, T.; Yamamoto, H.; Erman, J. E.; J. S. Leigh, J.; Reed, G. H. *J. Biol. Chem.* **1972**, *247*, 2447-2455.
- (33) Lin, S.-H.; Yu, N.-T.; Gersonde, K. *FEBS Lett.* **1988**, *229*, 367-371.
- (34) Lan, E. H.; Dave, B. C.; Fukuto, J. M.; Dunn, B.; Zink, J. I.; Valentine, J. S. *J. Mater. Chem.* **1999**, *9*, 45–53.
- (35) Wayland, B. B.; Olson, L. W. *J. Am. Chem. Soc.* **1974**, *96*, 6037-6041.
- (36) Wayland, B. B.; Olson, L. W.; Siddiqui, Z. U. *J. Am. Chem. Soc.* **1976**, *98*, 94-98.
- (37) Piciulo, P. L.; Scheidt, W. R. *Inorg. Nucl. Chem. Lett.* **1975**, *11*, 309-311.
- (38) KELLY, S.; Lancon, D.; Kadish, K. M. *Inorg. Chem.* **1984**, *23*, 1451-1458.
- (39) Yi, J.; Namjou, K.; Zahran, Z. N.; McCann, P. J.; Richter-Addo, G. B. *Nitric Oxide* **2006**, *15*, 154-162.
- (40) Zahran, Z. N.; Lee, J.; Alguindigue, S. S.; Khan, M. A.; Richter-Addo, G. B. *Dalton Trans.* **2004**, 44–50.
- (41) Yu, C.-H.; Su, Y. O. *J. Electroanal. Chem.* **1994**, *368*, 323-327.
- (42) Keilin, D. *Proc. Roy. Soc. B* **1936**, *121*, 165-173.
- (43) Azarov, I.; Huang, K. T.; Basu, S.; Gladwin, M. T.; Hogg, N.; Kim-Shapiro, D. B. *J. Biol. Chem.* **2005**, *280*, 39024–39032.
- (44) Bryan, N. S. *Free Rad. Biol. Med.* **2006**, *41*, 691-701.
- (45) Teale, F. W. J. *Biochim. Biophys. Acta* **1959**, *35*, 543.
- (46) Langley, R.; Hambright, P.; Alston, K. *Inorg. Chem.* **1986**, *25*, 114-117.
- (47) Pflugrath, J. *Acta Crystallogr.* **1999**, *D55*, 1718-1725.
- (48) By Collaborative Computational Project, N. S. D. L., Warrington WA4 4AD, England *Acta Cryst.* **1994**, *D50*, 760-763.
- (49) Vagin, A.; Teplyakov, A. *J. Appl. Crystallogr.* **1997**, *30*, 1022-1025.

- (50) Copeland, D. M.; Soares, A.; West, A. H.; Richter-Addo, G. B. *J. Inorg. Biochem.* **2006**, *100*, 1413-1425.
- (51) Arendall III, W. B.; Tempel, W.; Richardson, J. S.; Zhou, W.; Wang, S.; Davis, I. W.; Liu, Z.-J.; Rose, J. P.; Carson, W. M.; Luo, M.; Richardson, D. C.; Wang, B.-C. *J. Struct. Funct. Genomics* **2005**, *6*, 1-11.
- (52) Davis, I. W.; Murray, L. W.; Richardson, J. S.; Richardson, D. C. *Nucl. Acids Res.* **2004**, *32* (Web Server), W615-W619.
- (53) Brunger, A. T.; Adams, P. D.; Clore, G. M.; DeLano, W. L.; Gros, P.; Grosse-Kunstleve, R. W.; Jiang, J.-S.; Kuszewski, J.; Nilges, M.; Pannu, N. S.; Reed, R. J.; Rice, L. M.; Simonson, T.; Warren, G. L. *Acta Crystallogr.* **1998**, *D54*, 905-921.
- (54) Williamson, M. M.; Hill, C. L. *Inorg. Chem.* **1987**, *26*, 4155-4160.
- (55) Williamson, M. M.; Hill, C. L. *Inorg. Chem.* **1986**, *25*, 4668-4671.
- (56) Cheng, B.; Cukiernik, F.; Fries, P. H.; Marchon, J.-C.; Scheidt, W. R. *Inorg. Chem.* **1995**, *34*, 4627-4639.
- (57) Day, V. W.; Stults, B. R.; Tasset, A. L.; Day, R. O.; Marianelli, R. S. *J. Am. Chem. Soc.* **1974**, *96*, 2650-2652.
- (58) Hatano, K.; Anzai, K.; Iitaka, Y. *Bull. Chem. Soc. Jpn.* **1983**, *56*, 422-427.
- (59) Cheng, B.; Scheidt, W. R. *Acta Cryst.* **1996**, *C52*, 361-363.
- (60) Kirner, J. F.; Reed, C. A.; Scheidt, W. R. *J. Am. Chem. Soc.* **1977**, *99*, 2557-2563.
- (61) Day, V. W.; Stults, B. R.; Tasset, E. L.; Marianelli, R. S. *Inorg. Nucl. Chem. Lett.* **1975**, *11*, 505-509.
- (62) Brooker, S.; McKee, V. *Acta Cryst.* **1993**, *C49*, 441-445.
- (63) Brucker, E. A.; Olson, J. S.; Phillips, G. N. *J. Biol. Chem.* **1996**, *271*, 25419-25422.
- (64) Sono, M.; Dawson, J. H. *J. Biol. Chem.* **1982**, *257*, 5496-5502, and references therein.
- (65) Hori, H.; Ikeda-Saito, M.; Reed, G. H.; Yonetani, T. *J. Magn. Reson.* **1984**, *58*, 177-185.
- (66) Maurus, R.; Overall, C. M.; Bogumi, R.; Luo, Y.; Mauk, A. G.; Smith, M.; Brayer, G. D. *Biochem. Biophys. Acta* **1997**, *1341*, 1-13.
- (67) Evans, S. V.; Brayer, G. D. *J. Mol. Biol.* **1990**, *213*, 885-897.
- (68) Bohle, D. S.; Sagan, E. S. *Eu. J. inorg. Chem.* **2000**, 1609.
- (69) Vojtechovsky, J.; Chu, K.; Berendzen, J.; Sweet, R. M.; Schlichting, I. *Biophys. J.* **1999**, *77*, 2153-2174.
- (70) Kachalova, G. S.; Popov, A. N.; Bartunik, H. D. *Science* **1999**, *284*, 473-476.
- (71) Quillin, M. L.; Arduini, R. M.; Olson, J. S.; Phillips, G. N., Jr. *J. Mol. Biol.* **1993**, *234*, 140-155.
- (72) Quillin, M. L.; Li, T.; Olson, J. S.; Phillips, G. N., Jr.; Y, D.; Ikeda-Saito, M.; Regan, R.; Carlson, M.; Gibson, Q. H.; Li, H.; Elber, R. *J. Mol. Biol.* **1995**, *245*, 416-436.
- (73) Takano, T. *J. Mol. Biol.* **1977**, *110*, 569-584.

- (74) Krzywda, S.; Murshudov, G. N.; Brzozowski, A. M.; Jaskolski, M.; Scott, E. E.; Klizas, S. A.; Gibson, Q. H.; Olson, J. S.; Wilkinson, A. J. *Biochemistry* **1998**, *37*, 15896-15907.
- (75) Cameron, A. D.; Smerdon, S. J.; Wilkinson, A. J.; Habash, J.; Helliwell, J. R.; Li, T.; Olson, J. S. *Biochemistry* **1993**, *32*, 13061-13070.
- (76) Chu, K.; Vojtchovsky, J.; McMahon, B. H.; Sweet, R. M.; Berendzen, J.; Schlichting, I. *Nature* **2000**, *403*, 921-923.
- (77) Schotte, F.; Soman, J.; Olson, J. S.; Wulff, M.; Anfinrud, P. A. *J. Struct. Biol.* **2004**, *147*, 235-246.
- (78) Lamb, D. C.; Nienhaus, K.; Arcovito, A.; Draghi, F.; Miele, A. E.; Brunori, M.; Nienhaus, G. U. *J. Biol. Chem.* **2002**, *277*, 11636-11644.
- (79) Brunori, M.; Bourgeois, D.; Vallone, B. *J. Struct. Biol.* **2004**, *147*, 223-234.
- (80) Springer, B. A.; Sligar, S. G.; Olson, J. S.; Phillips, G. N., Jr. *Chem. Rev.* **1994**, *94*, 699-714.
- (81) Cox, R. P.; Hollaway, M. R. *Eur. J. Biochem.* **1977**, *74*, 575-587.
- (82) Taniguchi, I.; Li, C.-Z.; Ishida, M.; Yao, Q. *J. Electroanal. Chem.* **1999**, *460*, 245-250.
- (83) Arnone, A.; Rogers, P.; Blough, N. V.; McGourty, J. L.; Hoffman, B. M. *J. Mol. Biol.* **1986**, *188*, 693-706.
- (84) Nienhaus, K.; Ostermann, A.; Nienhaus, G. U.; Parak, F. G.; Schmidt, M. *Biochemistry* **2005**, *44*, 5095-5105.
- (85) Bogumil, R.; Hunter, C. L.; Maurus, R.; Tang, H.-L.; Lee, H.; Lloyd, E.; Brayer, G. D.; Smith, M.; Mauk, A. G. *Biochemistry* **1994**, *33*, 7600-7608.
- (86) Perutz, M. F.; Mathews, F. S. *J. Mol. Biol.* **1966**, *21*, 199-202.
- (87) Deatherage, J. F.; Obendorf, S. K.; Moffat, K. *J. Mol. Biol.* **1979**, *134*, 419-429.
- (88) Stryer, L.; Kendrew, J. C.; Watson, H. C. *J. Mol. Biol.* **1964**, *8*, 96-104.
- (89) Maurus, R.; Bogumi, B.; Nguyen, N. T.; Mauk, A. G.; Brayer, G. *Biochem. J.* **1998**, *322*, 67-74.
- (90) Mattevi, A.; Gatti, G.; Coda, A.; Rizzi, M.; Ascenzi, P.; Brunori, M.; Bolognesi, M. *J. Mol. Recogn.* **1991**, *4*, 1-6.
- (91) Richter-Addo, G. B.; Legzdins, P. *Metal Nitrosyls*; Oxford University Press: New York, 1992.
- (92) Cheng, L.; Novozhilova, I.; Kim, C.; Kovalevsky, A.; Bagley, K. A.; Coppens, P.; Richter-Addo, G. B. *J. Am. Chem. Soc.* **2000**, *122*, 7142-7143.
- (93) Feltham, R. D.; Enemark, J. H. *Top. Stereochem.* **1981**, *12*, 155-215.
- (94) Westcott, B. L.; Enemark, J. H. In *Inorganic Electronic Structure and Spectroscopy*; Lever, A. B. P., Solomon, E. I., Eds.; Wiley and Sons: New York, 1999; Vol. 2 (Applications and Case Studies), p Chapter 7.
- (95) Enemark, J. H.; Feltham, R. D. *Coord. Chem. Rev.* **1974**, *13*, 339-406.
- (96) Wyllie, G. R. A.; Scheidt, W. R. *Chem. Rev.* **2002**, *102*, 1067-1089.

- (97) Wyllie, G. R. A.; Scheidt, W. R. *Inorg. Chem.* **2003**, *42*, 4259-4261.
- (98) Hori, H.; Ikeda-Saito, M.; Yonetani, T. *J. Biol. Chem.* **1981**, *256*, 7M9-7855.
- (99) Scheidt, W. R.; Hatano, K.; Rupprecht, G. A.; Piciulo, P. L. *Inorg. Chem.* **1979**, *18*, 292-299.
- (100) Piciulo, P. L.; Rupprecht, G.; Scheidt, W. R. *J. Am. Chem. Soc.* **1974**, *96*, 5293-5295.
- (101) Yu, N.-T.; Lin, S.-H.; Chang, C. K.; Gersonde, K. *Biophys. J.* **1989**, *55*, 1137-1144.
- (102) Duranski, M. R.; Greer, J. J. M.; Dejam, A.; Jaganmohan, S.; Hogg, N.; Langston, W.; Patel, R. P.; Yet, S.-F.; Wang, X.; Kevil, C. G.; Gladwin, M. T.; Lefer, D. J. *The Journal of Clinical Investigation* **2005**, *115*, 1232-1240.
- (103) Averill, B. A. *Chem. Rev.* **1996**, *96*, 2951-2964.
- (104) Hollocher, T. C. In *Nitric Oxide. Principles and Applications*; Lancaster, J., Ed.; Academic Press: San Diego, 1996, p 289-344.
- (105) Eady, R. R.; Hasnain, S. S. In *Comprehensive Coordination Chemistry II*; Que Jr., L., Tolman, W. B., Eds.; Elsevier: San Diego, CA, 2004; Vol. 8 (Bio-coordination chemistry), p 759-786.
- (106) Williams, P. A.; Fulop, V.; Garman, E. F.; Saunders, N. F. W.; Ferguson, S. J.; Hajdu, J. *Nature* **1997**, *389*, 406-412.
- (107) Einsle, O.; Messerschmidt, A.; Huber, R.; Kroneck, P. M. H.; Neese, F. *J. Am. Chem. Soc.* **2002**, *124*, 11737-11745.
- (108) Crane, B. R.; Siegel, L. M.; Getzoff, E. D. *Biochemistry* **1997**, *36*, 12120-12137.
- (109) Silaghi-Dumitrescu, R. *Inorg. Chem.* **2004**, *43*, 3715-3718.
- (110) Nasri, H.; Ellison, M. K.; Chen, S.; Huynh, B. H.; Scheidt, W. R. *J. Am. Chem. Soc.* **1997**, *119*, 6274-6283.
- (111) Novozhilova, I. V.; Coppens, P.; Lee, J.; Richter-Addo, G. B.; Bagley, K. A. *J. Am. Chem. Soc.* **2006**, *128*, 2093-2104.
- (112) Kim, K.; Lee, W. S.; Kim, H.-J.; Cho, S.-H.; Girolami, G. S.; Godin, P. A.; Suslick, K. S. *Inorg. Chem.* **1991**, *30*, 2652-2656.
- (113) Suslick, K. S.; Watson, R. A. *New. J. Chem.* **1992**, *16*, 633-642.
- (114) Hoshino, M.; Nagashima, Y.; Seki, H. *Inorg. Chem.* **1998**, *37*, 2464-2469.
- (115) Yamamoto, K.; Iitaka, Y. *Chem. Lett.* **1989**, 697-698.
- (116) Jene, P. C.; Ibers, J. A. *Inorg. Chem.* **2000**, *39*, 3823-3827.
- (117) Adachi, H.; Suzuki, H.; Miyazaki, Y.; Iimura, Y.; Hoshino, M. *Inorg. Chem.* **2002**, *41*, 2518-2524.
- (118) Goodwin, J.; Kurtikyan, T.; Standard, J.; Walsh, R.; Zheng, B.; Parmley, D.; Howard, J.; Green, S.; Mardyukov, A.; Przybla, D. E. *Inorg. Chem.* **2005**, *44*, 2215-2223.
- (119) Seki, H.; Okada, K.; Iimura, Y.; Hoshino, M. *J. Phys. Chem. A* **1997**, *101*, 8174-817.

## Appendix

**Table 2.4.** Bond Lengths [Å] for [Ru(bpb)(NO)]<sub>2</sub>(μ-O).

Ru(1)-N(25)	1.7486(17)	C(13)-C(14)	1.388(3)
Ru(1)-O(27)	1.8829(3)	C(13)-H(13)	0.9500
Ru(1)-N(9)	1.9890(16)	C(14)-C(15)	1.398(3)
Ru(1)-N(16)	1.9935(15)	C(14)-H(14)	0.9500
Ru(1)-N(1)	2.1277(15)	C(15)-N(16)	1.417(2)
Ru(1)-N(24)	2.1507(16)	N(16)-C(17)	1.343(2)
N(1)-C(2)	1.335(2)	C(17)-O(18)	1.233(2)
N(1)-C(6)	1.359(2)	C(17)-C(19)	1.511(3)
C(2)-C(3)	1.383(3)	C(19)-N(24)	1.359(2)
C(2)-H(2)	0.9500	C(19)-C(20)	1.385(3)
C(3)-C(4)	1.382(3)	C(20)-C(21)	1.379(3)
C(3)-H(3)	0.9500	C(20)-H(20)	0.9500
C(4)-C(5)	1.386(3)	C(21)-C(22)	1.380(3)
C(4)-H(4)	0.9500	C(21)-H(21)	0.9500
C(5)-C(6)	1.382(3)	C(22)-C(23)	1.383(3)
C(5)-H(5)	0.9500	C(22)-H(22)	0.9500
C(6)-C(7)	1.515(3)	C(23)-N(24)	1.339(3)
C(7)-O(8)	1.230(2)	C(23)-H(23)	0.9500
C(7)-N(9)	1.344(2)	N(25)-O(26)	1.174(2)
N(9)-C(10)	1.416(2)	O(27)-Ru(1)#1	1.8829(3)
C(10)-C(11)	1.395(3)	Cl(1S)-C(1S)	1.764(3)
C(10)-C(15)	1.421(3)	Cl(2S)-C(1S)	1.764(2)
C(11)-C(12)	1.394(3)	C(1S)-H(1SA)	0.9900
C(11)-H(11)	0.9500	C(1S)-H(1SB)	0.9900
C(12)-C(13)	1.385(3)	Cl(1')-C(1S')	1.764(4)
C(12)-H(12)	0.9500	Cl(2')-C(1S')	1.763(4)
C(1S')-H(1S2)	0.99	C(1S')-H(1S1)	0.9900

**Table 2.5.** Bond Angles [°] for [Ru(bpb)(NO)]<sub>2</sub>(μ-O).

N(25)-Ru(1)-O(27)	174.14(5)	N(25)-Ru(1)-N(24)	91.52(7)
N(25)-Ru(1)-N(9)	95.07(7)	O(27)-Ru(1)-N(24)	86.41(4)
O(27)-Ru(1)-N(9)	88.44(5)	N(9)-Ru(1)-N(24)	162.86(6)
N(25)-Ru(1)-N(16)	95.54(7)	N(16)-Ru(1)-N(24)	79.93(6)
O(27)-Ru(1)-N(16)	89.49(5)	N(1)-Ru(1)-N(24)	115.53(6)
N(9)-Ru(1)-N(16)	83.69(6)	C(2)-N(1)-C(6)	119.25(16)
N(25)-Ru(1)-N(1)	91.61(7)	C(2)-N(1)-Ru(1)	130.07(13)
O(27)-Ru(1)-N(1)	84.36(4)	C(6)-N(1)-Ru(1)	110.61(12)
N(9)-Ru(1)-N(1)	80.14(6)	N(1)-C(2)-C(3)	122.19(18)
N(16)-Ru(1)-N(1)	162.84(6)	N(1)-C(2)-H(2)	118.9

C(3)-C(2)-H(2)	118.9	C(17)-N(16)-Ru(1)	119.42(13)
C(4)-C(3)-C(2)	119.01(19)	C(15)-N(16)-Ru(1)	112.24(11)
C(4)-C(3)-H(3)	120.5	O(18)-C(17)-N(16)	127.86(19)
C(2)-C(3)-H(3)	120.5	O(18)-C(17)-C(19)	120.04(17)
C(3)-C(4)-C(5)	119.03(18)	N(16)-C(17)-C(19)	112.09(16)
C(3)-C(4)-H(4)	120.5	N(24)-C(19)-C(20)	121.40(18)
C(5)-C(4)-H(4)	120.5	N(24)-C(19)-C(17)	118.47(16)
C(6)-C(5)-C(4)	119.40(19)	C(20)-C(19)-C(17)	120.09(17)
C(6)-C(5)-H(5)	120.3	C(21)-C(20)-C(19)	119.40(19)
C(4)-C(5)-H(5)	120.3	C(21)-C(20)-H(20)	120.3
N(1)-C(6)-C(5)	121.10(18)	C(19)-C(20)-H(20)	120.3
N(1)-C(6)-C(7)	118.09(16)	C(20)-C(21)-C(22)	119.11(19)
C(5)-C(6)-C(7)	120.78(17)	C(20)-C(21)-H(21)	120.4
O(8)-C(7)-N(9)	127.74(18)	C(22)-C(21)-H(21)	120.4
O(8)-C(7)-C(6)	120.53(16)	C(21)-C(22)-C(23)	119.09(19)
N(9)-C(7)-C(6)	111.72(16)	C(21)-C(22)-H(22)	120.5
C(7)-N(9)-C(10)	128.11(16)	C(23)-C(22)-H(22)	120.5
C(7)-N(9)-Ru(1)	119.42(13)	N(24)-C(23)-C(22)	122.31(19)
C(10)-N(9)-Ru(1)	112.32(12)	N(24)-C(23)-H(23)	118.8
C(11)-C(10)-N(9)	124.36(17)	C(22)-C(23)-H(23)	118.8
C(11)-C(10)-C(15)	119.67(17)	C(23)-N(24)-C(19)	118.71(16)
N(9)-C(10)-C(15)	115.97(17)	C(23)-N(24)-Ru(1)	131.26(13)
C(12)-C(11)-C(10)	119.68(18)	C(19)-N(24)-Ru(1)	110.02(12)
C(12)-C(11)-H(11)	120.2	O(26)-N(25)-Ru(1)	175.85(15)
C(10)-C(11)-H(11)	120.2	Ru(1)-O(27)-Ru(1)#1	180.0
C(13)-C(12)-C(11)	120.76(19)	Cl(2S)-C(1S)-Cl(1S)	111.13(18)
C(13)-C(12)-H(12)	119.6	Cl(2S)-C(1S)-H(1SA)	109.4
C(11)-C(12)-H(12)	119.6	Cl(1S)-C(1S)-H(1SA)	109.4
C(12)-C(13)-C(14)	120.29(18)	Cl(2S)-C(1S)-H(1SB)	109.4
C(12)-C(13)-H(13)	119.9	Cl(1S)-C(1S)-H(1SB)	109.4
C(14)-C(13)-H(13)	119.9	H(1SA)-C(1S)-H(1SB)	108.0
C(13)-C(14)-C(15)	120.14(18)	Cl(2')-C(1S')-Cl(1')	111.0(5)
C(13)-C(14)-H(14)	119.9	Cl(2')-C(1S')-H(1S1)	109.4
C(15)-C(14)-H(14)	119.9	Cl(1')-C(1S')-H(1S1)	109.4
C(14)-C(15)-N(16)	124.77(17)	Cl(2')-C(1S')-H(1S2)	109.4
C(14)-C(15)-C(10)	119.46(18)	Cl(1')-C(1S')-H(1S2)	109.4
N(16)-C(15)-C(10)	115.78(16)	H(1S1)-C(1S')-H(1S2)	108.0
C(17)-N(16)-C(15)	128.29(16)		

**Table 3.6.** Bond Lengths [ $\text{\AA}$ ] for (TTP)Mn(NO)(MeOH).

Mn(1)-N(5)	1.6804(17)	Mn(1)-N(2)	2.0212(16)
Mn(1)-N(1)	2.0077(17)	Mn(1)-N(4)	2.0315(17)
Mn(1)-N(3)	2.0148(17)	Mn(1)-O(2)	2.0863(15)

O(1)-N(5)	1.165(2)	C(22)-C(23)	1.386(3)
O(2)-C(49)	1.455(3)	C(23)-C(24)	1.384(4)
N(1)-C(1)	1.372(2)	C(24)-C(25)	1.394(3)
N(1)-C(4)	1.374(3)	C(24)-C(27)	1.513(3)
N(2)-C(9)	1.380(2)	C(25)-C(26)	1.398(3)
N(2)-C(6)	1.384(3)	C(28)-C(29)	1.386(3)
N(3)-C(14)	1.376(3)	C(28)-C(33)	1.391(3)
N(3)-C(11)	1.379(2)	C(29)-C(30)	1.389(3)
N(4)-C(16)	1.377(3)	C(30)-C(31)	1.381(3)
N(4)-C(19)	1.377(2)	C(31)-C(32)	1.390(3)
C(1)-C(20)	1.403(3)	C(31)-C(34)	1.513(3)
C(1)-C(2)	1.442(3)	C(32)-C(33)	1.387(3)
C(2)-C(3)	1.345(3)	C(35)-C(36)	1.389(3)
C(3)-C(4)	1.437(3)	C(35)-C(40)	1.393(3)
C(4)-C(5)	1.403(3)	C(36)-C(37)	1.394(3)
C(5)-C(6)	1.405(3)	C(37)-C(38)	1.385(4)
C(5)-C(21)	1.497(3)	C(38)-C(39)	1.391(4)
C(6)-C(7)	1.437(3)	C(38)-C(41)	1.511(3)
C(7)-C(8)	1.352(3)	C(39)-C(40)	1.388(3)
C(8)-C(9)	1.441(3)	C(42)-C(47)	1.389(3)
C(9)-C(10)	1.402(3)	C(42)-C(43)	1.397(3)
C(10)-C(11)	1.389(3)	C(43)-C(44)	1.393(3)
C(10)-C(28)	1.504(3)	C(44)-C(45)	1.387(3)
C(11)-C(12)	1.446(3)	C(45)-C(46)	1.387(3)
C(12)-C(13)	1.347(3)	C(45)-C(48)	1.513(3)
C(13)-C(14)	1.445(3)	C(46)-C(47)	1.391(3)
C(14)-C(15)	1.402(3)	Mn(2)-Mn(2)#1	0.3354(18)
C(15)-C(16)	1.395(3)	Mn(2)-N(8)	1.676(3)
C(15)-C(35)	1.496(3)	Mn(2)-O(4)#1	1.748(3)
C(16)-C(17)	1.443(3)	Mn(2)-N(6)#1	2.0044(19)
C(17)-C(18)	1.358(3)	Mn(2)-N(8)#1	2.007(3)
C(18)-C(19)	1.443(3)	Mn(2)-N(7)	2.020(2)
C(19)-C(20)	1.394(3)	Mn(2)-N(6)	2.037(2)
C(20)-C(42)	1.501(3)	Mn(2)-N(7)#1	2.038(2)
C(21)-C(26)	1.392(3)	Mn(2)-O(4)	2.081(3)
C(21)-C(22)	1.404(3)	O(4)-C(74)	1.478(4)

O(4)-Mn(2)#1	1.748(3)	C(60)-C(61)	1.396(3)
N(8)-O(3)	1.169(3)	C(60)-C(65)	1.398(3)
N(8)-Mn(2)#1	2.007(3)	C(61)-C(62)	1.390(3)
N(6)-C(50)	1.375(3)	C(62)-C(63)	1.383(4)
N(6)-C(53)	1.378(3)	C(63)-C(64)	1.387(4)
N(6)-Mn(2)#1	2.0044(19)	C(63)-C(66)	1.517(4)
N(7)-C(58)	1.376(2)	C(64)-C(65)	1.396(4)
N(7)-C(55)	1.379(3)	C(67)-C(72)	1.389(3)
N(7)-Mn(2)#1	2.038(2)	C(67)-C(68)	1.394(3)
C(50)-C(59)#1	1.397(3)	C(68)-C(69)	1.390(3)
C(50)-C(51)	1.438(3)	C(69)-C(70)	1.389(3)
C(51)-C(52)	1.346(3)	C(70)-C(71)	1.380(3)
C(52)-C(53)	1.445(3)	C(70)-C(73)	1.513(3)
C(53)-C(54)	1.398(3)	C(71)-C(72)	1.390(3)
C(54)-C(55)	1.400(3)	C(75)-Cl(2)	1.717(4)
C(54)-C(60)	1.499(3)	C(75)-Cl(1)	1.719(3)
C(55)-C(56)	1.442(3)	C(76)-O(5)	1.465(4)
C(56)-C(57)	1.358(3)	C(77)-O(6)	1.479(5)
C(57)-C(58)	1.445(3)	C(78)-O(7)	1.476(5)
C(58)-C(59)	1.396(3)	C(79)-O(8)	1.479(5)
C(59)-C(50)#1	1.397(3)	C(80)-O(9)	1.472(5)
C(59)-C(67)	1.502(3)		

**Table 3.7.** Bond Angles [°] for (TTP)Mn(NO)(MeOH).

---

N(5)-Mn(1)-N(1)	93.15(8)	N(1)-Mn(1)-O(2)	87.22(6)
N(5)-Mn(1)-N(3)	92.73(8)	N(3)-Mn(1)-O(2)	86.92(6)
N(1)-Mn(1)-N(3)	174.11(7)	N(2)-Mn(1)-O(2)	84.32(6)
N(5)-Mn(1)-N(2)	93.06(8)	N(4)-Mn(1)-O(2)	88.56(6)
N(1)-Mn(1)-N(2)	89.95(7)	C(49)-O(2)-Mn(1)	124.31(13)
N(3)-Mn(1)-N(2)	90.06(7)	C(1)-N(1)-C(4)	105.86(16)
N(5)-Mn(1)-N(4)	94.06(8)	C(1)-N(1)-Mn(1)	127.03(14)
N(1)-Mn(1)-N(4)	89.81(7)	C(4)-N(1)-Mn(1)	127.09(13)
N(3)-Mn(1)-N(4)	89.46(7)	C(9)-N(2)-C(6)	105.46(16)
N(2)-Mn(1)-N(4)	172.88(7)	C(9)-N(2)-Mn(1)	126.79(14)
N(5)-Mn(1)-O(2)	177.36(7)	C(6)-N(2)-Mn(1)	127.38(12)

C(14)-N(3)-C(11)	105.73(16)	C(15)-C(14)-C(13)	123.98(19)
C(14)-N(3)-Mn(1)	127.44(13)	C(16)-C(15)-C(14)	123.79(19)
C(11)-N(3)-Mn(1)	126.73(14)	C(16)-C(15)-C(35)	118.97(17)
C(16)-N(4)-C(19)	105.94(16)	C(14)-C(15)-C(35)	117.22(17)
C(16)-N(4)-Mn(1)	126.80(13)	N(4)-C(16)-C(15)	126.02(17)
C(19)-N(4)-Mn(1)	126.77(14)	N(4)-C(16)-C(17)	110.14(16)
O(1)-N(5)-Mn(1)	175.66(18)	C(15)-C(16)-C(17)	123.84(18)
N(1)-C(1)-C(20)	126.40(18)	C(18)-C(17)-C(16)	106.90(18)
N(1)-C(1)-C(2)	110.03(17)	C(17)-C(18)-C(19)	106.97(17)
C(20)-C(1)-C(2)	123.56(18)	N(4)-C(19)-C(20)	125.57(18)
C(3)-C(2)-C(1)	106.80(17)	N(4)-C(19)-C(18)	110.05(17)
C(2)-C(3)-C(4)	107.38(19)	C(20)-C(19)-C(18)	124.37(17)
N(1)-C(4)-C(5)	126.12(18)	C(19)-C(20)-C(1)	123.87(17)
N(1)-C(4)-C(3)	109.89(17)	C(19)-C(20)-C(42)	119.48(18)
C(5)-C(4)-C(3)	123.97(19)	C(1)-C(20)-C(42)	116.64(18)
C(4)-C(5)-C(6)	124.19(19)	C(26)-C(21)-C(22)	117.8(2)
C(4)-C(5)-C(21)	116.98(17)	C(26)-C(21)-C(5)	123.44(18)
C(6)-C(5)-C(21)	118.76(17)	C(22)-C(21)-C(5)	118.75(18)
N(2)-C(6)-C(5)	124.79(18)	C(23)-C(22)-C(21)	120.8(2)
N(2)-C(6)-C(7)	110.05(17)	C(24)-C(23)-C(22)	121.4(2)
C(5)-C(6)-C(7)	125.17(19)	C(23)-C(24)-C(25)	118.1(2)
C(8)-C(7)-C(6)	107.34(18)	C(23)-C(24)-C(27)	119.9(2)
C(7)-C(8)-C(9)	106.92(17)	C(25)-C(24)-C(27)	122.0(2)
N(2)-C(9)-C(10)	125.27(18)	C(24)-C(25)-C(26)	120.8(2)
N(2)-C(9)-C(8)	110.21(18)	C(21)-C(26)-C(25)	120.9(2)
C(10)-C(9)-C(8)	124.52(17)	C(29)-C(28)-C(33)	118.22(18)
C(11)-C(10)-C(9)	124.74(18)	C(29)-C(28)-C(10)	121.79(19)
C(11)-C(10)-C(28)	117.73(18)	C(33)-C(28)-C(10)	119.99(17)
C(9)-C(10)-C(28)	117.50(18)	C(28)-C(29)-C(30)	120.6(2)
N(3)-C(11)-C(10)	125.89(18)	C(31)-C(30)-C(29)	121.33(19)
N(3)-C(11)-C(12)	110.01(17)	C(30)-C(31)-C(32)	118.11(19)
C(10)-C(11)-C(12)	124.09(18)	C(30)-C(31)-C(34)	121.08(19)
C(13)-C(12)-C(11)	107.00(17)	C(32)-C(31)-C(34)	120.8(2)
C(12)-C(13)-C(14)	107.18(18)	C(33)-C(32)-C(31)	120.8(2)
N(3)-C(14)-C(15)	125.97(17)	C(32)-C(33)-C(28)	120.90(19)
N(3)-C(14)-C(13)	110.06(17)	C(36)-C(35)-C(40)	117.8(2)

C(36)-C(35)-C(15)	120.13(19)	O(4)#1-Mn(2)-N(6)	92.57(11)
C(40)-C(35)-C(15)	122.02(19)	N(6)#1-Mn(2)-N(6)	170.52(5)
C(35)-C(36)-C(37)	120.8(2)	N(8)#1-Mn(2)-N(6)	84.76(13)
C(38)-C(37)-C(36)	121.4(2)	N(7)-Mn(2)-N(6)	89.00(8)
C(37)-C(38)-C(39)	117.7(2)	Mn(2)#1-Mn(2)-N(7)#1	82.2(5)
C(37)-C(38)-C(41)	121.0(2)	N(8)-Mn(2)-N(7)#1	89.80(17)
C(39)-C(38)-C(41)	121.3(2)	O(4)#1-Mn(2)-N(7)#1	97.50(13)
C(40)-C(39)-C(38)	121.2(2)	N(6)#1-Mn(2)-N(7)#1	89.41(8)
C(39)-C(40)-C(35)	121.0(2)	N(8)#1-Mn(2)-N(7)#1	88.87(14)
C(47)-C(42)-C(43)	118.35(18)	N(7)-Mn(2)-N(7)#1	170.53(5)
C(47)-C(42)-C(20)	120.80(17)	N(6)-Mn(2)-N(7)#1	89.30(8)
C(43)-C(42)-C(20)	120.72(19)	Mn(2)#1-Mn(2)-O(4)	6.5(4)
C(44)-C(43)-C(42)	120.2(2)	N(8)-Mn(2)-O(4)	172.2(2)
C(45)-C(44)-C(43)	121.3(2)	O(4)#1-Mn(2)-O(4)	178.75(8)
C(46)-C(45)-C(44)	118.12(19)	N(6)#1-Mn(2)-O(4)	84.35(9)
C(46)-C(45)-C(48)	120.3(2)	N(8)#1-Mn(2)-O(4)	6.59(18)
C(44)-C(45)-C(48)	121.6(2)	N(7)-Mn(2)-O(4)	88.15(11)
C(45)-C(46)-C(47)	121.1(2)	N(6)-Mn(2)-O(4)	86.18(10)
C(42)-C(47)-C(46)	120.82(19)	N(7)#1-Mn(2)-O(4)	82.44(11)
Mn(2)#1-Mn(2)-N(8)	169.9(5)	C(74)-O(4)-Mn(2)#1	122.3(3)
Mn(2)#1-Mn(2)-O(4)#1	172.2(4)	C(74)-O(4)-Mn(2)	123.2(3)
N(8)-Mn(2)-O(4)#1	7.9(2)	Mn(2)#1-O(4)-Mn(2)	1.25(7)
Mn(2)#1-Mn(2)-N(6)#1	90.9(4)	O(3)-N(8)-Mn(2)	167.8(4)
N(8)-Mn(2)-N(6)#1	95.17(15)	O(3)-N(8)-Mn(2)#1	169.4(4)
O(4)#1-Mn(2)-N(6)#1	96.90(11)	Mn(2)-N(8)-Mn(2)#1	1.68(9)
Mn(2)#1-Mn(2)-N(8)#1	8.4(4)	C(50)-N(6)-C(53)	106.00(16)
N(8)-Mn(2)-N(8)#1	178.32(9)	C(50)-N(6)-Mn(2)#1	126.08(14)
O(4)#1-Mn(2)-N(8)#1	173.1(2)	C(53)-N(6)-Mn(2)#1	127.78(14)
N(6)#1-Mn(2)-N(8)#1	85.83(13)	C(50)-N(6)-Mn(2)	126.47(14)
Mn(2)#1-Mn(2)-N(7)	88.3(5)	C(53)-N(6)-Mn(2)	127.02(14)
N(8)-Mn(2)-N(7)	99.62(17)	Mn(2)#1-N(6)-Mn(2)	9.48(5)
O(4)#1-Mn(2)-N(7)	91.89(13)	C(58)-N(7)-C(55)	105.96(17)
N(6)#1-Mn(2)-N(7)	90.74(8)	C(58)-N(7)-Mn(2)	126.27(14)
N(8)#1-Mn(2)-N(7)	81.70(14)	C(55)-N(7)-Mn(2)	127.63(13)
Mn(2)#1-Mn(2)-N(6)	79.6(4)	C(58)-N(7)-Mn(2)#1	126.71(14)
N(8)-Mn(2)-N(6)	94.21(15)	C(55)-N(7)-Mn(2)#1	126.82(14)

Mn(2)-N(7)-Mn(2)#1	9.47(5)	C(50)#1-C(59)-C(67)	116.53(17)
N(6)-C(50)-C(59)#1	126.33(18)	C(61)-C(60)-C(65)	118.2(2)
N(6)-C(50)-C(51)	110.06(18)	C(61)-C(60)-C(54)	121.1(2)
C(59)#1-C(50)-C(51)	123.56(18)	C(65)-C(60)-C(54)	120.6(2)
C(52)-C(51)-C(50)	107.17(18)	C(62)-C(61)-C(60)	120.8(2)
C(51)-C(52)-C(53)	107.21(18)	C(63)-C(62)-C(61)	121.5(2)
N(6)-C(53)-C(54)	125.68(18)	C(62)-C(63)-C(64)	117.6(2)
N(6)-C(53)-C(52)	109.55(18)	C(62)-C(63)-C(66)	121.4(3)
C(54)-C(53)-C(52)	124.75(19)	C(64)-C(63)-C(66)	121.0(3)
C(53)-C(54)-C(55)	124.23(19)	C(63)-C(64)-C(65)	122.0(2)
C(53)-C(54)-C(60)	116.72(17)	C(64)-C(65)-C(60)	119.9(2)
C(55)-C(54)-C(60)	119.02(19)	C(72)-C(67)-C(68)	118.36(18)
N(7)-C(55)-C(54)	125.51(19)	C(72)-C(67)-C(59)	120.88(19)
N(7)-C(55)-C(56)	110.03(17)	C(68)-C(67)-C(59)	120.65(17)
C(54)-C(55)-C(56)	124.44(19)	C(69)-C(68)-C(67)	120.21(18)
C(57)-C(56)-C(55)	107.03(19)	C(70)-C(69)-C(68)	121.5(2)
C(56)-C(57)-C(58)	106.89(18)	C(71)-C(70)-C(69)	117.92(18)
N(7)-C(58)-C(59)	125.71(19)	C(71)-C(70)-C(73)	121.31(19)
N(7)-C(58)-C(57)	110.08(17)	C(69)-C(70)-C(73)	120.8(2)
C(59)-C(58)-C(57)	124.20(18)	C(70)-C(71)-C(72)	121.4(2)
C(58)-C(59)-C(50)#1	124.40(18)	C(67)-C(72)-C(71)	120.7(2)
C(58)-C(59)-C(67)	119.08(18)	Cl(2)-C(75)-Cl(1)	105.9(3)

**Table 3.8.** Bond Lengths [ $\text{\AA}$ ] for (TTP)Mn(NO)(1-MeIm).

---

Mn(1)-N(5)	1.650(2)	N(2)-C(6)	1.376(4)
Mn(1)-N(3)	2.023(2)	N(2)-C(9)	1.379(3)
Mn(1)-N(1)	2.024(2)	N(3)-C(14)	1.370(4)
Mn(1)-N(2)	2.027(2)	N(3)-C(11)	1.377(3)
Mn(1)-N(4)	2.029(2)	N(4)-C(19)	1.374(4)
Mn(1)-N(6)	2.096(2)	N(4)-C(16)	1.384(4)
O(1)-N(5)	1.174(3)	N(6)-C(51)	1.324(4)
N(1)-C(4)	1.374(4)	N(6)-C(49)	1.374(4)
N(1)-C(1)	1.381(3)	N(7)-C(51)	1.341(4)

N(7)-C(50)	1.374(4)	C(22)-C(23)	1.399(5)
N(7)-C(52)	1.463(4)	C(22)-H(22A)	0.9500
C(1)-C(20)	1.397(4)	C(23)-C(24)	1.387(5)
C(1)-C(2)	1.442(4)	C(23)-H(23A)	0.9500
C(2)-C(3)	1.350(4)	C(24)-C(25)	1.389(5)
C(2)-H(2A)	0.9500	C(24)-C(27)	1.512(5)
C(3)-C(4)	1.449(4)	C(25)-C(26)	1.388(5)
C(3)-H(3A)	0.9500	C(25)-H(25A)	0.9500
C(4)-C(5)	1.403(4)	C(26)-H(26A)	0.9500
C(5)-C(6)	1.411(4)	C(27)-H(27A)	0.9800
C(5)-C(21)	1.496(4)	C(27)-H(27B)	0.9800
C(6)-C(7)	1.444(4)	C(27)-H(27C)	0.9800
C(7)-C(8)	1.355(4)	C(28)-C(29)	1.389(4)
C(7)-H(7A)	0.9500	C(28)-C(33)	1.390(4)
C(8)-C(9)	1.437(4)	C(29)-C(30)	1.390(4)
C(8)-H(8A)	0.9500	C(29)-H(29A)	0.9500
C(9)-C(10)	1.402(4)	C(30)-C(31)	1.381(5)
C(10)-C(11)	1.388(4)	C(30)-H(30A)	0.9500
C(10)-C(28)	1.498(4)	C(31)-C(32)	1.381(6)
C(11)-C(12)	1.446(4)	C(31)-C(34)	1.516(5)
C(12)-C(13)	1.339(4)	C(32)-C(33)	1.390(5)
C(12)-H(12A)	0.9500	C(32)-H(32A)	0.9500
C(13)-C(14)	1.447(4)	C(33)-H(33A)	0.9500
C(13)-H(13A)	0.9500	C(34)-H(34A)	0.9800
C(14)-C(15)	1.392(4)	C(34)-H(34B)	0.9800
C(15)-C(16)	1.395(4)	C(34)-H(34C)	0.9800
C(15)-C(35)	1.494(4)	C(35)-C(36)	1.397(5)
C(16)-C(17)	1.433(4)	C(35)-C(40)	1.397(4)
C(17)-C(18)	1.361(4)	C(36)-C(37)	1.392(5)
C(17)-H(17A)	0.9500	C(36)-H(36A)	0.9500
C(18)-C(19)	1.439(5)	C(37)-C(38)	1.382(5)
C(18)-H(18A)	0.9500	C(37)-H(37A)	0.9500
C(19)-C(20)	1.402(4)	C(38)-C(39)	1.379(5)
C(20)-C(42)	1.497(4)	C(38)-C(41)	1.511(5)
C(21)-C(22)	1.390(4)	C(39)-C(40)	1.380(5)
C(21)-C(26)	1.398(4)	C(39)-H(39A)	0.9500

C(40)-H(40A)	0.9500	C(77)-H(77A)	0.9500
C(41)-H(41A)	0.9800	C(78)-C(79)	1.376(10)
C(41)-H(41B)	0.9800	C(78)-H(78A)	0.9500
C(41)-H(41C)	0.9800	C(79)-H(79A)	0.9500
C(42)-C(47)	1.397(4)	C(80)-H(80A)	0.9800
C(42)-C(43)	1.400(4)	C(80)-H(80B)	0.9800
C(43)-C(44)	1.398(4)	C(80)-H(80C)	0.9800
C(43)-H(43A)	0.9500	N(10)-O(2)	1.127(10)
C(44)-C(45)	1.380(5)	C(81)-Cl(2)	1.719(4)
C(44)-H(44A)	0.9500	C(81)-Cl(1)	1.720(4)
C(45)-C(46)	1.390(5)	C(81)-H(81A)	0.9900
C(45)-C(48)	1.509(5)	C(81)-H(81B)	0.9900
C(46)-C(47)	1.387(4)	N(8)-C(53)	1.365(3)
C(46)-H(46A)	0.9500	N(8)-C(56)	1.375(4)
C(47)-H(47A)	0.9500	N(8)-Mn(2)#1	2.072(3)
C(48)-H(48A)	0.9800	N(9)-C(61)	1.369(3)
C(48)-H(48B)	0.9800	N(9)-C(58)	1.378(3)
C(48)-H(48C)	0.9800	N(9)-Mn(2)#1	1.981(3)
C(49)-C(50)	1.359(4)	C(53)-C(62)#1	1.396(4)
C(49)-H(49A)	0.9500	C(53)-C(54)	1.439(4)
C(50)-H(50A)	0.9500	C(54)-C(55)	1.345(4)
C(51)-H(51A)	0.9500	C(54)-H(54A)	0.9500
C(52)-H(52A)	0.9800	C(55)-C(56)	1.441(4)
C(52)-H(52B)	0.9800	C(55)-H(55A)	0.9500
C(52)-H(52C)	0.9800	C(56)-C(57)	1.403(4)
Mn(2)-N(10)	1.755(9)	C(57)-C(58)	1.405(4)
Mn(2)-N(9)#1	1.981(3)	C(57)-C(63)	1.495(4)
Mn(2)-N(8)	1.992(3)	C(58)-C(59)	1.439(4)
Mn(2)-N(9)	2.068(3)	C(59)-C(60)	1.345(4)
Mn(2)-N(8)#1	2.072(3)	C(59)-H(59A)	0.9500
Mn(2)-N(11)	2.047(7)	C(60)-C(61)	1.436(4)
N(11)-C(79)	1.332(9)	C(60)-H(60A)	0.9500
N(11)-C(77)	1.482(8)	C(61)-C(62)	1.397(4)
N(12)-C(77)	1.349(8)	C(62)-C(53)#1	1.396(4)
N(12)-C(78)	1.375(8)	C(62)-C(70)	1.498(4)
N(12)-C(80)	1.486(8)	C(63)-C(68)	1.394(4)

C(63)-C(64)	1.405(4)	C(72)-H(72A)	0.9500
C(64)-C(65)	1.393(4)	C(73)-C(74)	1.389(5)
C(64)-H(64A)	0.9500	C(73)-C(76)	1.506(4)
C(65)-C(66)	1.391(5)	C(74)-C(75)	1.389(4)
C(65)-H(65A)	0.9500	C(74)-H(74A)	0.9500
C(66)-C(67)	1.379(5)	C(75)-H(75A)	0.9500
C(66)-C(69)	1.513(5)	C(76)-H(76A)	0.9800
C(67)-C(68)	1.387(4)	C(76)-H(76B)	0.9800
C(67)-H(67A)	0.9500	C(76)-H(76C)	0.9800
C(68)-H(68A)	0.9500	C(82)-Cl(4)	1.722(3)
C(69)-H(69A)	0.9800	C(82)-Cl(3)	1.723(4)
C(69)-H(69B)	0.9800	C(82)-H(82A)	0.9900
C(69)-H(69C)	0.9800	C(82)-H(82B)	0.9900
C(70)-C(75)	1.392(4)	C(82')-Cl(3')	1.722(4)
C(70)-C(71)	1.396(4)	C(82')-Cl(4')	1.722(4)
C(71)-C(72)	1.380(4)	C(82')-H(82C)	0.9900
C(71)-H(71A)	0.9500	C(82')-H(82D)	0.9900
C(72)-C(73)	1.396(5)		

**Table 3.9.** Bond Angles [°] for (TTP)Mn(NO)(1-MeIm).

N(5)-Mn(1)-N(3)	91.13(10)	C(4)-N(1)-C(1)	106.3(2)
N(5)-Mn(1)-N(1)	94.19(10)	C(4)-N(1)-Mn(1)	126.86(18)
N(3)-Mn(1)-N(1)	174.68(9)	C(1)-N(1)-Mn(1)	126.8(2)
N(5)-Mn(1)-N(2)	94.68(11)	C(6)-N(2)-C(9)	105.9(2)
N(3)-Mn(1)-N(2)	89.68(9)	C(6)-N(2)-Mn(1)	126.96(18)
N(1)-Mn(1)-N(2)	89.92(10)	C(9)-N(2)-Mn(1)	126.8(2)
N(5)-Mn(1)-N(4)	93.11(11)	C(14)-N(3)-C(11)	106.5(2)
N(3)-Mn(1)-N(4)	90.02(10)	C(14)-N(3)-Mn(1)	126.90(18)
N(1)-Mn(1)-N(4)	89.65(10)	C(11)-N(3)-Mn(1)	126.5(2)
N(2)-Mn(1)-N(4)	172.21(9)	C(19)-N(4)-C(16)	106.0(2)
N(5)-Mn(1)-N(6)	176.76(11)	C(19)-N(4)-Mn(1)	127.3(2)
N(3)-Mn(1)-N(6)	86.85(9)	C(16)-N(4)-Mn(1)	126.54(19)
N(1)-Mn(1)-N(6)	87.84(9)	O(1)-N(5)-Mn(1)	176.6(2)
N(2)-Mn(1)-N(6)	87.84(9)	C(51)-N(6)-C(49)	105.3(2)
N(4)-Mn(1)-N(6)	84.38(9)	C(51)-N(6)-Mn(1)	125.97(19)

C(49)-N(6)-Mn(1)	128.3(2)	C(10)-C(11)-C(12)	123.8(3)
C(51)-N(7)-C(50)	107.2(3)	C(13)-C(12)-C(11)	107.1(3)
C(51)-N(7)-C(52)	125.9(3)	C(13)-C(12)-H(12A)	126.5
C(50)-N(7)-C(52)	126.9(3)	C(11)-C(12)-H(12A)	126.5
N(1)-C(1)-C(20)	126.1(3)	C(12)-C(13)-C(14)	107.6(3)
N(1)-C(1)-C(2)	109.7(2)	C(12)-C(13)-H(13A)	126.2
C(20)-C(1)-C(2)	124.2(3)	C(14)-C(13)-H(13A)	126.2
C(3)-C(2)-C(1)	107.3(2)	N(3)-C(14)-C(15)	125.8(3)
C(3)-C(2)-H(2A)	126.4	N(3)-C(14)-C(13)	109.3(2)
C(1)-C(2)-H(2A)	126.4	C(15)-C(14)-C(13)	124.9(3)
C(2)-C(3)-C(4)	107.1(3)	C(14)-C(15)-C(16)	125.3(3)
C(2)-C(3)-H(3A)	126.4	C(14)-C(15)-C(35)	117.2(2)
C(4)-C(3)-H(3A)	126.4	C(16)-C(15)-C(35)	117.5(3)
N(1)-C(4)-C(5)	126.5(3)	N(4)-C(16)-C(15)	125.2(3)
N(1)-C(4)-C(3)	109.6(2)	N(4)-C(16)-C(17)	110.1(2)
C(5)-C(4)-C(3)	123.8(3)	C(15)-C(16)-C(17)	124.7(3)
C(4)-C(5)-C(6)	123.5(3)	C(18)-C(17)-C(16)	106.8(3)
C(4)-C(5)-C(21)	118.8(2)	C(18)-C(17)-H(17A)	126.6
C(6)-C(5)-C(21)	117.7(2)	C(16)-C(17)-H(17A)	126.6
N(2)-C(6)-C(5)	126.0(3)	C(17)-C(18)-C(19)	107.2(3)
N(2)-C(6)-C(7)	109.9(2)	C(17)-C(18)-H(18A)	126.4
C(5)-C(6)-C(7)	124.1(3)	C(19)-C(18)-H(18A)	126.4
C(8)-C(7)-C(6)	107.0(3)	N(4)-C(19)-C(20)	125.6(3)
C(8)-C(7)-H(7A)	126.5	N(4)-C(19)-C(18)	109.8(3)
C(6)-C(7)-H(7A)	126.5	C(20)-C(19)-C(18)	124.6(3)
C(7)-C(8)-C(9)	107.0(3)	C(1)-C(20)-C(19)	124.3(3)
C(7)-C(8)-H(8A)	126.5	C(1)-C(20)-C(42)	118.4(3)
C(9)-C(8)-H(8A)	126.5	C(19)-C(20)-C(42)	117.3(3)
N(2)-C(9)-C(10)	125.6(3)	C(22)-C(21)-C(26)	118.2(3)
N(2)-C(9)-C(8)	110.2(2)	C(22)-C(21)-C(5)	120.5(3)
C(10)-C(9)-C(8)	124.2(3)	C(26)-C(21)-C(5)	121.3(3)
C(11)-C(10)-C(9)	124.0(3)	C(21)-C(22)-C(23)	120.6(3)
C(11)-C(10)-C(28)	116.7(3)	C(21)-C(22)-H(22A)	119.7
C(9)-C(10)-C(28)	119.2(3)	C(23)-C(22)-H(22A)	119.7
N(3)-C(11)-C(10)	126.7(3)	C(24)-C(23)-C(22)	121.3(3)
N(3)-C(11)-C(12)	109.5(3)	C(24)-C(23)-H(23A)	119.3

C(22)-C(23)-H(23A)	119.3	H(34A)-C(34)-H(34B)	109.5
C(23)-C(24)-C(25)	117.6(3)	C(31)-C(34)-H(34C)	109.5
C(23)-C(24)-C(27)	120.7(3)	H(34A)-C(34)-H(34C)	109.5
C(25)-C(24)-C(27)	121.7(3)	H(34B)-C(34)-H(34C)	109.5
C(26)-C(25)-C(24)	121.8(3)	C(36)-C(35)-C(40)	117.8(3)
C(26)-C(25)-H(25A)	119.1	C(36)-C(35)-C(15)	121.6(3)
C(24)-C(25)-H(25A)	119.1	C(40)-C(35)-C(15)	120.6(3)
C(25)-C(26)-C(21)	120.4(3)	C(37)-C(36)-C(35)	120.3(3)
C(25)-C(26)-H(26A)	119.8	C(37)-C(36)-H(36A)	119.9
C(21)-C(26)-H(26A)	119.8	C(35)-C(36)-H(36A)	119.9
C(24)-C(27)-H(27A)	109.5	C(38)-C(37)-C(36)	121.3(3)
C(24)-C(27)-H(27B)	109.5	C(38)-C(37)-H(37A)	119.4
H(27A)-C(27)-H(27B)	109.5	C(36)-C(37)-H(37A)	119.4
C(24)-C(27)-H(27C)	109.5	C(39)-C(38)-C(37)	118.4(3)
H(27A)-C(27)-H(27C)	109.5	C(39)-C(38)-C(41)	120.1(3)
H(27B)-C(27)-H(27C)	109.5	C(37)-C(38)-C(41)	121.5(4)
C(29)-C(28)-C(33)	117.9(3)	C(38)-C(39)-C(40)	121.2(3)
C(29)-C(28)-C(10)	120.9(3)	C(38)-C(39)-H(39A)	119.4
C(33)-C(28)-C(10)	121.1(3)	C(40)-C(39)-H(39A)	119.4
C(28)-C(29)-C(30)	121.1(3)	C(39)-C(40)-C(35)	121.0(3)
C(28)-C(29)-H(29A)	119.4	C(39)-C(40)-H(40A)	119.5
C(30)-C(29)-H(29A)	119.4	C(35)-C(40)-H(40A)	119.5
C(31)-C(30)-C(29)	120.9(3)	C(38)-C(41)-H(41A)	109.5
C(31)-C(30)-H(30A)	119.5	C(38)-C(41)-H(41B)	109.5
C(29)-C(30)-H(30A)	119.5	H(41A)-C(41)-H(41B)	109.5
C(30)-C(31)-C(32)	118.0(3)	C(38)-C(41)-H(41C)	109.5
C(30)-C(31)-C(34)	120.9(4)	H(41A)-C(41)-H(41C)	109.5
C(32)-C(31)-C(34)	121.1(4)	H(41B)-C(41)-H(41C)	109.5
C(31)-C(32)-C(33)	121.6(3)	C(47)-C(42)-C(43)	118.3(3)
C(31)-C(32)-H(32A)	119.2	C(47)-C(42)-C(20)	122.0(3)
C(33)-C(32)-H(32A)	119.2	C(43)-C(42)-C(20)	119.7(3)
C(28)-C(33)-C(32)	120.4(3)	C(44)-C(43)-C(42)	120.1(3)
C(28)-C(33)-H(33A)	119.8	C(44)-C(43)-H(43A)	119.9
C(32)-C(33)-H(33A)	119.8	C(42)-C(43)-H(43A)	119.9
C(31)-C(34)-H(34A)	109.5	C(45)-C(44)-C(43)	121.5(3)
C(31)-C(34)-H(34B)	109.5	C(45)-C(44)-H(44A)	119.3

C(43)-C(44)-H(44A)	119.3	N(8)-Mn(2)-N(9)	88.70(12)
C(44)-C(45)-C(46)	118.1(3)	N(10)-Mn(2)-N(8)#1	92.1(3)
C(44)-C(45)-C(48)	121.2(3)	N(9)#1-Mn(2)-N(8)#1	88.90(12)
C(46)-C(45)-C(48)	120.6(3)	N(8)-Mn(2)-N(8)#1	171.28(10)
C(47)-C(46)-C(45)	121.4(3)	N(9)-Mn(2)-N(8)#1	88.21(10)
C(47)-C(46)-H(46A)	119.3	N(10)-Mn(2)-N(11)	173.2(4)
C(45)-C(46)-H(46A)	119.3	N(9)#1-Mn(2)-N(11)	85.3(2)
C(46)-C(47)-C(42)	120.5(3)	N(8)-Mn(2)-N(11)	89.6(2)
C(46)-C(47)-H(47A)	119.7	N(9)-Mn(2)-N(11)	86.2(2)
C(42)-C(47)-H(47A)	119.7	N(8)#1-Mn(2)-N(11)	82.10(19)
C(45)-C(48)-H(48A)	109.5	C(79)-N(11)-C(77)	99.9(6)
C(45)-C(48)-H(48B)	109.5	C(79)-N(11)-Mn(2)	139.2(5)
H(48A)-C(48)-H(48B)	109.5	C(77)-N(11)-Mn(2)	119.8(4)
C(45)-C(48)-H(48C)	109.5	C(77)-N(12)-C(78)	106.8(5)
H(48A)-C(48)-H(48C)	109.5	C(77)-N(12)-C(80)	126.9(5)
H(48B)-C(48)-H(48C)	109.5	C(78)-N(12)-C(80)	126.0(5)
C(50)-C(49)-N(6)	109.9(3)	N(12)-C(77)-N(11)	111.4(5)
C(50)-C(49)-H(49A)	125.0	N(12)-C(77)-H(77A)	124.3
N(6)-C(49)-H(49A)	125.0	N(11)-C(77)-H(77A)	124.3
C(49)-C(50)-N(7)	106.0(3)	N(12)-C(78)-C(79)	106.5(5)
C(49)-C(50)-H(50A)	127.0	N(12)-C(78)-H(78A)	126.7
N(7)-C(50)-H(50A)	127.0	C(79)-C(78)-H(78A)	126.7
N(6)-C(51)-N(7)	111.6(3)	N(11)-C(79)-C(78)	115.4(6)
N(6)-C(51)-H(51A)	124.2	N(11)-C(79)-H(79A)	122.3
N(7)-C(51)-H(51A)	124.2	C(78)-C(79)-H(79A)	122.3
N(7)-C(52)-H(52A)	109.5	O(2)-N(10)-Mn(2)	158.6(7)
N(7)-C(52)-H(52B)	109.5	Cl(2)-C(81)-Cl(1)	111.0(3)
H(52A)-C(52)-H(52B)	109.5	Cl(2)-C(81)-H(81A)	109.4
N(7)-C(52)-H(52C)	109.5	Cl(1)-C(81)-H(81A)	109.4
H(52A)-C(52)-H(52C)	109.5	Cl(2)-C(81)-H(81B)	109.4
H(52B)-C(52)-H(52C)	109.5	Cl(1)-C(81)-H(81B)	109.4
N(10)-Mn(2)-N(9)#1	98.3(3)	H(81A)-C(81)-H(81B)	108.0
N(10)-Mn(2)-N(8)	96.0(3)	C(53)-N(8)-C(56)	106.6(2)
N(9)#1-Mn(2)-N(8)	92.97(11)	C(53)-N(8)-Mn(2)	124.75(19)
N(10)-Mn(2)-N(9)	90.0(3)	C(56)-N(8)-Mn(2)	128.67(19)
N(9)#1-Mn(2)-N(9)	171.31(9)	C(53)-N(8)-Mn(2)#1	126.85(19)

C(56)-N(8)-Mn(2)#1	125.95(19)	C(53)#1-C(62)-C(70)	117.9(2)
Mn(2)-N(8)-Mn(2)#1	8.72(10)	C(61)-C(62)-C(70)	117.5(2)
C(61)-N(9)-C(58)	105.9(2)	C(68)-C(63)-C(64)	117.5(3)
C(61)-N(9)-Mn(2)#1	124.80(19)	C(68)-C(63)-C(57)	121.8(3)
C(58)-N(9)-Mn(2)#1	129.33(18)	C(64)-C(63)-C(57)	120.6(3)
C(61)-N(9)-Mn(2)	126.85(19)	C(65)-C(64)-C(63)	120.3(3)
C(58)-N(9)-Mn(2)	126.58(18)	C(65)-C(64)-H(64A)	119.8
Mn(2)#1-N(9)-Mn(2)	8.69(9)	C(63)-C(64)-H(64A)	119.8
N(8)-C(53)-C(62)#1	126.2(2)	C(66)-C(65)-C(64)	121.4(3)
N(8)-C(53)-C(54)	109.8(2)	C(66)-C(65)-H(65A)	119.3
C(62)#1-C(53)-C(54)	124.0(3)	C(64)-C(65)-H(65A)	119.3
C(55)-C(54)-C(53)	107.0(3)	C(67)-C(66)-C(65)	118.2(3)
C(55)-C(54)-H(54A)	126.5	C(67)-C(66)-C(69)	121.0(3)
C(53)-C(54)-H(54A)	126.5	C(65)-C(66)-C(69)	120.8(3)
C(54)-C(55)-C(56)	107.4(3)	C(66)-C(67)-C(68)	121.2(3)
C(54)-C(55)-H(55A)	126.3	C(66)-C(67)-H(67A)	119.4
C(56)-C(55)-H(55A)	126.3	C(68)-C(67)-H(67A)	119.4
N(8)-C(56)-C(57)	126.2(2)	C(67)-C(68)-C(63)	121.4(3)
N(8)-C(56)-C(55)	109.2(2)	C(67)-C(68)-H(68A)	119.3
C(57)-C(56)-C(55)	124.6(3)	C(63)-C(68)-H(68A)	119.3
C(56)-C(57)-C(58)	123.4(3)	C(66)-C(69)-H(69A)	109.5
C(56)-C(57)-C(63)	118.4(2)	C(66)-C(69)-H(69B)	109.5
C(58)-C(57)-C(63)	118.3(2)	H(69A)-C(69)-H(69B)	109.5
N(9)-C(58)-C(57)	125.5(2)	C(66)-C(69)-H(69C)	109.5
N(9)-C(58)-C(59)	109.8(2)	H(69A)-C(69)-H(69C)	109.5
C(57)-C(58)-C(59)	124.7(3)	H(69B)-C(69)-H(69C)	109.5
C(60)-C(59)-C(58)	107.1(3)	C(75)-C(70)-C(71)	118.1(3)
C(60)-C(59)-H(59A)	126.5	C(75)-C(70)-C(62)	121.4(3)
C(58)-C(59)-H(59A)	126.5	C(71)-C(70)-C(62)	120.5(3)
C(59)-C(60)-C(61)	107.2(3)	C(72)-C(71)-C(70)	120.8(3)
C(59)-C(60)-H(60A)	126.4	C(72)-C(71)-H(71A)	119.6
C(61)-C(60)-H(60A)	126.4	C(70)-C(71)-H(71A)	119.6
N(9)-C(61)-C(62)	126.3(3)	C(71)-C(72)-C(73)	121.2(3)
N(9)-C(61)-C(60)	110.1(2)	C(71)-C(72)-H(72A)	119.4
C(62)-C(61)-C(60)	123.6(2)	C(73)-C(72)-H(72A)	119.4
C(53)#1-C(62)-C(61)	124.6(2)	C(74)-C(73)-C(72)	117.9(3)

C(74)-C(73)-C(76)	120.9(3)	H(76B)-C(76)-H(76C)	109.5
C(72)-C(73)-C(76)	121.2(3)	Cl(4)-C(82)-H(82A)	109.7
C(73)-C(74)-C(75)	121.1(3)	Cl(3)-C(82)-H(82A)	109.7
C(73)-C(74)-H(74A)	119.5	Cl(4)-C(82)-H(82B)	109.7
C(75)-C(74)-H(74A)	119.5	Cl(3)-C(82)-H(82B)	109.7
C(74)-C(75)-C(70)	120.8(3)	H(82A)-C(82)-H(82B)	108.2
C(74)-C(75)-H(75A)	119.6	Cl(3')-C(82')-Cl(4')	109.8(3)
C(70)-C(75)-H(75A)	119.6	Cl(3')-C(82')-H(82C)	109.7
C(73)-C(76)-H(76A)	109.5	Cl(4')-C(82')-H(82C)	109.7
C(73)-C(76)-H(76B)	109.5	Cl(3')-C(82')-H(82D)	109.7
H(76A)-C(76)-H(76B)	109.5	Cl(4')-C(82')-H(82D)	109.7
C(73)-C(76)-H(76C)	109.5	H(82C)-C(82')-H(82D)	108.2
H(76A)-C(76)-H(76C)	109.5	Cl(4)-C(82)-Cl(3)	109.9(3)

**Table 3.10.** Bond Lengths [ $\text{\AA}$ ] for (TPP)Mn(NO)(1-MeIm).

---

Mn(1)-N(5)	1.6411(13)	C(1)-C(20)	1.391(2)
Mn(1)-N(4)	2.0189(12)	C(1)-C(2)	1.445(2)
Mn(1)-N(2)	2.0200(12)	C(2)-C(3)	1.349(2)
Mn(1)-N(1)	2.0248(12)	C(2)-H(2A)	0.9500
Mn(1)-N(3)	2.0280(12)	C(3)-C(4)	1.443(2)
Mn(1)-N(6)	2.0882(13)	C(3)-H(3A)	0.9500
O(1)-N(5)	1.1718(17)	C(4)-C(5)	1.398(2)
N(1)-C(4)	1.3712(18)	C(5)-C(6)	1.397(2)
N(1)-C(1)	1.3738(19)	C(5)-C(21)	1.4977(19)
N(2)-C(9)	1.3721(19)	C(6)-C(7)	1.445(2)
N(2)-C(6)	1.3731(18)	C(7)-C(8)	1.350(2)
N(3)-C(11)	1.3735(19)	C(7)-H(7A)	0.9500
N(3)-C(14)	1.3736(17)	C(8)-C(9)	1.442(2)
N(4)-C(19)	1.3712(19)	C(8)-H(8A)	
N(4)-C(16)	1.3728(18)	C(9)-C(10)	1.401(2)
N(6)-C(47)	1.321(2)	C(10)-C(11)	1.398(2)
N(6)-C(45)	1.3827(19)	C(10)-C(27)	1.499(2)
N(7)-C(47)	1.3478(19)	C(11)-C(12)	1.4458(19)
N(7)-C(46)	1.374(2)	C(12)-C(13)	1.352(2)
N(7)-C(48)	1.456(2)	C(12)-H(12A)	0.9500

C(13)-C(14)	1.443(2)	C(34)-C(35)	1.391(2)
C(13)-H(13A)	0.9500	C(34)-H(34A)	0.9500
C(14)-C(15)	1.397(2)	C(35)-C(36)	1.386(2)
C(15)-C(16)	1.395(2)	C(35)-H(35A)	0.9500
C(15)-C(33)	1.4982(19)	C(36)-C(37)	1.387(2)
C(16)-C(17)	1.446(2)	C(36)-H(36A)	0.9500
C(17)-C(18)	1.348(2)	C(37)-C(38)	1.392(2)
C(17)-H(17A)	0.9500	C(37)-H(37A)	0.9500
C(18)-C(19)	1.4409(19)	C(38)-H(38A)	0.9500
C(18)-H(18A)	0.9500	C(39)-C(40)	1.388(2)
C(19)-C(20)	1.4038(19)	C(39)-C(44)	1.397(2)
C(20)-C(39)	1.498(2)	C(40)-C(41)	1.392(2)
C(21)-C(22)	1.387(2)	C(40)-H(40A)	0.9500
C(21)-C(26)	1.390(2)	C(41)-C(42)	1.386(2)
C(22)-C(23)	1.393(2)	C(41)-H(41A)	0.9500
C(22)-H(22A)	0.9500	C(42)-C(43)	1.381(2)
C(23)-C(24)	1.378(3)	C(42)-H(42A)	0.9500
C(23)-H(23A)	0.9500	C(43)-C(44)	1.390(2)
C(24)-C(25)	1.372(3)	C(43)-H(43A)	0.9500
C(24)-H(24A)	0.9500	C(44)-H(44A)	0.9500
C(25)-C(26)	1.392(2)	C(45)-C(46)	1.346(2)
C(25)-H(25A)	0.9500	C(45)-H(45A)	0.9500
C(26)-H(26A)	0.9500	C(46)-H(46A)	0.9500
C(27)-C(28)	1.392(2)	C(47)-H(47A)	0.9500
C(27)-C(32)	1.397(2)	C(48)-H(48A)	0.9800
C(28)-C(29)	1.395(2)	C(48)-H(48B)	0.9800
C(28)-H(28A)	0.9500	C(48)-H(48C)	0.9800
C(29)-C(30)	1.383(3)	C(49)-C(50)	1.377(3)
C(29)-H(29A)	0.9500	C(49)-C(54)	1.393(3)
C(30)-C(31)	1.379(3)	C(49)-H(49A)	0.9500
C(30)-H(30A)	0.9500	C(50)-C(51)	1.381(3)
C(31)-C(32)	1.393(2)	C(50)-H(50A)	0.9500
C(31)-H(31A)	0.9500	C(51)-C(52)	1.347(4)
C(32)-H(32A)	0.9500	C(51)-H(51A)	0.9500
C(33)-C(34)	1.390(2)	C(52)-C(53)	1.367(4)
C(33)-C(38)	1.393(2)	C(52)-H(52A)	0.9500

C(53)-C(54)	1.390(3)	C(60)-H(60A)	0.9500
C(53)-H(53A)	0.9500	C(61)-C(62)	1.435(4)
C(54)-C(55)	1.500(4)	C(62)-H(62A)	0.9800
C(55)-H(55A)	0.9800	C(62)-H(62B)	0.9800
C(55)-H(55B)	0.9800	C(62)-H(62C)	0.9800
C(55)-H(55C)	0.9800	C(63)-C(65)#1	1.388(4)
C(56)-C(61)	1.373(4)	C(63)-C(64)	1.392(4)
C(56)-C(57)	1.377(5)	C(63)-H(63A)	0.9500
C(56)-H(56A)	0.9500	C(64)-C(65)	1.384(4)
C(57)-C(58)	1.400(4)	C(64)-C(66)	1.538(7)
C(57)-H(57A)	0.9500	C(65)-C(63)#1	1.388(4)
C(58)-C(59)	1.349(4)	C(65)-H(65A)	0.9500
C(58)-H(58A)	0.9500	C(66)-H(66A)	0.9800
C(59)-C(60)	1.359(4)	C(66)-H(66B)	0.9800
C(59)-H(59A)	0.9500	C(66)-H(66C)	0.9800
C(60)-C(61)	1.413(4)		

**Table 3.11.** Bond Angles [°] for (TPP)Mn(NO)(1-MeIm).

N(5)-Mn(1)-N(4)	93.56(5)	C(1)-N(1)-Mn(1)	126.90(9)
N(5)-Mn(1)-N(2)	93.47(6)	C(9)-N(2)-C(6)	106.38(12)
N(4)-Mn(1)-N(2)	172.97(5)	C(9)-N(2)-Mn(1)	127.25(9)
N(5)-Mn(1)-N(1)	91.15(5)	C(6)-N(2)-Mn(1)	126.36(10)
N(4)-Mn(1)-N(1)	89.47(5)	C(11)-N(3)-C(14)	106.16(12)
N(2)-Mn(1)-N(1)	90.37(5)	C(11)-N(3)-Mn(1)	126.63(9)
N(5)-Mn(1)-N(3)	92.65(5)	C(14)-N(3)-Mn(1)	126.20(10)
N(4)-Mn(1)-N(3)	89.99(5)	C(19)-N(4)-C(16)	106.02(12)
N(2)-Mn(1)-N(3)	89.71(5)	C(19)-N(4)-Mn(1)	127.15(9)
N(1)-Mn(1)-N(3)	176.18(5)	C(16)-N(4)-Mn(1)	126.51(10)
N(5)-Mn(1)-N(6)	178.30(5)	O(1)-N(5)-Mn(1)	178.42(12)
N(4)-Mn(1)-N(6)	87.96(5)	C(47)-N(6)-C(45)	105.11(13)
N(2)-Mn(1)-N(6)	85.01(5)	C(47)-N(6)-Mn(1)	129.25(10)
N(1)-Mn(1)-N(6)	88.10(5)	C(45)-N(6)-Mn(1)	125.52(11)
N(3)-Mn(1)-N(6)	88.10(5)	C(47)-N(7)-C(46)	106.90(13)
C(4)-N(1)-C(1)	106.19(12)	C(47)-N(7)-C(48)	127.13(13)
C(4)-N(1)-Mn(1)	126.30(10)	C(46)-N(7)-C(48)	125.92(13)

N(1)-C(1)-C(20)	125.75(13)	C(12)-C(13)-C(14)	107.02(13)
N(1)-C(1)-C(2)	109.90(12)	C(12)-C(13)-H(13A)	126.5
C(20)-C(1)-C(2)	124.34(14)	C(14)-C(13)-H(13A)	126.5
C(3)-C(2)-C(1)	106.85(13)	N(3)-C(14)-C(15)	125.75(13)
C(3)-C(2)-H(2A)	126.6	N(3)-C(14)-C(13)	109.97(13)
C(1)-C(2)-H(2A)	126.6	C(15)-C(14)-C(13)	124.28(13)
C(2)-C(3)-C(4)	107.22(13)	C(16)-C(15)-C(14)	124.34(13)
C(2)-C(3)-H(3A)	126.4	C(16)-C(15)-C(33)	117.29(13)
C(4)-C(3)-H(3A)	126.4	C(14)-C(15)-C(33)	118.32(13)
N(1)-C(4)-C(5)	125.57(13)	N(4)-C(16)-C(15)	126.23(13)
N(1)-C(4)-C(3)	109.84(13)	N(4)-C(16)-C(17)	109.93(12)
C(5)-C(4)-C(3)	124.54(13)	C(15)-C(16)-C(17)	123.79(13)
C(6)-C(5)-C(4)	124.66(13)	C(18)-C(17)-C(16)	106.81(13)
C(6)-C(5)-C(21)	117.71(13)	C(18)-C(17)-H(17A)	126.6
C(4)-C(5)-C(21)	117.59(13)	C(16)-C(17)-H(17A)	126.6
N(2)-C(6)-C(5)	125.95(13)	C(17)-C(18)-C(19)	107.18(13)
N(2)-C(6)-C(7)	109.61(12)	C(17)-C(18)-H(18A)	126.4
C(5)-C(6)-C(7)	124.33(13)	C(19)-C(18)-H(18A)	126.4
C(8)-C(7)-C(6)	107.10(13)	N(4)-C(19)-C(20)	125.90(13)
C(8)-C(7)-H(7A)	126.4	N(4)-C(19)-C(18)	110.02(12)
C(6)-C(7)-H(7A)	126.4	C(20)-C(19)-C(18)	123.94(13)
C(7)-C(8)-C(9)	107.04(13)	C(1)-C(20)-C(19)	124.04(13)
C(7)-C(8)-H(8A)	126.5	C(1)-C(20)-C(39)	118.84(12)
C(9)-C(8)-H(8A)	126.5	C(19)-C(20)-C(39)	117.09(13)
N(2)-C(9)-C(10)	125.55(13)	C(22)-C(21)-C(26)	118.57(15)
N(2)-C(9)-C(8)	109.83(12)	C(22)-C(21)-C(5)	120.07(15)
C(10)-C(9)-C(8)	124.61(14)	C(26)-C(21)-C(5)	121.36(15)
C(11)-C(10)-C(9)	124.54(14)	C(21)-C(22)-C(23)	120.57(19)
C(11)-C(10)-C(27)	117.63(12)	C(21)-C(22)-H(22A)	119.7
C(9)-C(10)-C(27)	117.80(13)	C(23)-C(22)-H(22A)	119.7
N(3)-C(11)-C(10)	125.53(13)	C(24)-C(23)-C(22)	120.3(2)
N(3)-C(11)-C(12)	109.86(12)	C(24)-C(23)-H(23A)	119.9
C(10)-C(11)-C(12)	124.60(14)	C(22)-C(23)-H(23A)	119.9
C(13)-C(12)-C(11)	106.98(13)	C(25)-C(24)-C(23)	119.59(17)
C(13)-C(12)-H(12A)	126.5	C(25)-C(24)-H(24A)	120.2
C(11)-C(12)-H(12A)	126.5	C(23)-C(24)-H(24A)	120.2

C(24)-C(25)-C(26)	120.62(19)	C(36)-C(37)-C(38)	120.00(14)
C(24)-C(25)-H(25A)	119.7	C(36)-C(37)-H(37A)	120.0
C(26)-C(25)-H(25A)	119.7	C(38)-C(37)-H(37A)	120.0
C(21)-C(26)-C(25)	120.38(19)	C(37)-C(38)-C(33)	120.43(14)
C(21)-C(26)-H(26A)	119.8	C(37)-C(38)-H(38A)	119.8
C(25)-C(26)-H(26A)	119.8	C(33)-C(38)-H(38A)	119.8
C(28)-C(27)-C(32)	118.92(15)	C(40)-C(39)-C(44)	118.96(14)
C(28)-C(27)-C(10)	121.68(15)	C(40)-C(39)-C(20)	121.00(13)
C(32)-C(27)-C(10)	119.40(14)	C(44)-C(39)-C(20)	120.01(14)
C(27)-C(28)-C(29)	120.32(17)	C(39)-C(40)-C(41)	120.70(15)
C(27)-C(28)-H(28A)	119.8	C(39)-C(40)-H(40A)	119.6
C(29)-C(28)-H(28A)	119.8	C(41)-C(40)-H(40A)	119.6
C(30)-C(29)-C(28)	120.12(18)	C(42)-C(41)-C(40)	119.94(15)
C(30)-C(29)-H(29A)	119.9	C(42)-C(41)-H(41A)	120.0
C(28)-C(29)-H(29A)	119.9	C(40)-C(41)-H(41A)	120.0
C(31)-C(30)-C(29)	120.10(16)	C(43)-C(42)-C(41)	119.78(15)
C(31)-C(30)-H(30A)	120.0	C(43)-C(42)-H(42A)	120.1
C(29)-C(30)-H(30A)	120.0	C(41)-C(42)-H(42A)	120.1
C(30)-C(31)-C(32)	120.14(17)	C(42)-C(43)-C(44)	120.51(15)
C(30)-C(31)-H(31A)	119.9	C(42)-C(43)-H(43A)	119.7
C(32)-C(31)-H(31A)	119.9	C(44)-C(43)-H(43A)	119.7
C(31)-C(32)-C(27)	120.39(17)	C(43)-C(44)-C(39)	120.11(15)
C(31)-C(32)-H(32A)	119.8	C(43)-C(44)-H(44A)	119.9
C(27)-C(32)-H(32A)	119.8	C(39)-C(44)-H(44A)	119.9
C(34)-C(33)-C(38)	119.09(13)	C(46)-C(45)-N(6)	109.95(14)
C(34)-C(33)-C(15)	121.12(13)	C(46)-C(45)-H(45A)	125.0
C(38)-C(33)-C(15)	119.79(13)	N(6)-C(45)-H(45A)	125.0
C(33)-C(34)-C(35)	120.50(14)	C(45)-C(46)-N(7)	106.46(14)
C(33)-C(34)-H(34A)	119.7	C(45)-C(46)-H(46A)	126.8
C(35)-C(34)-H(34A)	119.8	N(7)-C(46)-H(46A)	126.8
C(36)-C(35)-C(34)	120.11(15)	N(6)-C(47)-N(7)	111.58(13)
C(36)-C(35)-H(35A)	119.9	N(6)-C(47)-H(47A)	124.2
C(34)-C(35)-H(35A)	119.9	N(7)-C(47)-H(47A)	124.2
C(35)-C(36)-C(37)	119.86(14)	N(7)-C(48)-H(48A)	109.5
C(35)-C(36)-H(36A)	120.1	N(7)-C(48)-H(48B)	109.5
C(37)-C(36)-H(36A)	120.1	H(48A)-C(48)-H(48B)	109.5

N(7)-C(48)-H(48C)	109.5	C(52)-C(53)-C(54)	121.3(3)
H(48A)-C(48)-H(48C)	109.5	C(52)-C(53)-H(53A)	119.3
H(48B)-C(48)-H(48C)	109.5	C(54)-C(53)-H(53A)	119.3
C(50)-C(49)-C(54)	120.7(2)	C(49)-C(54)-C(53)	117.2(2)
C(50)-C(49)-H(49A)	119.6	C(49)-C(54)-C(55)	121.3(2)
C(54)-C(49)-H(49A)	119.6	C(53)-C(54)-C(55)	121.5(2)
C(49)-C(50)-C(51)	120.2(2)	C(54)-C(55)-H(55A)	109.5
C(49)-C(50)-H(50A)	119.9	C(54)-C(55)-H(55B)	109.5
C(51)-C(50)-H(50A)	119.9	H(55A)-C(55)-H(55B)	109.5
C(52)-C(51)-C(50)	119.6(3)	C(54)-C(55)-H(55C)	109.5
C(52)-C(51)-H(51A)	120.2	H(55A)-C(55)-H(55C)	109.5
C(50)-C(51)-H(51A)	120.2	H(55B)-C(55)-H(55C)	109.5
C(51)-C(52)-C(53)	121.0(2)	C(61)-C(56)-C(57)	119.1(3)
C(51)-C(52)-H(52A)	119.5	C(61)-C(56)-H(56A)	120.4
C(53)-C(52)-H(52A)	119.5	C(57)-C(56)-H(56A)	120.4
C(56)-C(57)-C(58)	122.0(3)	C(61)-C(62)-H(62C)	109.5
C(56)-C(57)-H(57A)	119.0	H(62A)-C(62)-H(62C)	109.5
C(58)-C(57)-H(57A)	119.0	H(62B)-C(62)-H(62C)	109.5
C(59)-C(58)-C(57)	117.5(3)	C(65)#1-C(63)-C(64)	121.5(3)
C(59)-C(58)-H(58A)	121.2	C(65)#1-C(63)-H(63A)	119.3
C(57)-C(58)-H(58A)	121.2	C(64)-C(63)-H(63A)	119.3
C(58)-C(59)-C(60)	122.5(3)	C(65)-C(64)-C(63)	117.0(3)
C(58)-C(59)-H(59A)	118.7	C(65)-C(64)-C(66)	121.5(3)
C(60)-C(59)-H(59A)	118.7	C(63)-C(64)-C(66)	121.4(3)
C(59)-C(60)-C(61)	119.8(2)	C(64)-C(65)-C(63)#1	121.5(3)
C(59)-C(60)-H(60A)	120.1	C(64)-C(65)-H(65A)	119.3
C(61)-C(60)-H(60A)	120.1	C(63)#1-C(65)-H(65A)	119.3
C(56)-C(61)-C(60)	119.0(3)	C(64)-C(66)-H(66A)	109.5
C(56)-C(61)-C(62)	118.9(3)	C(64)-C(66)-H(66B)	109.5
C(60)-C(61)-C(62)	122.0(3)	H(66A)-C(66)-H(66B)	109.5
C(61)-C(62)-H(62A)	109.5	C(64)-C(66)-H(66C)	109.5
C(61)-C(62)-H(62B)	109.5	H(66A)-C(66)-H(66C)	109.5
H(62A)-C(62)-H(62B)	109.5	H(66B)-C(66)-H(66C)	109.5

**Table 3.12.** Bond Lengths [Å] for (T(*p*-OCH<sub>3</sub>)PP)Mn(NO)(1-MeIm).

Mn(1)-N(5)	1.645(3)	C(5)-C(21)	1.501(5)
Mn(1)-N(1)	2.015(3)	C(6)-C(7)	1.420(5)
Mn(1)-N(3)	2.028(3)	C(7)-C(8)	1.341(5)
Mn(1)-N(2)	2.032(3)	C(8)-C(9)	1.434(5)
Mn(1)-N(4)	2.034(3)	C(9)-C(10)	1.396(5)
Mn(1)-N(6)	2.097(3)	C(10)-C(11)	1.413(5)
O(1)-N(5)	1.176(4)	C(10)-C(28)	1.514(5)
O(2)-C(24)	1.388(4)	C(11)-C(12)	1.439(5)
O(2)-C(27)	1.438(5)	C(12)-C(13)	1.360(5)
O(3)-C(31)	1.378(4)	C(13)-C(14)	1.420(5)
O(3)-C(34)	1.424(5)	C(14)-C(15)	1.402(5)
O(4)-C(38)	1.372(4)	C(15)-C(16)	1.400(5)
O(4)-C(41)	1.434(5)	C(15)-C(35)	1.501(5)
O(5)-C(45)	1.380(4)	C(16)-C(17)	1.445(5)
O(5)-C(48)	1.407(5)	C(17)-C(18)	1.352(5)
N(1)-C(1)	1.365(4)	C(18)-C(19)	1.455(4)
N(1)-C(4)	1.404(4)	C(19)-C(20)	1.380(5)
N(2)-C(9)	1.375(4)	C(20)-C(42)	1.500(5)
N(2)-C(6)	1.382(4)	C(21)-C(26)	1.377(5)
N(3)-C(11)	1.365(4)	C(21)-C(22)	1.385(5)
N(3)-C(14)	1.398(4)	C(22)-C(23)	1.391(5)
N(4)-C(19)	1.370(4)	C(23)-C(24)	1.385(5)
N(4)-C(16)	1.377(4)	C(24)-C(25)	1.378(5)
N(6)-C(51)	1.307(5)	C(25)-C(26)	1.397(5)
N(6)-C(49)	1.382(5)	C(28)-C(29)	1.378(5)
N(7)-C(50)	1.331(5)	C(28)-C(33)	1.393(5)
N(7)-C(51)	1.368(5)	C(29)-C(30)	1.387(5)
N(7)-C(52)	1.446(6)	C(30)-C(31)	1.366(5)
C(1)-C(20)	1.427(5)	C(31)-C(32)	1.372(5)
C(1)-C(2)	1.429(5)	C(32)-C(33)	1.377(5)
C(2)-C(3)	1.360(5)	C(35)-C(36)	1.387(5)
C(3)-C(4)	1.434(5)	C(35)-C(40)	1.389(5)
C(4)-C(5)	1.410(4)	C(36)-C(37)	1.377(5)
C(5)-C(6)	1.398(5)	C(37)-C(38)	1.387(5)

C(38)-C(39)	1.383(5)	C(49)-C(50)	1.352(6)
C(39)-C(40)	1.399(5)	C(53)-Cl(1)	1.717(4)
C(42)-C(47)	1.377(5)	C(53)-Cl(2)	1.720(4)
C(42)-C(43)	1.389(5)	C(53')-Cl(1')	1.719(4)
C(43)-C(44)	1.378(5)	C(53')-Cl(2')	1.720(4)
C(44)-C(45)	1.387(5)	C(53'')-Cl(1'')	1.715(4)
C(45)-C(46)	1.357(5)	C(53'')-Cl(2'')	1.720(4)
C(46)-C(47)	1.393(5)		

**Table 3.13** Bond Angles [°] for (T(*p*-OCH<sub>3</sub>)PP)Mn(NO)(1-MeIm).

N(5)-Mn(1)-N(1)	93.88(14)	C(11)-N(3)-C(14)	105.2(3)
N(5)-Mn(1)-N(3)	92.84(14)	C(11)-N(3)-Mn(1)	127.7(2)
N(1)-Mn(1)-N(3)	173.27(12)	C(14)-N(3)-Mn(1)	126.4(2)
N(5)-Mn(1)-N(2)	93.21(13)	C(19)-N(4)-C(16)	107.0(3)
N(1)-Mn(1)-N(2)	90.84(11)	C(19)-N(4)-Mn(1)	126.7(2)
N(3)-Mn(1)-N(2)	89.24(11)	C(16)-N(4)-Mn(1)	125.9(2)
N(5)-Mn(1)-N(4)	91.66(13)	O(1)-N(5)-Mn(1)	178.3(3)
N(1)-Mn(1)-N(4)	88.81(11)	C(51)-N(6)-C(49)	105.2(3)
N(3)-Mn(1)-N(4)	90.54(11)	C(51)-N(6)-Mn(1)	128.7(3)
N(2)-Mn(1)-N(4)	175.13(12)	C(49)-N(6)-Mn(1)	126.1(3)
N(5)-Mn(1)-N(6)	179.31(13)	C(50)-N(7)-C(51)	108.1(3)
N(1)-Mn(1)-N(6)	86.11(11)	C(50)-N(7)-C(52)	125.8(4)
N(3)-Mn(1)-N(6)	87.17(11)	C(51)-N(7)-C(52)	126.1(4)
N(2)-Mn(1)-N(6)	87.48(11)	N(1)-C(1)-C(20)	124.6(3)
N(4)-Mn(1)-N(6)	87.65(11)	N(1)-C(1)-C(2)	111.7(3)
C(24)-O(2)-C(27)	116.2(3)	C(20)-C(1)-C(2)	123.7(3)
C(31)-O(3)-C(34)	117.2(3)	C(3)-C(2)-C(1)	106.5(3)
C(38)-O(4)-C(41)	116.3(3)	C(2)-C(3)-C(4)	107.4(3)
C(45)-O(5)-C(48)	117.7(3)	N(1)-C(4)-C(5)	125.6(3)
C(1)-N(1)-C(4)	104.8(3)	N(1)-C(4)-C(3)	109.6(3)
C(1)-N(1)-Mn(1)	128.9(2)	C(5)-C(4)-C(3)	124.8(3)
C(4)-N(1)-Mn(1)	126.0(2)	C(6)-C(5)-C(4)	124.9(3)
C(9)-N(2)-C(6)	106.4(3)	C(6)-C(5)-C(21)	117.5(3)
C(9)-N(2)-Mn(1)	127.0(2)	C(4)-C(5)-C(21)	117.6(3)
C(6)-N(2)-Mn(1)	126.6(2)	(2)-C(6)-C(5)	125.7(3)

N(2)-C(6)-C(7)	109.1(3)	C(24)-C(23)-C(22)	119.5(4)
C(5)-C(6)-C(7)	125.1(3)	C(25)-C(24)-C(23)	120.4(3)
C(8)-C(7)-C(6)	108.1(3)	C(25)-C(24)-O(2)	123.8(3)
C(7)-C(8)-C(9)	107.2(3)	C(23)-C(24)-O(2)	115.7(3)
N(2)-C(9)-C(10)	126.4(3)	C(24)-C(25)-C(26)	119.0(3)
N(2)-C(9)-C(8)	109.2(3)	C(21)-C(26)-C(25)	121.7(3)
C(10)-C(9)-C(8)	124.4(3)	C(29)-C(28)-C(33)	117.2(3)
C(9)-C(10)-C(11)	123.7(3)	C(29)-C(28)-C(10)	122.1(3)
C(9)-C(10)-C(28)	117.9(3)	C(33)-C(28)-C(10)	120.7(3)
C(11)-C(10)-C(28)	118.4(3)	C(28)-C(29)-C(30)	121.3(4)
N(3)-C(11)-C(10)	125.7(3)	C(31)-C(30)-C(29)	120.4(4)
N(3)-C(11)-C(12)	111.0(3)	C(30)-C(31)-C(32)	119.4(3)
C(10)-C(11)-C(12)	123.3(3)	C(30)-C(31)-O(3)	124.6(4)
C(13)-C(12)-C(11)	106.2(3)	C(32)-C(31)-O(3)	116.0(3)
C(12)-C(13)-C(14)	107.8(3)	C(31)-C(32)-C(33)	120.3(4)
N(3)-C(14)-C(15)	124.7(3)	C(32)-C(33)-C(28)	121.4(4)
N(3)-C(14)-C(13)	109.8(3)	C(36)-C(35)-C(40)	117.2(3)
C(15)-C(14)-C(13)	125.4(3)	C(36)-C(35)-C(15)	120.1(3)
C(16)-C(15)-C(14)	125.5(3)	C(40)-C(35)-C(15)	122.7(3)
C(16)-C(15)-C(35)	117.2(3)	C(37)-C(36)-C(35)	122.3(4)
C(14)-C(15)-C(35)	117.3(3)	C(36)-C(37)-C(38)	119.8(4)
N(4)-C(16)-C(15)	126.2(3)	O(4)-C(38)-C(39)	116.4(4)
N(4)-C(16)-C(17)	109.2(3)	O(4)-C(38)-C(37)	124.0(4)
C(15)-C(16)-C(17)	124.5(3)	C(39)-C(38)-C(37)	119.6(3)
C(18)-C(17)-C(16)	107.5(3)	C(38)-C(39)-C(40)	119.6(4)
C(17)-C(18)-C(19)	106.9(3)	C(35)-C(40)-C(39)	121.5(4)
N(4)-C(19)-C(20)	127.3(3)	C(47)-C(42)-C(43)	116.9(3)
N(4)-C(19)-C(18)	109.3(3)	C(47)-C(42)-C(20)	121.6(3)
C(20)-C(19)-C(18)	123.4(3)	C(43)-C(42)-C(20)	121.5(3)
C(19)-C(20)-C(1)	123.3(3)	C(44)-C(43)-C(42)	121.7(3)
C(19)-C(20)-C(42)	119.6(3)	C(43)-C(44)-C(45)	120.0(4)
C(1)-C(20)-C(42)	117.0(3)	C(46)-C(45)-O(5)	124.8(3)
C(26)-C(21)-C(22)	118.3(3)	C(46)-C(45)-C(44)	119.1(3)
C(26)-C(21)-C(5)	120.3(3)	O(5)-C(45)-C(44)	116.0(3)
C(22)-C(21)-C(5)	121.4(3)	C(45)-C(46)-C(47)	120.5(4)
C(21)-C(22)-C(23)	121.1(3)	C(42)-C(47)-C(46)	121.7(4)

C(50)-C(49)-N(6)	109.9(4)	Cl(1)-C(53)-Cl(2)	114.5(3)
N(7)-C(50)-C(49)	106.3(4)	Cl(1')-C(53')-Cl(2')	114.3(3)
N(6)-C(51)-N(7)	110.5(4)	Cl(1'')-C(53'')-Cl(2'')	114.5(3)